Probing Ytterbium Quantum Gases in an Optical Lattice using the Clock Transition

Dissertation

zur Erlangung des Doktorgrades
an der Fakultät für Mathematik, Informatik und Naturwissenschaften,
Fachbereich Physik
der Universität Hamburg

vorgelegt von
Thomas Georg Ponath
aus Jena

Hamburg
2018

Gutachter der Dissertation:	Prof. Dr. Klaus Sengstock Prof. Dr. Henning Moritz
Zusammensetzung der Prüfungskommission:	Prof. Dr. Klaus Sengstock Prof. Dr. Henning Moritz Prof. Dr. Günter Huber Prof. Dr. Ludwig Mathey Prof. Dr. Roman Schnabel
Vorsitzender der Prüfungskommission:	Prof. Dr. Roman Schnabel
Datum der Disputation:	12. Juni 2018
Vorsitzender des Fach-Promotionsausschusses Physik:	Prof. Dr. Wolfgang Hansen
Leiter des Fachbereichs Physik:	Prof. Dr. Michael Potthoff
Dekan der Fakultät Mathematik, Informatik und Naturwissenschaften:	Prof. Dr. Heinrich Graener

Abstract

In the “Ytterbium quantum gas” experiment, we investigate strongly correlated quantum many-body physics with a system of ultracold Ytterbium in an optical lattice by performing spectroscopy on an ultra-narrow “clock” transition using a stable, narrow-linewidth laser.

Ultracold quantum gases of alkaline-earth-like (AEL) elements are highly suitable as “quantum simulator” systems for the investigation of strongly-correlated many-body physics. Fermionic AELs, such as ^{173}Yb, exhibit many favourable features for experiments: a narrow clock transition enabling precision spectroscopy measurements, a low-lying, long-lived metastable state, a decoupled nuclear spin- and electronic state and an SU(N) symmetry. Ultracold quantum gases of AEL atoms in an optical lattice enable experimental realizations of complex systems, such as the Kondo lattice model, or the study of correlations emerging in strongly dissipative systems.

I show an experimental apparatus of an all-optical 2D/3D MOT setup with three-beam optical dipole trap. We prepare clean, ultracold Ytterbium quantum gases with control over the spin population. We can load several 10^4 atoms into the lowest band of a three-dimensional, deep optical lattice, operating at the magic-wavelength of 578 nm. An imaging system with a repumping laser enables the separate detection of ground- and excited state atoms.

Coherent control over the metastable electronic state and high spectroscopic resolution require a highly stable, narrow-linewidth laser system, which is at the focus of this thesis. I present a detailed characterisation of our revised 578 nm “clock” laser system stabilised by Pound-Drever-Hall (PDH) lock to a high-finesse cavity. Key features are the all-ULE glass cavity enabling operation with low sensitivities to temperature- and beam power fluctuations, a waveguide-based, fibre-coupled EOM providing optimal modulation depths for the PDH lock, an improved beam power stabilisation in the lock setup and an improved phase-stable fibre link to the experiment. In a stability evaluation with a beam independently locked to a second cavity, the clock laser shows a short-time linewidth of 1 Hz over 2 s. The combined system shows 1-hour long windows of approximately linear drift with remaining frequency fluctuations up to 50 Hz. Monitoring the atomic resonance frequency, we obtained a long-term linear drift of -318 ± 1 mHz/s of the cavity. This laser system is a crucial tool for the preparation, manipulation and probing of strongly-correlated many-body systems of ultracold Ytterbium.

In coherent clock spectroscopy measurements on single spin-component ^{173}Yb, we achieved a high-resolution of 50 ± 2 Hz FWHM (sinc² curve fit) and over 80% excitation fraction to the metastable $^3P_0$ state. We showed transitions to higher bands in the optical lattice. Performing spectroscopy on two spin-component mixtures, we resolved a feature of spin-exchange interactions between inter-orbital two-particle states.

The presented apparatus and the developed techniques for preparation and coherent control of Ytterbium provide an ideal starting point for the study of novel quantum systems.

Zusammenfassung

Im “Ytterbium Quantengas”-Experiment untersuchen wir stark korrelierte Quantenvielteilchenphysik mit einem System aus ultrakaltem Ytterbium in einem optischen Gitter durch Spektroskopie an einem extrem schmalen “Uhrenübergang” mit einem stabilen, schmalbandigen Laser.

Ultrakalte Quantengase aus Erdalkali-ähnlichen (AEL) Atomen eignen sich hervorragend als "Quantensimulator"-Systeme zur Untersuchung stark korrelierter Vielteilchenphysik. Fermionische AELs, wie z.B. ^{173}Yb, weisen viele günstige Eigenschaften für Experimente auf: einen schmalen Uhrenübergang, der präzise spektroskopische Messungen ermöglicht, einen tief liegenden, langlebigen metastabilen Zustand, eine Entkopplung von Kernspin und elektronischem Zustand und eine SU(N)-Symmetrie. Ultrakalte Quantengase von AEL-Atomen in einem optischen Gitter ermöglichen die experimentelle Realisierung komplexer Systeme wie das Kondo-Gitter-Modell oder die Untersuchung von Korrelationen in stark dissipativen Systemen.

Ich stelle einen Aufbau einer volloptischen 2D/3D MOT mit optischer Dipolfalle vor. Wir erzeugen saubere, ultrakalte Ytterbium-Quantengase mit Kontrolle über die Spin-Population. Wir können einige 10^4 Atome in das unterste Band eines tiefen dreidimensionalen optischen Gitters laden, das bei der magischen Wellenlänge von 578 nm arbeitet. Ein Abbildungssystem mit einem Repumping-Laser ermöglicht die getrennte Detektion von grundzustands- und angeregten Atomen.

Kohärente Kontrolle über den metastabilen elektronischen Zustand und eine hohe spektroskopische Auflösung erfordern ein hochstabiles, schmalbandiges Lasersystem, das im Zentrum dieser Arbeit steht. Ich präsentiere eine detaillierte Charakterisierung unseres überarbeiteten 578 nm “Uhren”-Lasersystems, welches durch einen Pound-Drever-Hall (PDH) Lock auf einen Resonator mit hoher Finesse stabilisiert wird. Wesentliche Neuerungen sind der vollständig aus ULE Glas bestehende Resonator, der einen Betrieb mit geringer Empfindlichkeit gegenüber Temperatur- und Strahlleistungsschwankungen ermöglicht, ein wellenleiterbasierter, fasergekoppelter EOM für optimale Modulationstiefen des PDH-Lock, eine verbesserte Strahlleistungs-Stabilisierung im Lock-Aufbau und eine verbesserte phasenstabile Faserverbindung zum Experiment. In einer Stabilitätsanalyse mit einem unabhängig auf einen zweiten Resonator stabilisierten Strahl zeigt der Uhrenlaser eine kurzzeitige Linienbreite von 1 Hz über 2 s. Das kombinierte System zeigt 1 Stunde lange Zeitfenster mit annähernd linearem Drift und verbleibende Frequenzschwankungen von bis zu 50 Hz. Die Messungen der atomaren Resonanzfrequenz ergab einen langfristigen linearen Drift des Resonators von 318 ± 1 mHz/s. Dieses Lasersystem ist ein wichtiges Werkzeug für die Präparation, Manipulation und Untersuchung von stark korrelierten Vielteilchensysteme aus ultrakaltem Ytterbium.

In kohärenten Uhrenspektroskopie an Spin-polarisiertem ^{173}Yb erreichten wir eine hohe Auflösung von 50 ± 2 Hz FWHM (sinc^2-Funktions-Fit) und über 80% Anregung in dem metastabilen $^3P_0$-Zustand. Wir präsentierten Übergänge in höhere Bändern des optischen Gitters. In Spektroskopie-Messungen an Zwei-Spin-Komponenten-Mischungen konnten wir ein Merkmal von Spin-Austausch-Wechselwirkungen zwischen interorbitalen Zwei-Teilchen-Zuständen auflösen.

Der vorgestellte Aufbau und die entwickelten Techniken zur Präparation und kohärenten Kontrolle von Ytterbium bieten einen idealen Ausgangspunkt für die Erforschung neuer Quantensysteme.

Publikationen

Im Rahmen der vorliegenden Arbeit ist die folgende wissenschaftliche Veröffentlichung entstanden.

Publications

The following research article has been published in the course of this thesis.

[P1] K. Sponselee, L. Freystatzky, B. Abeln, M. Diem, B. Hundt, A. Kochanke, T. Ponath, B. Santra, L. Mathey, K. Sengstock, C. Becker, 'Dynamics of Ultracold Quantum Gases in the Dissipative Fermi-Hubbard Model' *New Journal of Physics,* In Review (2018) https://arxiv.org/abs/1805.11853

This work was made possible by the Marie Curie Initial Training Network "QTea", financed by the FP7 of the European Commission, contract-No MCITN-317485.

Contents

List of Figures

Chapter 1 Introduction

In the Ytterbium quantum gas experiment, we investigate quantum many-body physics with a system of ultracold Ytterbium atoms in an optical lattice by performing spectroscopy on an ultra-narrow atomic transition using a stable, narrow-linewidth laser.

Quantum many-body physics describes systems of many interacting constituents in complex structures, such as atom structures or solid-state systems. The system's individual parts, such as electrons, neutrons, protons, or atoms themselves, and the fundamental laws governing their interactions are well understood when looked at individually. Interactions between large numbers of constituents give rise to correlations in the system which influence its static and dynamic properties. Examples of properties resulting from strong interactions are high-temperature superconductors and heavy Fermion materials. "More is different" [1] expresses this effect of an emergence of new properties in larger, more complex systems, which individual constituents obey well-known fundamental laws.

The full system's complex structure and the high number of interacting particles, resulting in an exponential growth of information, can hinder a theoretical or computational analysis. Researchers can circumvent these problems by experimentally implementing simplified model systems with real quantum behaviour in highly controlled environments. Such "quantum simulators" [2] bridge the gap between a simplified theoretical treatment and the investigation of real-world systems which offer only limited access for observation and manipulation. Ultracold quantum gases in an optical lattice are excellent quantum simulators for many-body systems [3–5]:

Quantum gases can be cooled to nano-Kelvin temperatures where the atoms occupy lowest quantum mechanical states and atomic interactions in the low-density gas dominate the properties of the system. Optical lattices strongly confine the atoms in regular, deep potentials, thereby reducing the kinetic tunnelling energy and enhancing the influence of onsite atomic interactions. Quantum gases in optical lattices can be observed and tuned with high control, repeatability, purity, and isolation from external influences.

Investigating the behaviour of a quantum gas model system can help to understand the original, complex many-body system. Furthermore, new tools and novel experiments enable access and observations not possible in original solid-state systems, such as momentum resolved spectroscopy or single-site resolution and manipulation. Advancing even further, one can design complex synthetic materials with properties only predicted by theoretical models and not known in nature.

Several groups of elements are established in quantum gas experiments: Alkali atoms, such as bosonic ^{87}Rb and ^{23}Na or fermionic ^{40}K, were the first atoms are cooled to quantum degeneracy [6–8]. Their electron structure is favourable for laser cooling and Feshbach resonances allow a tuning of the atom interaction strength. Experiments with Alkali atoms achieved realizations of the Bose-Hubbard and of the Fermi-Hubbard model, as prime examples. Technical advances enabled quantum gas experiments with atoms which exhibit more complex atomic properties. Experiments with Chromium, Dysprosium and Erbium, for example, make use of the atom's long-range, anisotropic dipole moment [9–11]. Experiments with Rydberg atoms investigate long-range interactions [12,13]. A third group of elements in quantum gas experiments are alkali-earth atoms (such as Calcium [14] and Strontium [15]) and the alkali-earth-like element Ytterbium (Yb) [16,17].

Alkali-earth atoms (AEA) and Alkali-earth-like (AEL) elements have two valence electrons in their electronic structure. This results in energetically low-lying, metastable states which are highly decoupled from perturbations. The transition between ground state and lowest metastable state possesses an ultra-narrow linewidth on the millihertz scale. Optical lattice clocks used in frequency metrology probe this 'clock' transition of Alkali-earth-like atoms as frequency reference, reaching unprecedented stability levels of 10^{-18} [18–21].

Fermionic AEA and AEL atoms have zero electronic angular momentum in the ground state $^1S_0$ and in the lowest energy metastable state $^3P_0$. The absence of angular momentum on these energy levels results in a decoupling of nuclear spin and electronic state (or orbital, analogous to electrons in solids), establishing each as an independent degree of freedom. This independence of atomic interactions from the spin-state corresponds to a SU(N) symmetry [22], N being the number of spin states. SU(N) symmetric systems can possibly realize exotic phases like spin liquids [23] or can be used to create highly entangled Dicke states offering an improved accuracy in spectroscopy experiments [24].

Furthermore, the two independent degrees of freedom and the SU(N) symmetry in fermionic AEAs and AEL atoms give rise to a direct spin-exchange interaction between two atoms in different electronic states occupying the same lattice site [25]. Here, the narrow clock transition can be used as spectroscopic tool to measure frequency shifts of interaction states or to probe their electronic state occupation over time, deriving spin-exchange energies and atomic interaction properties [26–28]. In condensed matter physics, orbital spin-exchange is related to quantum effects such as unconventional superconductivity in heavy fermion systems [29–32]. The spin-exchange interaction in combination with a differential Zeeman shift between ground state and metastable state enable to tune atomic interaction strengths via a novel (inter-)orbital Feshbach resonance [33–35]. Such a tunability extends the accessible parameter regime in experiments with two-electron atoms.

Theory proposals suggest AEL elements to realize complex quantum many-body systems [25,36–39] and quantum computing schemes [40–42]. One approach is to implement a state-dependent optical lattice which exploits the different ac-polarizabilities of ground and metastable state. The independent spin and orbital degrees of freedom and the interorbital spin-

exchange interaction then allow a realization of the Kondo lattice model [37,43–45]: Trapping metastable state atoms in deep lattice sites and allowing tunnelling for ground state atoms, the spin-exchange mechanism couples mobile to localized atoms. This is analogous to interactions between localized and mobile magnetic moments in solid-state materials, giving rise to the Kondo effect. Furthermore, confinement induced resonances can further tune the interaction strength. Another idea is to implement a state-dependent anti-magic lattice, where atoms in the different orbitals are confined in spatially shifted sublattices of the lattice laser intensity maxima, respectively minima. This allows to realize light assisted tunnelling between the lattice sites, creating strong synthetic magnetic fields and artificial gauge fields [46–48].

More examples of the rich physics that can be investigated with AEL atoms are $SU(N > 2)$ high-spin symmetry systems, which relate to quantum magnetism and exotic phases [23,38,46,49], and isotope mixtures of ^{171}Yb and ^{173}Yb which realize a novel $SU(2) \times SU(6)$ symmetry [50].

The Yb experiment at Hamburg University was established in 2009. The team realized the cooling of bosonic ^{174}Yb and fermionic ^{173}Yb to quantum degeneracy starting from an all-optical 2D/3D MOT setup [51–53]. At the end of 2013, at the beginning of my PhD, we measured first narrow-linewidth spectra of ^{173}Yb and spectra indicating spin-exchange interactions in the experiment. However, the resolution and signal to noise ratios of the spectra did not suffice to resolve individual scattering channels [53].
In 2015, we analysed a dissipative Fermi-Hubbard model using a reliable preparation method of the excited clock state, based on a rapid-adiabatic-passage scheme employing the ultranarrow transition [54,55].
Joining the team as fellow of an EU initial training network on quantum sensor technologies and applications, the focus of my work is on the clock laser system. I aimed for improved high-resolution spectra of the clock transition and to resolve spin-exchange interaction shifts in Yb lattice systems. In spring 2016, I realized significant improvements to the clock laser system by exchanging the high-Finesse resonator serving as frequency reference in the Pound-Drever-Hall (PDH) lock, implementing a fibre-coupled, waveguide-based EOM in the PDH lock, and rebuilding large parts of the clock laser setup. After these changes, I characterised the new clock laser system in detail and prepared it for spectroscopy measurements. In autumn 2016, we measured improved high-resolution spectra of the clock transition achieving a full width half maximum (FWHM) of 50 Hz. At the same time, we measured spectra clearly showing a feature resulting from spin-exchange interactions in ^{173}Yb, which are also shown in [55].
Lastly, the laser system for the 3D MOT was rebuilt enabling quantum gases with Yb isotope mixtures in the future and a 659 nm laser system for a state dependent lattice was integrated into the experiment [55–57].

In this thesis, I present my work on the clock laser system. I show the characterization of the rebuilt clock laser system, discuss improvements compared to the initial setup and indicate potential future improvements. I show the improved spectroscopic capability of the Yb experiment, presenting new high-resolution spectra and spectra showing features of spin-exchange interactions.

Chapter 2 gives an overview of the Yb experiment. It describes the cooling transitions of Yb, the experimental apparatus and the procedure to generate an ultra-cold atom gas of Fermionic ^{173}Yb in an optical lattice. Last, it shows the integration of the clock laser system in the experiment.

Chapter 3 discusses the clock laser system in detail. After an overview of the relevant parameters and components to reference the laser frequency to a cavity resonance via PDH locking technique, it describes the clock laser setup before and after reconstruction in 2016 and motivates the changes. The central new elements are an ultra-stable cavity made of ultra-low expansion (ULE) glass, a waveguide-based electro-optic modulator (EOM) and an additional photodiode to monitor residual amplitude modulation (RAM) noise and a new intensity regulation based on the beam power on cavity transmission, which are characterised in the following. With all parts of the laser system discussed individually, the PDH lock performance and the laser system's stability, based on the beat note measurements to an independently locked beam and on drifts against atomic resonance, are shown. The last section gives suggestions on future improvements to the clock laser system and its integration in the experiment.

Chapter 4 presents spectroscopy measurements of ultracold ^{173}Yb Fermi gases in the deep, magic-wavelength optical lattice. High-resolution single spin-component spectra show the achievable resolution of the clock laser in the experiment. Optical sideband spectroscopy measurements confirm a clean atom preparation and loading of several 10^4 atoms into the lowest band of the optical lattice. And first measurements of ultracold ^{173}Yb Fermi gases with two spin-components show a two-body spin-exchange interaction feature. Last, I suggest complementing measurements on Yb with the current experimental setup.

Chapter 5 summarises the capabilities of the experimental apparatus and the characterisation results of the clock laser system. In an outlook, I mention capabilities of the Yb experiment which are currently being implemented and look ahead to fascinating experiments that will be possible in the near future.

Chapter 2 Experiment Overview

In this chapter, I give an overview of the experimental setup and describe the generation of ultracold ^{173}Yb Fermi gases used for spectroscopy measurements. For extensive details on and characterizations of the setup, for general experimental parameters and for previously obtained results in the Yb project I refer to the PhD and master theses of my colleagues [52–59].

The first generation of PhD students, Sören Dörscher [52] and Alexander Thobe [53], designed and put the ultra-cold Ytterbium atom experiment in use. Together with the following PhD students, Bastian Hundt [54] and André Kochanke [55], and joined by me in mid-2013, we continuously enhanced the setup and performed experiments. While working together with the colleagues on all tasks and measurements conducted during that time, the focus of my work was the operation and improvement of the 578 nm clock laser system presented in this thesis. Regarding the setup, I took part in implementing the dichromatic dipole trap setup, in implementing and characterising an updated atom imaging scheme and in implementing and characterising a rapid-adiabatic-passage (RAP) scheme, which is presented in [54,55]. Many Bachelor and Master students, amongst others Torben Sobottke [59], Niels Petersen [58], Anna Skottke [57] and Benjamin Abeln [56], were supervised at and contributed to the Ytterbium experiment.

2.1 The Ytterbium experiment

At the centre of the experiment is a 2D/3D magneto-optical trap (MOT) and a subsequent optical dipole trap for evaporative cooling, published in [51], with which we can generate quantum-degenerate gases of Ytterbium (Yb). The alkali-earth-like element Yb has seven stable isotopes, two fermionic and five bosonic, most of which can be cooled to quantum degeneracy. Two electrons in its outer shell define its energy level structure, shown in Figure 1 a). For laser cooling and spectroscopy, the most relevant transitions are the 29 MHz broad $^1S_0$-$^1P_1$ transition at a wavelength of 399 nm and two of the (strongly) suppressed intercombination transitions to the ^3P manifold. The $^1S_0$-$^3P_1$ transition at 556 nm has a linewidth two orders narrower than the $^1S_0$-$^1P_1$ transition, enabling a Doppler cooling limit of 4,4 µK. This makes the 399 nm and the 556 nm transition a good combination for capturing and laser cooling atoms in two MOT stages. At this point we can use resonant pumping on the $^1S_0$-$^3P_1$ transition to redistribute the spin population in fermionic ^{173}Yb as desired. The Yb ground state does not allow for magnetic trapping. Therefore, we use evaporative cooling to quantum degeneracy in optical dipole traps, operating at 532 nm and 1064 nm wavelength. From there we load the ultra-cold atoms into an optical lattice at a “magic”-wavelength of 759 nm. The multiply forbidden $^1S_0$-$^3P_{0,2}$ transitions at wavelengths of 507 nm and 578 nm stand out with long life times of over tens of seconds and, correspondingly, narrow linewidths on the

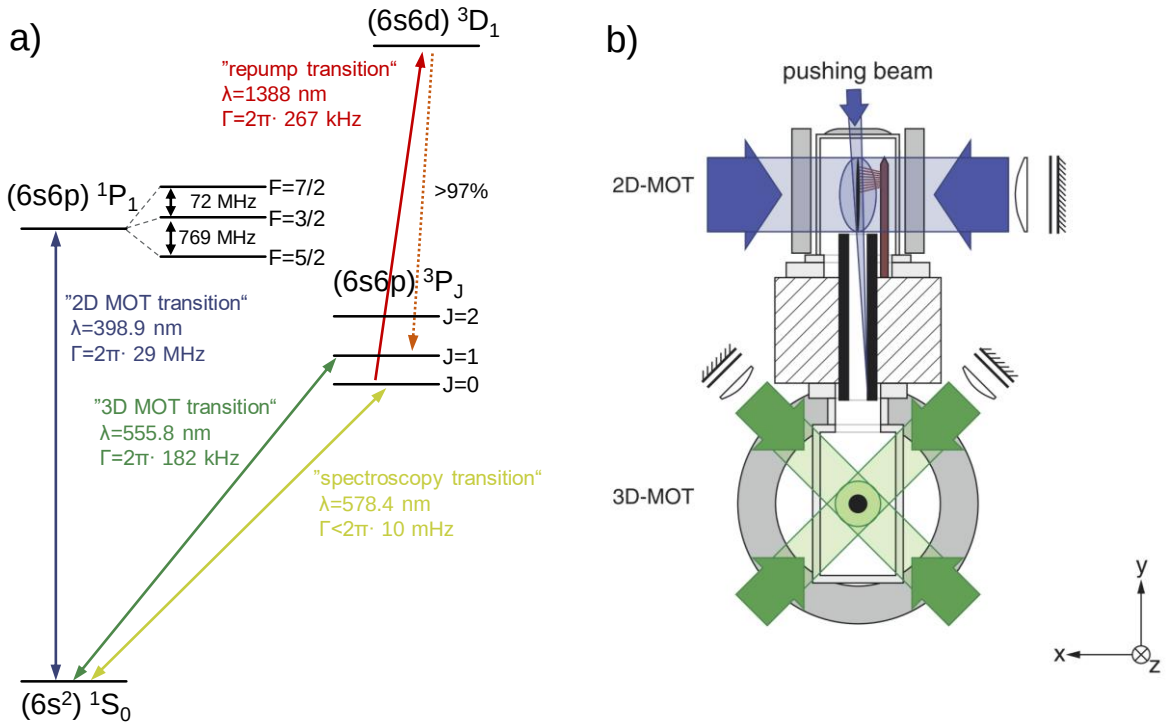

Figure 1: Yb energy level scheme and scheme of 2D/3D MOT setup. a) Energy level scheme and electron configuration of relevant laser cooling and spectroscopy transitions of Yb. Shown are the broad 2D MOT transition $^1S_0$-$^1P_1$ at 399 nm wavelength, the two orders narrower 3D MOT transition $^1S_0$-$^3P_1$ at 556 nm and the highly narrow spectroscopy transition $^1S_0$-$^3P_0$ at 578 nm. The hyperfine energy splitting for the $^1P_1$ state of the fermionic ^{173}Yb isotope is displayed. Our repumping scheme for $^3P_0$ excited state atoms uses the $^3D_1$ level, from where the atoms decay via the $^3P_1$ state into the ground state. Adapted from [51], distances not to scale. b) Scheme of experimental setup of 2D/3D MOT cells. In the top cell, a dispenser emits atoms into the blue 2D MOT. From the longitudinal 2D MOT, atoms transfer through a differential pumping stage into the lower "science" cell where they are captured in the green 3D MOT. This transfer is supported by an almost vertically aligned push beam hitting the lower part of the differential pumping stage. Setup scheme taken from [51].

millihertz scale [52,60]. These narrow transitions are used in optical clock and spectroscopy applications, giving them the name "clock states", respectively "clock transitions". In this experiment, we work with the $^3P_0$ state as excited, metastable clock state for spectroscopy. Performing spectroscopy on the clock transition is a direct approach to investigate many-body effects in Ytterbium. Lastly, we use absorption imaging on the 399 nm transition in combination with a repumper scheme, which transfers excited state atoms back to the ground state. This enables us to separately image atoms of both electronic states in one experimental cycle.

With this experimental apparatus we achieve non-trivial prerequisites for the study of many-body physics with quantum gases: We can reliably prepare clean, ultracold quantum gases of Ytterbium with well-defined spin populations and significant atom numbers loaded into the lowest energy band of an optical lattice. We can excite the metastable clock state with high resolution and reliably detect atoms in both, ground and excited energy state.

2.2 2D/3D MOT

Figure 1 b) shows the setup of two fused silica glass cells linked by a steel construction and surrounded by magnetic coils. A differential pumping stage connects the two cells. 55 l/s ion getter pumps and a titanium sublimation pump maintain a working pressure of 10^{-9} mbar in the upper and 10^{-11} mbar in the lower cell. In the top glass cell is the 2D MOT, operating as initial cooling stage. In the bottom glass cell, the "science cell", the rest of the experiment takes place, i.e. further cooling in a 3D MOT, atom spin repumping, followed by cooling to quantum degeneracy in an optical dipole trap, transfer into the optical lattice and the actual experiment.

The 2D MOT operates with two pairs of rectangular magnetic coils generating a quadrupole field with optimal 2D MOT field gradient of 55 G/cm. A dispenser emits Yb atoms from one corner of the glass cell into the 2D MOT. A low vapor pressure of Yb and its high adsorption to the glass cell require the 2D MOT to capture the atoms from the atomic beam, in contrast to alkali MOTs which can load from a background gas. The 2D MOT laser beams are 1 cm x 4 cm retro-reflected beams at 399 nm, corresponding to the $^1S_0$-$^1P_1$ transition, and operate at a red detuning of $\Delta_{2D} = -1{,}2\ \Gamma_{399\,\mathrm{nm}}$, with $\Gamma_{399\,\mathrm{nm}} = 29$ MHz, Γ being the transition linewidth. The beam shape roughly matches the dispenser emission geometry. The laser source for the 2D MOT is a commercial frequency doubled diode laser[1] with free-space access to the 2D MOT cell. The laser provides a beam power of about 180 mW in each arm. The 2D MOT laser frequency is stabilized by an offset lock to a diode laser[2]. The latter is locked by absorption spectroscopy to the same transition using an Yb atom beam. The diode laser also provides beams for absorption imaging along two imaging axes and a "push beam": Atoms in the 2D MOT are only cooled in the horizontal plane and their velocity in the vertical direction transfers them through the differential pumping stage to the 3D MOT in the "science" cell. The "push beam", slightly red detuned to the $^1S_0$-$^1P_1$ transition, enhances this transfer by about a factor of three.

The 3D MOT operates with two Anti-Helmholtz coils at a field gradient of 2 G/cm and a laser frequency detuning of about -7 MHz to the transition frequency. The 3D MOT operates on the narrow $^1S_0$-$^3P_1$ transition at 556 nm with transition line-width $\Gamma_{556\,\mathrm{nm}} = 182$ kHz. To increase the 3D MOT capture velocity, we spectrally broaden the laser beams by applying a triangular modulation of 7 MHz amplitude at 200 kHz frequency via AOMs in the beam paths. The three, circular 3D MOT beams have a 2 cm diameter and about 10 mW power each at the 3D MOT location. The beams are provided by a fibre-laser second-harmonic-generation (SHG) system[3]. The fibre laser is locked via optical phase-locked loop to a diode laser SHG system[4], which in turn is stabilized by Pound-Drever-Hall (PDH) lock to the resonance of a highly stable, ultra-low expansion glass (ULE) cavity. Light from the diode laser SHG system is also available for

[1] Toptica DL-SHG pro
[2] Toptica DL pro
[3] Menlo Orange one-SHG
[4] Toptica DL-SHG

a dual colour 3D MOT in the future, for photo association experiments and for optical Stern-Gerlach separation of spin states in later stages of the experiment.

For the bosonic isotope ^{174}Yb, we achieve MOT loading rates of $13 \cdot 10^6$ atoms per second, giving MOTs of 10^8 atoms after 10 s. Under a different beam and polarization alignment, optimizing the atom number, the fermionic isotope ^{173}Yb achieves loading rates of about $1{,}5 \cdot 10^6$ atoms per second and about $9 \cdot 10^6$ atoms after 10 s loading. The significantly lower loading rate of ^{173}Yb results from the lower natural isotope abundance and two unfavourable atom properties: First, in the 2D MOT, a close by energy level in the hyperfine splitting of the $^1P_1$ state allows only for a limited detuning capability. Second, in the 3D MOT, a large Zeeman shift between the ground and excited MOT states shifts negative m_F-states into a blue detuned energy range with respect to 3D MOT laser. Therefore, atoms in negative m_F-states are accelerated by the laser beams and lost from the MOT [53].

André Kochanke characterised of the current 2D/3D MOT setup in detail [55]. Furthermore, André Kochanke and Benjamin Abeln designed the laser setups to enable switching laser frequencies to match different Yb isotopes within an experimental cycle in the future [55,56].

2.3 Spin preparation

Before the beginning of evaporative cooling, we populate the spin components of a fermionic ^{173}Yb gas as desired by spin-selective optical pumping. While a magnetic field of 67 G induces a Zeeman splitting of the spin states, a circularly polarized, resonant beam on the $^1S_0$-$^3P_1$ intercombination transition (de)populates the individual states. Optionally, we can image the resulting spin distribution by applying an Optical Stern-Gerlach (OSG) separation of the individual spin states in a time-of-flight expansion measurement. The OSG beam is a circularly polarized beam close to the $F' = 7/2$ resonance of the intercombination transition. The atoms pass the OSG beam at its maximal slope and experience a spin dependent dipole force. They spatially separate after a brief time-of-flight, which we observe in an absorption image. Off-resonant atom scattering and a small separation of the lowest m_F states cause large error margins in quantitative analyses of the atom numbers in the currently implemented OSG detection.

2.4 Bichromatic Optical Dipole Trap

After loading the 3D MOT for 10-30 s the atoms are transferred into a bichromatic, crossed optical dipole trap at 532 nm and 1064 nm. To optimize the overlap, the 3D MOT atom cloud is compressed by increasing the magnetic field gradient to 10 G/cm and further cooled by disabling the spectral broadening of the 3D MOT beams, reducing the laser frequency detuning to -0,7 MHz, and reducing the laser power to a few percent of its initial capturing power. In the evaporative cooling process in the dipole trap, the 532 nm wavelength beam “DT1” (propagating along z-direction in Figure 1 b)) with 18 µm x 29 µm beam size and 9 W power initially dominates the trapping potential. The DT1 beam power is exponentially ramped down over 5 s to 25 mW, whereby the atoms accumulate in the crossed trap potential formed by the

two 1064 nm beams “IR1” and “IR2”. IR1 overlaps with DT1, has a circular beam diameter of 54 µm and 1 W power. IR2 propagates in x-direction, has an elliptical shape of 65 µm along y-direction times 220 µm along z-direction and a power of 10,5 W. In a second evaporation phase the beams IR1 and IR2 beam powers are exponentially ramped down over 8-15 s to 55 mW and 7,7 W, respectively. In parallel, the green DT1 beam power is ramped down to 10 mW over 2 s and then switched off. To avoid further evaporation, the IR beam powers are increased by 5 % above their minimal value at the end of the evaporation sequence.

A diode-pumped Nd:Yag laser[5] with free-space access to the glass cell provides the green dipole trap beam DT1. A Nd:Yag pumped MOPA[6] system provides the IR beams. Large mode area fibres[7] guide the IR beams to the experiment. All beams are intensity stabilised by monitoring photodiodes after the glass cell and feedback acting via the RF power applied to high power AOMs in the beam paths.

Working with a bichromatic dipole trap allows for good atom transfer from the MOT and fast initial evaporation within a deep dipole trap with large volume and large trapping frequencies. The initial trap depth is 616 µK against the direction of gravity. In a previous, all-green crossed dipole trap the average trap frequency was 91 Hz [52]. The second evaporation step in the infrared crossed dipole trap results in a more homogeneously distributed cold atom gas with average trap frequency of 36 Hz, enabling the transfer of two orders of magnitude more Fermions into the lowest band of an optical lattice in the next step [54,55].

After evaporation, we obtain essentially pure Bose-Einstein condensates of ^{174}Yb with 10^5 atoms. For fermionic ^{173}Yb with six spin components, we obtain quantum degenerate Fermi gas of 10^5 atoms at temperatures of $10-18\%$ of the Fermi temperature (T_F). For two spin-component Fermi gases and for spin polarized Fermi gases the evaporation efficiency decreases, and we obtain $5\cdot10^4$ atoms at temperatures of $20\%\,T_F$. Lifetimes (1/e time constant) of the degenerate gas in the dipole trap are over 40 s for ^{174}Yb and over 30 s for ^{173}Yb. These lifetimes are very long compared to an atom interrogation sequence lasting up to a few hundred milliseconds. Therefore, atomic losses due to the dipole traps can usually be neglected. Figure 2 a) and b) show time-of-flight images of a ^{174}Yb BEC and a ^{173}Yb DFG with six spin components.

2.5 Optical lattice

After evaporative cooling in the optical dipole trap, we transfer the atoms into the optical lattice. The optical lattice consists of a retroreflected 1D lattice along the z-direction, which is superimposed with the clock beam, and a 120° angle - triangular 2D lattice in the XY-plane. The polarization of the triangular lattice beams is set to be out of plane to obtain a triangular lattice, in contrast to the possibility of a hexagonal lattice at in-plane beam polarization [53,54,58]. The lattice is at the “magic” wavelength of 759 nm at which the polarizabilities and

[5] Coherent Verdi V18
[6] Coherent Mephisto MOPA 24W
[7] NKT Photonics LMA-PM-15

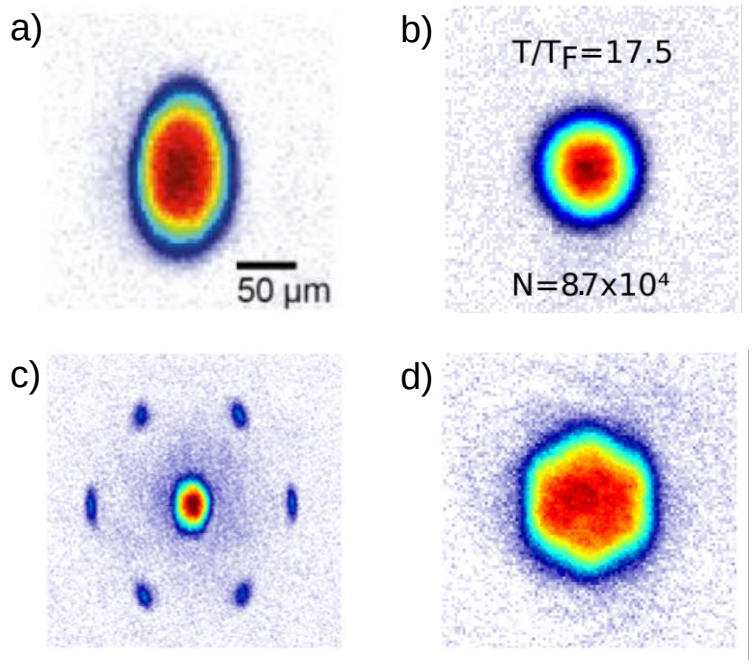

Figure 2: Typical Yb quantum gas images. a) Image of a ^{174}Yb BEC with $2 \cdot 10^5$ atoms after TOF. b) Typical image of a quantum degenerate Fermi ^{173}Yb six-component spin mixture with $9 \cdot 10^4$ atoms at temperature of $0{,}18\ T_F$ after TOF. c) ^{174}Yb BEC released from a triangular 2D lattice after TOF, showing distinct diffraction peaks. d) Band-mapping image of a six-component Fermion ^{173}Yb cloud in a triangular lattice filling the lowest lattice band, thus showing the hexagonal 1st Brillouin zone. Images b) - d) also shown in [55].

therefore AC light shifts of the trapping potential are the same for the ground state $^1S_0$ and the excited state $^3P_0$ [61,62]. In this way, spectra of the clock transition are not broadened due to the intensity profile of the lattice beams.

A Ti:Sa laser system[8] provides about 1 W power in a beam with 84 µm waist for the 1D lattice and 400 mW power at each 2D lattice beam with waists of 93 µm. The lattice beam powers are monitored and stabilized via the RF power applied to an AOM in each beam path. Digital DDS RF frequency sources for the AOM frequencies provide a high phase stability of the individual beams for the optical lattice. This setup proved to be more phase-stable in experiments than with a voltage controlled oscillator - based fibre noise cancellation system as AOM frequency sources [54]. A FNC setup based on a digital frequency source is in preparation and could further improve the phase stability of the lattice.

The effective lattice depths are up to $150\ E_r$ for the 1D lattice and up to $50\ E_r$ for the triangular 2D lattice, with E_r being the recoil energy for Ytterbium in the optical lattice. We operate in the deep Lamb-Dicke regime, at which the strong spatial confinement in the optical lattice suppresses motional excitations of atoms by the spectroscopy laser. Figure 2 c) shows a time-of-flight (TOF) image of a superfluid ^{174}Yb BEC released from the triangular optical lattice. The individual peaks indicate the discrete lattice momenta of BEC in superfluid state within

[8] Coherent Verdi V18 and MBR 110

the optical lattice. Figure 2 d) shows a band mapping image of a spin-polarized ^{173}Yb DFG in the triangular optical lattice, indicating occupation of the first Brillouin zone.

2.6 Imaging

We can take images of the atom cloud with a standard absorption imaging scheme along two perpendicular directions in the horizontal plane (x- and y-axis), operating on the blue, 399 nm $^1S_0$-$^1P_1$ transition. We derive the atom cloud image from an atom absorption image, a reference image (without atoms) and a dark image (without the imaging laser). The blue transition has a large transition linewidth, enabling an insensitivity of the atom count against laser frequency fluctuations. The transition further allows working with well detectable beam powers while remaining below the atom saturation intensity. On the x-axis, the imaging resolution is limited by the camera's pixel edge length of 13 µm and an objective magnification of 4,71x. Detection on the z-axis is impinged by optical distortions of the beam being transmitted through several mirrors, introducing aberrations and interferences. The pixel edge length is 6,7 µm and the objective magnification is 2,2x.

In the experiment, fluctuations in the setup's performance introduce shot-to-shot fluctuations of the total atom number loaded on the order of 15%. Being able to determine relative excitation numbers in clock spectroscopy significantly reduces the influence of atom number fluctuations and improves the signal to noise ratio in the recorded spectra. We use a "repumping" scheme transferring the excited state atoms back to the ground state, enabling us to detect them with our absorption imaging scheme present. The excited state ($^3P_0$) atoms are transferred to the $^1S_0$ ground state by exciting them to the $^3D_1$ state, indicated in the energy level scheme in Figure 1 a). From the $^3D_1$ state, the atoms decay to the $^3P_1$ state and from there on the 556 nm intercombination transition to the ground state. Looking at the decay channels and decay rates of the $^3D_1$ state after an illumination of the excited $^3P_0$ atoms for 1 ms, over 97,5% of the atoms transfer to the ground state. The remaining 2,5% of $^3P_0$ atoms decay into the metastable $^3P_2$ state where we consider them as lost. The excitation light for the $^3P_0$-$^3D_1$ transition is provided by a 1388 nm distributed-feedback diode (DFB) laser[9] with about 2 mW laser power at the atoms. The laser frequency is broadened to a spectral width of about 10 GHz to ensure a good power spectral density in case of small laser frequency drifts and to cover all spin states. Lacking a suitable frequency reference in the laboratory, the DFB laser frequency operates free-running. Monitoring its emission frequency shows a sufficiently high frequency stability over weeks of operation. The atoms successfully transferred to the ground state are imaged at 399 nm. Due to the spatial separation during time of flight of the atom cloud, this atom absorption image for the formerly excited atoms simultaneously serves as reference image for the atoms initially in the ground state. Correspondingly, the first absorption image of the atoms initially in the ground state also serves as reference image for the repumped excited atoms.

[9] NTT Electronics NLK1E5EAAA

2.7 Integration of the clock laser in the experiment

An experimental sequence for spectroscopy on ultracold ^{173}Yb takes about 50 seconds. To be able to perform spectroscopy with a resolution on the order of 100 Hz, this results in demanding stability requirements of the clock laser system and its integration in the experiment: We need a laser coherence time over tens of milliseconds for individual spectroscopy pulses and a high frequency stability over the up to two-hour-long duration of a spectroscopy series.

The 578 nm clock laser for high resolution spectroscopy on the $^1S_0$-$^3P_0$ transition is a diode based SHG system[10], which is presented in detail in Chapter 3. The clock light is guided to the experiment via a fibre link with VCO based fibre-noise-cancellation (FNC) to ensure a phase stable transmission of the laser light through a 10 m long optical fibre. Vibrations and local temperature changes could otherwise introduce phase noise onto the clock beam. The FNC AOM stabilizes the beat frequency of a local oscillator branch with a reflected part of the clock beam coming from the experiment table. Figure 3 shows the implementation of the clock beam at the experimental table, which was planned and realized by Bastian Hundt [54]. The FNC reflex results from the 0th order of an AOM running at fixed frequency after the fibre. A mirror located on a monolithic aluminium block which also holds the 1D lattice retro-reflex mirror creates the reflected beam. In this way, we extend the phase-stabilized beam path as far as possible and simultaneously relate the stabilized phase of the clock laser to the frame of reference of the 1D lattice holding the atoms. We also use the FNC AOM to switch the clock laser pulse at the experiment. We set the required beam power at the atoms via the RF power applied to the AOMs and, if necessary, by using an additional neutral density attenuator placed just before the 1D lattice retro-reflex mirror. However, in the current setup, we do not actively monitor the beam power of the clock laser at the experiment. The clock laser has a beam waist of $2\omega_0 = 200$ µm ($1/e^2$ intensity) at the atoms.

The AOM on the experiment table can also be used to produce frequency sweeps for clock excitations by rapid-adiabatic passage, implemented and used in measurements by Bastian Hundt [54].

[10] Toptica SHG Pro

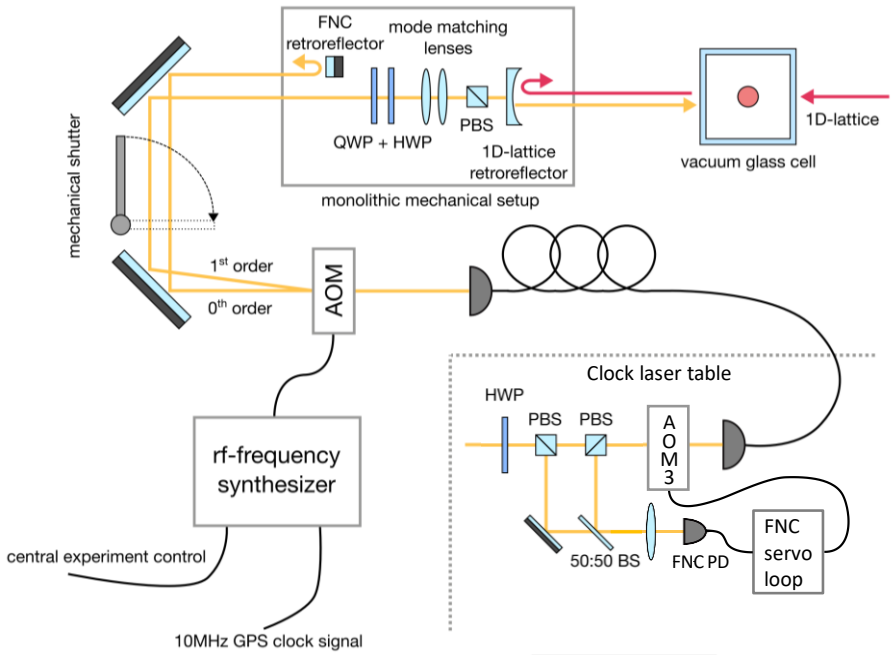

Figure 3: Schematic of the 578 nm clock beam integration in the experiment. A fibre noise cancellation setup stabilizes the clock beam fibre-link to the experiment. The 1D lattice mirror and the FNC retroreflex mirror are mounted on a rigid aluminium block to reduce relative motion between lattice and clock pulse. The FNC feedback AOM ("AOM 2") also switches the clock beam pulse. An AOM on the experiment table usually operates at fixed frequency. It can be used to run frequency sweeps of the clock laser. Polarization alignment and modematching optics fit the clock beam (exiting the fibre with circular polarization) to the experiment. Adapted from [54].

Chapter 3 Clock Laser System

To exploit the coherent control over the electronic state in our experiments, we need a clock laser system with sufficient coherence time and power.

We estimated our demands to the clock laser's coherence time, respectively linewidth, on the spectroscopy features we want to measure: The interaction-induced energy shifts of the clock transition are typically on the order of few kHz. Spectra showing such interaction shifts therefore should have a resolution of about 100 Hz. This results in a laser linewidth on the order of 10 Hz to provide high spectral purity and enable high-contrast spectroscopy measurements. This shows that the laser's coherence time needs to be significantly longer than the pulse length for typical measurements with large Rabi frequency.

A sufficient laser power enables working with a large beam waist which provides a homogeneous intensity distribution at the atoms. This suppresses dephasing from an inhomogeneous Rabi frequency. With the Rabi frequency relating to the beam power by $\Omega/\sqrt{I} = 77$ Hz with $[I] = \mathrm{mW\,cm^{-2}}$ for Ytterbium [63], one can also achieve kHz Rabi frequencies with a power of few mW. Working with a large Rabi frequency and correspondingly a short π-pulse duration can be useful when wanting to observe fast processes. This comes in trade for the achievable spectroscopy resolution as the effective transition linewidth also scales with the square-root of the beam power.

We utilize laser frequency stabilisation techniques established in the atom spectroscopy and clock community achieving (sub-) hertz linewidths and minimal frequency drifts [18–21]. To reduce the linewidth of a laser, a reference and feedback mechanism is needed. Due to the narrow linewidth of the clock transition and correspondingly weak spectroscopy signals, (doppler free) spectroscopy techniques cannot be applied here. Instead, we reference the laser frequency to the resonance of a high-finesse cavity [64] by a Pound-Drever-Hall (PDH) lock [65,66]. In a PDH lock, a phase modulated laser beam at the cavity resonance frequency is reflected off the cavity and impinges onto a fast monitoring photodiode. The monitored signal consists of the modulation sidebands, which are completely reflected off the cavity, and of the partly reflected, phase shifted carrier coming from the cavity. The resulting beat signal contains a frequency dependent error signal for the laser lock. Extracting that error signal and giving a corresponding correction back to the laser enables us to narrow the laser linewidth from about 100 kHz of a free running laser down to the single or sub-hertz level in the PDH lock. As the error signal is generated from the interference of the modulation sidebands with the cavity resonance, the PDH lock can be regarded as a phase lock between the incoming light and the light stored in the cavity, with the cavity acting like a flywheel [64]. Therefore, a PDH lock achieves frequency corrections far beyond the cavity resonance linewidth. The cavity provides

a highly stable frequency reference on short and intermediate timescales, where quantum noise (spontaneous emission) and minimal fluctuations or distortions (at the laser diode current, temperature and vibrations) in the free-running laser cause a frequency broadening of its emission. The cavity needs to be isolated from external influences such as temperature and pressure fluctuations. Drifts inherent to the cavity material require another frequency reference, such as an atomic reference, an GPS stabilised oscillator signal or an absolute optical frequency reference signal, to stabilize the laser frequency on timescales of hours and more [67,68].

Chapter overview

This chapter discusses and characterises the clock laser setup and its individual elements as follows:

Chapter 3.1 introduces relevant parameters to discuss the Pound-Drever-Hall lock of the clock laser. It looks at the performance requirements for the electronics in the lock to achieve a single hertz linewidth.

The laser and the electronics of the PDH lock, i.e. the PDH photodiode, the signal generation and -processing electronics, and the feedback elements – in this setup an external cavity diode piezo in the laser's master oscillator and a fast acousto-optic modulator – are the same as in the initial clock laser setup built by Alexander Thobe. He evaluated the PDH lock in detail, including its noise, gain and phase characteristics, and showed a 1,1 Hz linewidth short-time level laser performance of the initial setup, presented in his thesis [53]. Chapter 3.2 describes this initial setup, its overall performance and new findings on the setup and its drawbacks.

Chapter 3.3 presents the rebuilt clock laser system, with the central, new elements being an ultra-stable cavity completely made of ultra-low expansion (ULE) glass, a waveguide-based electro-optic modulator (EOM) and an additional photodiode to monitor residual amplitude modulation (RAM) noise. Chapter 3.3.1 gives an overview of the setup. Then I look at approaches to improve the cavity characteristics. Next, the new cavity is characterised in detail: Chapter 3.3.3 presents a finite element method simulation on the temperature expansion characteristic of the new cavity. And chapter 3.3.4 gives experimental results of the new cavity's characteristics in detail and its integration in the setup, such as the performance of the temperature stabilisation.

The last vital part for the PDH lock is the phase modulation of the beam going to the cavity. Chapter 3.4.1 presents the new fibre-coupled waveguide-based EOM and shows its advantages to the previously used free-space EOM. With all individual components discussed, chapter 3.4.2 presents the characteristics of the PDH lock.

A stable operation of the clock laser with minimal frequency fluctuations also requires a beam power stabilisation at the cavity, characterised in chapter 3.5. Chapter 3.6 presents further minor details in the new setup and considerations on the reduction of residual amplitude modulation noise.

Chapter 3.7 shows a first performance evaluation of the clock laser system. The beat note between two clock beams independently locked to two cavity systems informs about the combined laser linewidth and frequency fluctuations, especially valid on short and intermediate time scales. A day-long monitoring of the beat frequency between the two cavity beams shows the combined frequency fluctuations and drifts of the two cavity systems. In the last subsection, we determine long-term drift of the cavity from the laser's frequency settings to match the clock transition in spin-polarized ^{173}Yb observed over several days.

Chapter 3.8 discusses approaches for future improvements of the clock laser system and its integration in the experiment as well as additional, improved characterization measurements.

The FEM simulation of the cavity was done by me. The redesign of the clock laser system was planned by me, with advice of André Kochanke and Bastian Hundt. The setup improvements and characterization measurements were done and evaluated by me, with experimental support of André Kochanke at the cavity exchange, at measuring the cavity's CTE-ZC temperature and at the fibre EOM's RAM temperature dependence. All spectroscopy measurements were recorded and evaluated by André Kochanke and me.

3.1 Theory considerations for PDH laser locking

Cavity parameters

The PDH lock links the frequency stability of the laser to the cavities resonance frequency and therefore its mechanical length stability. This is expressed in equation (3.1).

$$\frac{\Delta L}{L} = -\frac{\Delta \nu}{\nu} \tag{3.1}$$

L is the (non-expanded) cavity length, ΔL is the change in cavity length, ν the resonance frequency and $\Delta \nu$ the change in resonance frequency. In our system, the cavity length is $L = 77{,}5 \pm 0{,}1$ mm, the laser frequency about $\nu \approx 518{,}2946$ THz.

Relation (3.1) shows that distortions such as mechanical vibrations, pressure fluctuations or thermal expansion of the cavity directly reflect onto the laser frequency. To minimize distortions from the environment, the cavity is surrounded by temperature-controlled heat shields and mounted in a vacuum system at a pressure of about 10^{-8} mbar. Additionally, the whole cavity setup is placed on a vibration isolation platform.

Important cavity characteristics are its finesse, free spectral range, and its linewidth. Finesse and linewidth inform about the quality of the resonator and about its losses due to absorption events in and transmission through the cavity mirrors. The free spectral range $\Delta \nu_{FSR}$ gives the frequency difference between two successive longitudinal optical modes.

$$\Delta \nu_{FSR} = \frac{c}{2 \cdot L} \tag{3.2}$$

c is the speed of light. We assume a refractive index of 1 at low pressure in the vacuum system.

The spectral width of the Lorentzian shaped cavity resonances, the cavity (FWHM) linewidth $\delta\nu$, is directly related to the exponential decay time τ of light stored in the cavity. The decay time τ is measured in a cavity ringdown measurement, recording the decay of light intensity leaving the cavity after abruptly switched off the light going to the cavity. A narrow linewidth corresponds to an increased frequency discrimination of the cavity, which also results in an increased slope of the PDH lock error signal on resonance.

$$\delta\nu = \frac{1}{2\pi \cdot \tau} \tag{3.3}$$

The cavity finesse $\mathcal{F}$ is the ratio of the free spectral range $\Delta\nu_{FSR}$ by the cavity linewidth (FWHM) $\delta\nu$, shown in equation (3.4). A larger finesse means stronger contrast, such as in narrow Fabry Perot patterns, higher frequency selectivity and stronger intracavity resonance power. The finesse of self-built resonators is about 10^2 to 10^3, while that of high-finesse resonators is on the order 10^5 and above.

$$F = \frac{\Delta\nu_{FSR}}{\delta\nu} = \Delta\nu_{FSR} \cdot 2\pi \cdot \tau \tag{3.4}$$

The round-trip power loss, $(1-\rho)$, can be obtained by numerically solving equation (3.5).

$$\mathcal{F} = \frac{\pi}{2 \cdot \arcsin\left(\frac{1-\sqrt{\rho}}{2\cdot\sqrt[4]{\rho}}\right)} \tag{3.5}$$

PDH Lock

We reference the laser frequency to the cavity resonance by a Pound-Drever-Hall (PDH) lock. The PDH locking technique is similar to frequency modulation spectroscopy and well established since its publication in 1983 [65]. Here, I focus on few details helping the discussion of the setup. For detailed explanations I recommend the references [65,66].

The PDH error signal results from the beat of the carrier with the first modulation sideband. This reflects in the frequency discriminant D of the error signal, shown in equation (3.6).

$$D \equiv -\frac{8\sqrt{P_c \cdot P_s}}{\delta\nu} \tag{3.6}$$

Here, $P_c = J_0^2(\beta) \cdot P_0$ is the carrier power, $P_s = J_1^2(\beta) \cdot P_0$ is the power of one sideband of first order and $\delta\nu$ is the cavity linewidth. The carrier and sideband intensities scale from the total incoming power P_0 with the squared Bessel functions $J_0(\beta)$, resp. $J_1(\beta)$, with β being the modulation depth. The maximum frequency discriminant is at a modulation depth of $\beta = 1{,}08\ \text{rad}$. The course of this function is approximately that of a top half circle and thus has a broad peak. Exemplarily, a modulation depth of $\beta = 0{,}25\ \text{rad}$ yields 60% of the maximum value for the frequency discriminant.

In the setup, an electro-optic modulator (EOM) driven by a sinusoidal voltage signal provides the phase modulation of the beam. The effective modulation depth thus depends on the voltage applied and on the efficiency of the modulator, often expressed in a voltage required for a phase shift of π. We set the EOM's modulation frequency to be significantly larger than the cavity

linewidth and such that the modulation sidebands are far away from other cavity resonances. The EOM in our PDH setup is a fibre-coupled waveguide-based EOM running at 17,8 MHz modulation frequency and at ideal modulation depth of 1.08 rad, characterized in chapter 3.4.1.

PDH electronics requirements

Achieving a (sub-)hertz linewidth in a PDH lock sets high requirements in gain, noise, bandwidth, phase, and time delay to the involved components. Here, I discuss these requirements to the components, i.e. detector, signal processing elements and transducers.

The beam reflected off the cavity is monitored by the PDH photodetector. This photodetector needs a sufficient bandwidth to detect the relevant signal at modulation frequency (in our case at ≈ 18 MHz) with high sensitivity and low noise characteristic. Ideally it should operate above shot noise limited sensitivity, which is at 0,8 µW impinging beam power. In our setup about 10 µW beam power impinge onto the photodetector.

To obtain the DC error signal for the PDH lock, the signal of the PDH photodetector is mixed down with the phase-matched local oscillator (LO) signal at modulation frequency. This error signal is fed into a differential voltage input of a proportional-integral-derivative (PID) controller generating the feedback to the control elements of the laser. The individual PID controller elements are fine-tuned to achieve an optimal locking performance, adjusting the lock position in the error signal and balancing gain, bandwidth, and stability of the lock.

General performance requirements to the control elements for laser locking at the hertz linewidth level are described in [53,69], and briefly recapitulated here: The frequency noise spectrum of a laser determines its linewidth, i.e. the full width half maximum of the power spectral density (PSD_E) of the laser. Equation (3.7) shows that the PSD can be expressed as the Fourier transform of the autocorrelation function of the electric field $E(t)$, which includes the frequency noise by the noise spectral density $|\rho_\nu(f)|$.

$$PSD_E(\nu) = 2\,E_0^2 \cdot \int_{-\infty}^{\infty} \exp(i \cdot 2\pi\,(\nu_0 - \nu)\,\tau) \cdot \exp\left(-2 \cdot \int_0^{\infty} |\rho_\nu(f)|^2\,\frac{\sin^2(\pi f \tau)}{f^2}\,\mathrm{d}f\right)\mathrm{d}\tau \qquad (3.7)$$

ν is the frequency at which the PSD is evaluated with ν_0 the central frequency, E_0 is the electric field magnitude, τ is the autocorrelation lag. The Fourier relation in the autocorrelation function includes the noise integrated over the whole spectrum, making the relation non-trivial for experimental applications. Only for a flat noise density ($\rho_\nu(\nu) = \rho_0$), the PSD returns a Lorentzian curve with FWHM $\Delta\nu = \pi \cdot |\rho_0|^2$. Therefore, a linewidth of $\Delta\nu = 1$ Hz corresponds to a flat noise spectrum at the level $\rho_0 = 0.56\ \mathrm{Hz}/\sqrt{\mathrm{Hz}}$.

This upper noise boundary for the laser noise needs to be held at low frequencies of the laser in lock, as these contribute to the noise close to the carrier frequency in the laser spectrum.

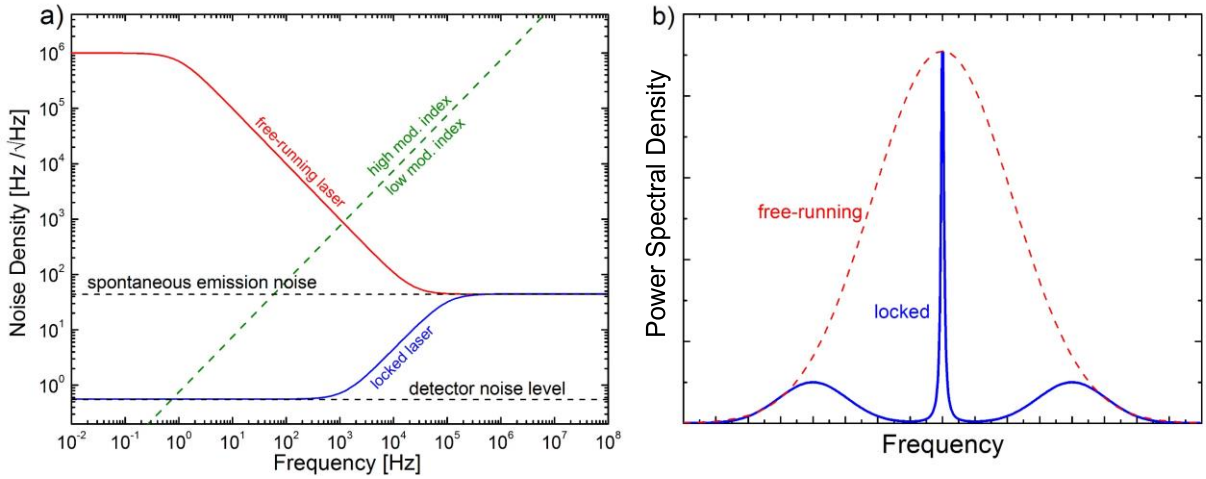

Figure 4: Schematic noise density spectrum and power spectral density plots a) Schematic noise density spectrum for a free running laser (red), a locked laser (blue). The spontaneous emission noise level is shown in black, the boundary between high and low modulation index of the noise is shown in green. b) Schematic power spectral density plots of a free-running and a locked laser. A free running laser has a broad gaussian line shape resulting from low-frequency noise. The frequency feedback of the lock reduces low-frequency noise, resulting in a narrow carrier in the power spectral density of the laser. Not suppressed high-frequency noise causes small side-peaks in the power spectral density. Taken from [53].

Qualitatively, this case of 'high modulation index noise' applies to noise which amplitude (in hertz) is larger than its frequency. Figure 4 shows schematic noise density spectra and corresponding power spectral density plots for a free running and a locked laser. The noise amplitude can be expressed in units of hertz when combining the detected signal with the detector sensitivity and error signal slope. In contrast, noise at high frequencies contributes to sideband features in the laser spectrum. If these sidebands are far away from any spectral features under investigation they can be neglected. This second case of 'low modulation index noise' corresponds to noise amplitudes being lower than the corresponding noise frequency. This consideration relaxes the lock regulation bandwidth over which the low noise level for a 1 Hz linewidth is required [69].

The noise spectrum of the free-running laser determines the requirements to the PID controller generating the feedback and the transducers enacting such. Technical noise, such as noise in the diode pump current, temperature fluctuations and mechanical vibrations, dominates the low frequency noise spectrum of the laser. The spectral noise density of technical noise can be on the level of $\approx 1\ \mathrm{MHz}/\sqrt{\mathrm{Hz}}$ for low frequencies and strongly decreases with increasing frequency. At large frequencies (over 10^5 Hz), the dominating noise is quantum noise, caused by spontaneous emission in the laser diode and by losses in the resonator. That quantum noise gives a flat noise spectrum, leading to the Schawlow-Townes linewidth limit [70,71]. For external cavity diode lasers (ECDLs), the quantum noise level is typically at tens of $\mathrm{Hz}/\sqrt{\mathrm{Hz}}$, corresponding to a linewidth of a few kHz.

These noise and bandwidth properties set the gain, phase and bandwidth requirements of the controller and transducers. Reducing the noise from the $1\ \mathrm{MHz}/\sqrt{\mathrm{Hz}}$ level of a free-running

laser to the $0{,}56\ \mathrm{Hz}/\sqrt{\mathrm{Hz}}$ level for 1 Hz linewidth requires a controller gain of 120 dB. The gain must be reduced to below unity before the phase of the loop transfer function reaches -180°, otherwise the controller feedback would make the regulation lock unstable. In an 1st order low pass loop filter, which reduces the gain by 20 dB/decade and a phase lag of -90° in the transfer function, this requires a control bandwidth of 1 MHz. Differentiating between high and low modulation index noise relaxes the bandwidth requirement to the kHz order.

All elements in the PDH lock, i.e. PDH photodetector, the signal transfer and control elements and the transducers, need sufficiently large bandwidths to process the signals and to provide feedback with minimal delay. Ideally, each individual element's bandwidth is more than an order of magnitude above the envisaged regulation bandwidth.

3.2 Initial clock laser setup

3.2.1 Setup description

Optical Setup

Rodolphe Le Targat, Christoph Becker, Alexander Thobe [53], Thomas Rützel [72] and Jan Carstens [73] planned and realized the initial clock laser system. The principle of the overall setup remains the same and is recapitulated here. Figure 6 depicts the updated setup, which also suits as reference for the initial clock setup.

The "clock" laser is an amplified frequency doubled external cavity diode laser system[10] with output power of 300 mW at 578 nm. The output beam is split into two branches to be able to establish two independent PDH locks to independent, similar cavity setups, called cavity 1 and cavity 2. The branch to cavity 1 is used for our spectroscopy experiments and will be at the centre of this discussion. The branch to cavity 2 is used for reference measurements of the clock laser, presented in section 3.7.1.

In the cavity 1 branch, a 200 MHz AOM[11] (AOM 1) acts as transducer for fast PDH lock regulation. The beam is then split into a branch to generate the PDH locking signal, and a branch to the experiment and frequency monitoring setups. In the latter, a fibre-noise-cancellation (FNC) stabilized fibre link guides the beam to the experiment. The FNC acts via AOM3, stabilizing the beat with a local oscillator branch monitored by a photodiode (FNC PD). Frequency monitoring of the cavity 1 beam is possible by a wave meter[12] and by beat measurements with a frequency comb[13] or with a beam stabilized to the second cavity.

In the PDH locking branch, the beam passes a 200 MHz AOM (AOM 2) used for intensity stabilisation, drift compensation and for shifting the laser frequency with respect to the cavity. The AOM is controlled via a computer-controlled DDS board[14] referenced to a 10 MHz GPS stabilized oscillator to avoid drifts of the laser frequency. A 0,5 m long fibre link (single mode, not polarization-maintaining) guides the beam onto a vibration isolation table[15] on which the PDH setup is located.

The following paragraph describes the setup on the vibration isolation table as in use until the cavity replacement beginning of 2016: After the outcoupler, a non-polarizing beam splitter sends half the beam power towards a photodiode[16] for intensity regulation. The feedback loop was a self-built PI-board acting onto the RF power of AOM 2. A Glen Tayler polarizer ensured a clean beam polarization. A free space EOM[17] with two electro-optic crystals at Brewster angle generated the modulation sidebands for the PDH signal. The modulation signal at $\Omega_{mod} = 17.8\,\mathrm{MHz}$ was supplied by a function generator[18], amplified by a commercial

[11] Crystal Technology 3200-121
[12] HighFinesse/Angstrom WSU-10U
[13] Menlo Systems FC-1500
[14] Analog Devices AD9959
[15] MinusK 150BM-1
[16] Thorlabs PDA36A
[17] Linos PM25 VIS
[18] Agilent 33500B

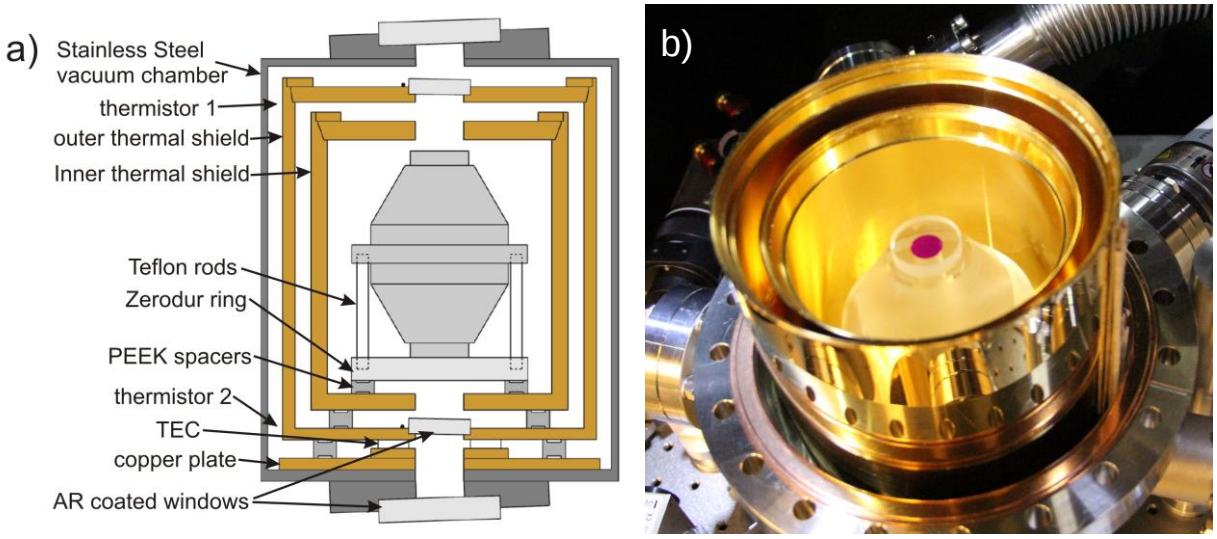

Figure 5: Schematic depiction and photo of the cavity in the vacuum setup. a) shows the vertically, mid-plane mounted cavity in the vacuum chamber enclosed by two thermal shields. The materials for mounting rods, ring and spacer are chosen to minimize heat conduction. The outer heat shield is mounted on a TEC for temperature control. One thermistor on the top side and one at the bottom side of the outer heat shield are used for temperature sensing. Taken from [53]. b) shows a photo of the cavity in the vacuum system during the cavity exchange.

RF amplifier and fed to the EOM via a self-built LC resonator circuit. Mode matching optics and an isolator to reduce possible etaloning effects were placed between EOM and cavity. The cavity is located inside a vacuum chamber and within temperature stabilized heat shields, discussed below. The transmitted beam could be monitored by a CCD camera to verify operation at the TEM_{00} mode and by a photodiode[19] (PD2) when optimizing the mode match. The beam reflected off the cavity was picked up at the isolator output and focussed onto an 80 MHz avalanche photodiode[20] (APD) giving the PDH PD signal. This signal is mixed with a local oscillator (phase-locked to the EOM modulation signal) generating the PDH lock DC error signal. The error signal is processed by a PID module[21] of the laser driver, acting with a fast feedback branch (10 MHz maximum bandwidth and 80 dB maximum gain, acting in the setup up to ≈ 1 MHz frequency) onto AOM 1 and with a slow feedback branch (maximum DC gain of 120 dB, acting in the setup up to ≈ 10 kHz) onto the master laser ECDL piezo.

Vacuum setup & Temperature control

The vacuum system, shown in Figure 5, was designed by Alexander Thobe [53] and Thomas Rützel [72]. It was adapted from a setup developed by the Hänsch group [64]. The setup remained essentially unchanged since its initial construction. The cavity is enclosed by two gold coated copper cylinders acting as heat shields and housed in a stainless-steel vacuum chamber. An ion getter pump maintains a pressure of about $5 \cdot 10^{-8}$ mbar. The materials between the shields and supporting the cavity (Teflon rods in a Zerodur ring, spacers made of

[19] Thorlabs PDA36A

[20] Femto HCA-S with Si APD Detector, customized model

[21] Toptica Fast Analog Linewidth Control (FALC 110)

PEEK) were selected to have minimal heat conductivity. A Peltier element between the vacuum chamber and the outer heat shield enables an active temperature stabilisation. It is regulated by a self-built temperature controller outside of the vacuum system, adapted from the design in [74]. Regulation feedback is provided by two 10 kiloohm negative temperature coefficient thermistors located at top and bottom of the outer heat shield. The thermistors are connected in series, to obtain an average temperature signal of the heat shield. The resistance signal is fed through the vacuum system to the temperature controller, where it is part of a Wheatstone bridge which generates the error signal. PI controllers on the board (designed with large integration time) then generate a feedback signal for the Peltier element.

3.2.2 Cavity characteristics and performance of the initial setup

The cavity was set up by Alexander Thobe [53] and Thomas Rützel [72] in 2009. It is the vertically, mid-plane mounted "football" geometry cavity assembly[22] developed in the group of Hänsch [64], bought from the company Advanced Thin Films (ATF). The spacer material was ultra-low expansion glass (ULE), which coefficient of thermal expansion (CTE) has a zero crossing near room temperature [75]. The mirrors were made of fused silica (FS)[23]. The consideration for FS mirrors may have been a reduced thermal noise in fused silica mirrors, reducing the power sensitivity by factor two, approximately [76]. However, due to different thermal expansion coefficients of ULE and FS, thermal stress has a large contribution to the cavity's effective coefficient of thermal expansion [77]. This stress decreases the CTE zero-crossing temperature by several tens of degrees [78]. For the cavities bought in 2009, the zero-crossing temperature was evaluated to be around $T_0 \approx -27°\,\mathrm{C}$ [53,58]. Due to deteriorating effects of large temperature gradients expected in the vacuum setup and a limited cooling power of the Peltier element it was not possible to work at that low temperature. Operating at a temperature of 7° C, a temperature sensitivity of the cavity resonance frequency of about $35\ \mathrm{kHz/mK}$ was deduced. This is several magnitudes more sensitive than operating close to a cavity's zero-crossing temperature. The temperature regulation board achieved a peak-to-peak stability on the order of $200\ \mu\mathrm{K}$ in 24 hours but also showed fluctuations up to $100\ \mu\mathrm{K}$ within 30 minutes. In combination with the heat shield's temperature low pass characteristics, having an exponential approach with time constant $\tau \approx 37\ \mathrm{h}$, short term fluctuations were expected to be averaged out. Still, significant nonlinear drifts of the cavity resonance frequency of 80 Hz on experimentally relevant timescales around 20 minutes and longer were present (see Fig. 3.15 in [53]). Furthermore, fast frequency fluctuations over tens of hertz on timescales of few seconds were observed. These fast fluctuations likely resulted from laser intensity fluctuations impinging on and coupled into the cavity, especially affecting the thermal expansion of the mirrors' anti-reflection coatings [79]. The sensitivity of the cavity resonance frequency to intensity variations was $3{,}45 \pm 0{,}38\ \mathrm{kHz/\mu W}$ (with respect to the transmitted power), which

[22] ATF 6030

[23] as we realized after publication of Alexander Thobe's thesis [53].

is again extremely large compared to similar setups [63,79,80], and showed an exponential approach with time constant $\tau \approx 1{,}5$ s.

Cavity ringdown measurements as well as measuring the transmission while scanning over the resonance frequency gave a cavity full width half maximum linewidth of $\Delta\nu_{FWHM} \approx 12.1$ kHz and a finesse of $\mathcal{F} \approx 150\,000$ for cavity 1. A mode matching coefficient of $\epsilon = (84 \pm 7)\%$ was derived from the beam powers transmitted and reflected from the cavity. The PDH lock achieved a regulation servo bandwidth of about 900 kHz with a linear detector sensitivity of 19 µV/Hz on resonance. The lock enabled linewidths of $1{,}1$ Hz over two second periods and $10 - 20$ Hz for periods up to one minute [53]. The laser stability was evaluated by a beat with a second beam independently locked to a similar, reference cavity. The narrow short-time line-width agrees with the laser noise characteristics.

3.2.3 Drawbacks of the initial setup

The intensity regulation as implemented in the initial setup monitors the total intensity on the vibration isolation table, independent of the polarization. Due to polarization cleaning elements following, rotations of the polarization axis of the light resulted in amplitude changes. This was not compensated for in the initial setup. A cavity's thermal expansion and therefore its resonance frequency are highly sensitive to the total in-coupled power [53,63,79,80] and even slightly sensitive to beam powers only impinging onto the cavity [79]. Therefore, intensity fluctuations are highly disadvantageous to the laser's frequency stability.

The free space EOM, containing a bulk birefringent crystal, requires a large voltage of 1000 V ± 10% applied across the crystal for a polarization rotation of $\lambda/2$. Assuming a linear dependence of the crystals polarization rotation on the voltage applied, this equals a large RMS voltage of 243 V for a sine wave to achieve a modulation depth of $\beta = 1.08$ with this EOM. At this modulation depth, the PDH error signal discriminator D (given in equation (3.6)) is maximised relative to the optical power at the photodiode. Even with a good driving signal amplification of about 10x in an LC circuit before the free space EOM, only a modulation depth of $\beta \approx 0{,}48$ could be achieved [73]. This corresponds to only achieving about 65% of the possible PDH error signal. A smaller frequency discriminator results in a PDH lock which is less sensitive to frequency deviations of the laser with respect to the cavity resonance.

Furthermore, it was not possible to stabilize the temperature or an offset voltage across the crystal of the free space EOM in the original setup. This allowed for additional (slow) rotations of the crystal axes with the environment temperature, resulting in a varying, mismatched polarization alignment between the impinging light and the crystal axes. On one hand, it results in polarisation rotations which result in amplitude variations of the total light power due to polarization selective elements in the beam path. Furthermore, residual amplitude modulation noise (RAM) causing additional fluctuations of the monitored PDH signal is significantly larger without temperature stabilisation of the EOM. RAM noise decreases the laser's frequency stability and will be discussed in the chapters 3.4.1 and 3.6.1.

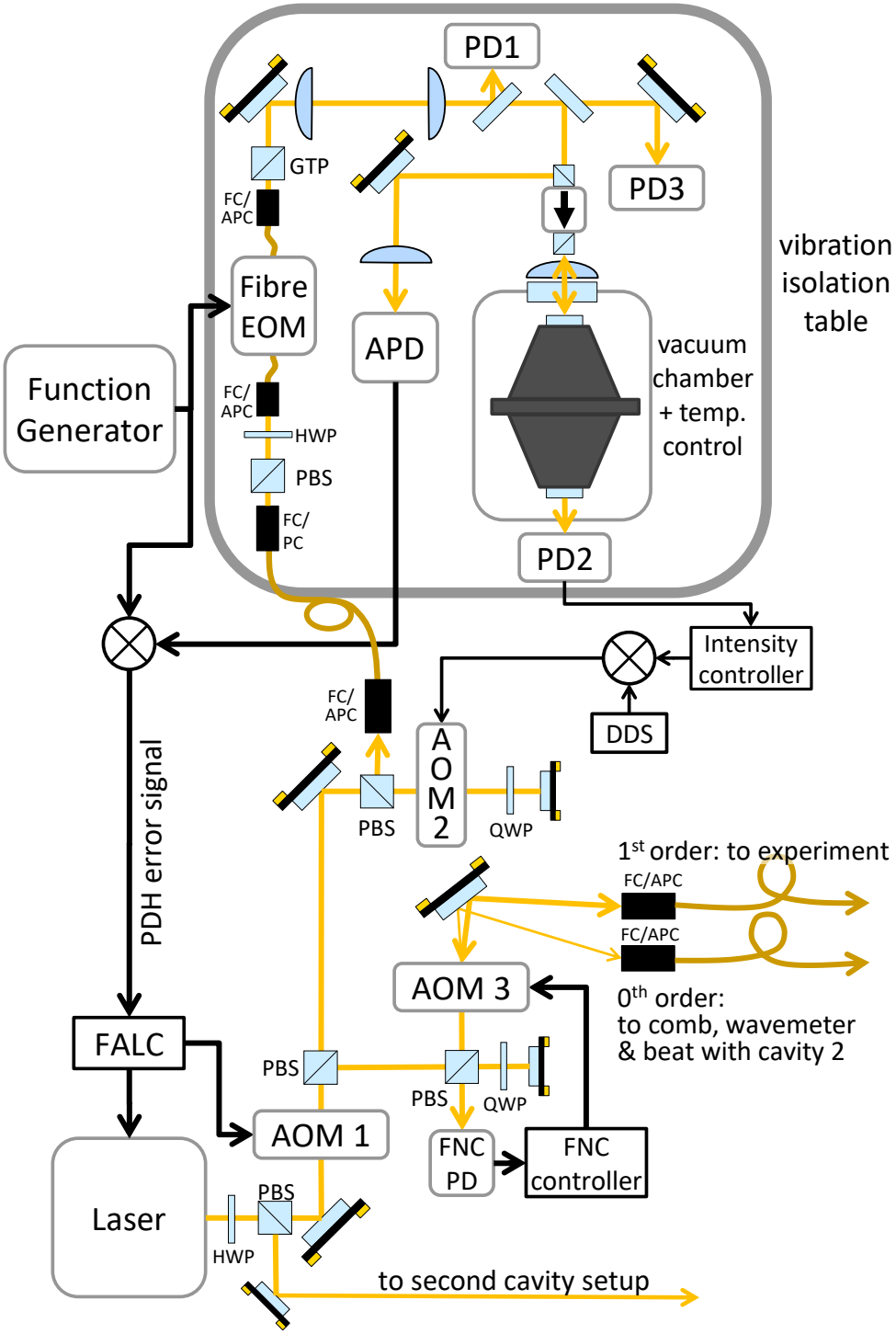

Figure 6: Scheme of the new clock setup, omitting most modematching optics for clarity. AOM 1: +80 MHz AOM as fast frequency correction element in the cavity 1 PDH lock; AOM 2: 2·(-210) MHz AOM for frequency shift, drift correction, intensity regulation; AOM 3: −80 MHz AOM for FNC operation and switching light pulses at the experiment; FNC PD: Fast photodiode for FNC beat monitoring; PD1: Intensity monitoring photodiode[25]; PD2: Transmission photodiode[27] for intensity stabilisation; PD3: RAM monitoring photodiode[26]; APD: Avalanche photodiode[20] for PDH signal; HWP/QWP: Half/Quarter wave plate, PBS: Polarizing beam splitter; GTP: Glan-Taylor Polarizer; FC/(A)PC: Fibre Coupler for (Angled) Polished Contact fibre; ⊗ : frequency mixer; DDS: Direct Digital Synthesizer; FALC: Fast, analog PID controller; Function Generator[18]: signals for PDH modulation and local oscillator signals for PDH & RAM, with tuneable phase shift; Fibre EOM: Waveguide-based EOM with PM fibres[24], temperature stabilized.

3.3 Rebuilt clock setup and new cavity 1

In 2013, the Yb team performed a series of spectroscopy measurements on the $^1S_0 - {}^3P_0$ "clock" transition of Ytterbium in a magic optical lattice. These measurements also showed us the performance of the overall experiment and the "initial" clock setup in particular [53]. In spin-polarized and thus non-interacting Fermions, we managed to record Fourier limited spectra with a minimal resolution of 192 Hz (FWHM of Lorentz fit to the spectrum). This is larger than the expected power broadened linewidth and the laser's short-time linewidth of 1,1 Hz. We attributed the limited resolution achieved to a limited frequency stability of the clock laser.

Furthermore, we performed spectroscopy measurements on interacting two-orbital spin mixtures of ^{173}Yb in an attempt to determine important interaction parameters for ^{173}Yb, in particular the two inter-orbital scattering lengths U_{eg}^{+} and U_{eg}^{-} [26,53]. With these measurements we simultaneously evaluated the capabilities of the clock laser to resolve occupation- and state-dependent on-site shifts of the clock transition. In first measurements we observed additional excitations compared to single component spectra [53], which fit to the expected frequencies based on scattering lengths published by groups in Munich [26,34] and Florence [27]. However, the stability of our laser setup was not sufficient to resolve the individual features in the spectra on its own.

We implemented many improvements to the experiment to address drawbacks encountered in these measurements and enhance our capabilities. Exemplary are the bichromatic optical dipole trap to achieve low trapping frequencies, homogeneous samples and more stable atom numbers [54,55], a repump laser enabling counting atom numbers of the ground and excited state [55] and the stabilisation of the clock laser to the optical lattice retroreflector [54] to suppress Doppler shifts between clock laser and lattice.

Looking at the clock system, we assumed that the large temperature sensitivity of cavity 1 is the cause for strong nonlinear drifting behaviour on intermediate and long timescales. Furthermore, we assumed that the cavity's large sensitivity to beam power fluctuations is also linked to the large stress on the cavity mirrors, resulting from operating far away from its temperature of zero-expansion. Therefore, we decided to address the cavity itself to resolve these problems arising from its low zero-crossing temperature of thermal expansion. Opening the vacuum system to access the cavity was also an opportunity for me to rebuild the clock laser setup. Especially on the vibration isolation table I could resolve the problems in the initial design mentioned in the previous chapter.

This chapter gives a comprehensive overview of the new clock setup, starting with a setup description in the next section. The subsequent sections focus on the cavity: In subsection 3.3.2, I discuss two approaches to resolve the cavity's low thermal expansion zero-crossing temperature. Then I show results of a FEM simulation on the thermal expansion of the cavity model with spacer and mirrors made of ultra-low expansion (ULE) glass. In subsection 3.3.4 I show the experimental characterization results of the new, all-ULE cavity.

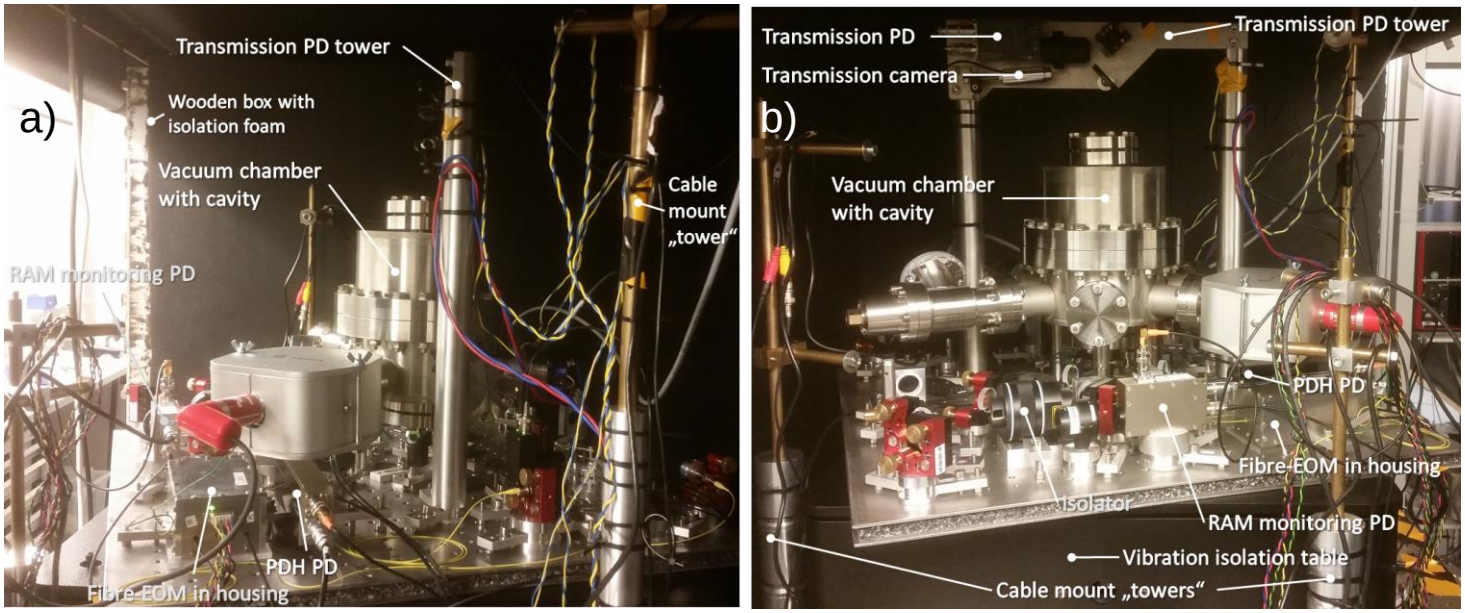

Figure 7: Photos of the rebuilt clock setup around the cavity and vacuum chamber on the vibration isolation table, with labels to major components visible. The wooden box with noise isolation foam surrounding the setup form the black background. The intensity monitoring pickup and photodiode before the cavity are not present in these photos.

3.3.1 Overview of new clock 1 setup

Rebuilding the clock cavity setup included rearranging all components on the vibration isolation table, exchanging the free-space EOM with the fibre-coupled EOM, adding a monitor RAM photoreceiver to the setup and changing details such as a rigid mount for the cavity transmission photoreceiver and adding cable holding mounts to reduce vibrations.

Following is a description of the new setup on the vibration isolation table. The setup is schematically depicted in Figure 6 and shown in photos in Figure 7. After exiting the fibre collimator, the beam passes a polarizing beam splitter ensuring a defined linear polarization and a 50/50 beam splitter for intensity monitoring with a passive photodiode. The transmitted beam passes a half-wavelength waveplate and is coupled into the fibre EOM[24] which generates the sidebands for the PDH lock. After the EOM, the beam passes a Glenn Taylor polarizer, a two-lens telescope reducing the beam diameter, and a pickup mirror with 83% reflectivity. The reflected beam is used for intensity monitoring[25]. The transmitted beam impinges on another pickup mirror with 75% reflectivity. Here, the transmitted arm is focussed onto a fast photodiode[26] for RAM monitoring at the modulation frequency. The reflected beam, going to the cavity in the vacuum system, passes an isolator and a focussing lens which matches the beam to the cavity mode. The beam reflected off the cavity is picked up after passing the isolator in reverse and focussed onto a fast avalance-photodiode[20] generating the PDH signal.

[24] Jenoptik PM594 with PM APC fibres
[25] Thorlabs PDA36A
[26] Femto HCA-S custom, 40 MHz Low Noise Optical Receiver with Monitor Path

The beam transmitted through the cavity is split up by a pellicle beam splitter (8% reflection, 92% transmission). A sensitive photodiode[27] and a CCD camera monitor the transmitted light, both rigidly mounted on an arch-like support construction to minimize possible vibrations.

3.3.2 Cavity improvement choices: ULE rings or new cavity

Legero et al. [78] showed in 2010 that the large effect on a cavity's coefficient of thermal expansion zero-crossing (CTE-ZC) temperature, which results from deformations due to the material mismatch of ULE spacer and FS mirrors, can be compensated by optically contacting ULE rings to the back sides of the cavity mirrors. The rings enable a cavity with CTE-ZC at room temperature and effectively about three times lower thermal noise, compared to an all ULE cavity. Unfortunately, implementing this feature did not apply to our existing cavity and setup. The backsides of our cavity mirrors had an insufficient polishing degree for optical contacting. Furthermore, a short distance to the heat shields surrounding the cavity would have been a problem. Lastly, the clock laser and the second cavity setup were in daily use for the experiments conducted. A downtime of several months of our cavity setups could not be scheduled.

The alternative option was to buy new cavities with more suitable material properties. We decided to buy the same cavity model, this time with spacers and mirrors made of ULE glass. By going for the same cavity model, we avoided time consuming changes to the setup, especially for a new vacuum chamber and heat shields, otherwise necessary. By pre-selecting the material batch for the spacer, a spacer CTE-ZC temperature within 10°C to 30°C could be guaranteed by *ATF*. However, the company could not produce the cavity mirrors out of the same material batch of ULE. As variations in the material result in slightly different zero-expansion temperatures, the combination of different ULE batches for spacer and mirrors results in a shift of the effective temperature of minimal expansion. To verify that the cavity's effective temperature of minimal expansion still would be around room temperature, I modelled the cavity's thermal expansion by FEM analysis. The modelling and results are explained in the following chapter.

3.3.3 FEM simulations of the cavity's thermal expansion

FEM simulation model

For the FEM simulations, I followed the papers [78,81].

The linear coefficient of thermal expansion (CTE), $\alpha(T)$, relates a change in temperature dT to the length change dL of a bulk material:

$$dL = L \cdot \alpha(T) \cdot dT \tag{3.8}$$

[27] Femto LCA-S-400K-SI

The coefficient of thermal expansion of a bulk material, $\alpha(T)$, itself can be modelled with a quadratic temperature dependence close to its zero-crossing temperature.

$$\alpha_{ULE}(T) = a \cdot (T - T_0) + b \cdot (T - T_0)^2 \tag{3.9}$$

With a, b being the linear and quadratic expansion coefficients, T the material temperature and T_0 the zero-crossing temperature of the CTE. Material properties for Ultra Low Expansion Glass (ULE) and Fused Silica are given in Table 3.1.

For a resonator construction, the effective CTE, α_{eff}, is the sum of spacer expansion with coefficient α_s and an additional, axial mirror displacement due to deformation, dB. The axial displacement of the mirrors is modelled as result from the mirrors bulging under radial expansion of the mirror material while being rigidly fixed on the spacer with different expansion coefficient. The axial displacement is related via a linear coupling coefficient δ to the difference of the radial expansion of the mirrors to that of the spacer. The partial length change of the resonator, dL, due to a change in temperature dT is given in equation (3.10).

$$\begin{aligned} dL &= L \cdot \alpha_s(T) \cdot dT + 2 \cdot dB \\ dL &= L \cdot \alpha_s(T) \cdot dT + 2 \cdot \delta \cdot R \cdot [\alpha_m(T) - \alpha_s(T)] \cdot dT \end{aligned} \tag{3.10}$$

Where L is the spacer length, R the mirror radius and the subscripts s for spacer, m for mirror.

Relating equation (3.10) and equation (3.8) gives the effective coefficient of thermal expansion of a cavity, shown in equation (3.11).

$$\alpha_{eff}(T) = \alpha_s(T) + 2\delta\frac{R}{L}[\alpha_m(T) - \alpha_s(T)] \tag{3.11}$$

The relative length change $\Delta L(T)/L$, shown in (3.12), results from integration of equation (3.10) over temperature.

$$\begin{aligned} \frac{\Delta L(T)}{L} &= \int_{T_{0,cav}}^{T} \alpha_{eff}(T)\, dT \\ &= \frac{a_s}{2}\left(\left(T - T_{0,s}\right)^2 - \left(T_{0,cav} - T_{0,s}\right)^2\right) + \frac{b_s}{3}\left(\left(\mathrm{T} - \mathrm{T}_{0,s}\right)^3 - \left(T_{0,cav} - T_{0,s}\right)^3\right) \\ &+2\,\boldsymbol{\delta}\,\frac{R}{L}\left(\left(\frac{a_m}{2}\left(\left(T - T_{0,m}\right)^2 - \left(T_{0,cav} - T_{0,m}\right)^2\right) + \frac{b_m}{3}\left(\left(\mathrm{T} - \mathrm{T}_{0,\mathrm{m}}\right)^3 - \left(T_{0,cav} - T_{0,m}\right)^3\right)\right)\right. \\ &\left. -\left(\frac{a_s}{2}\left(\left(T - T_{0,s}\right)^2 - \left(T_{0,cav} - T_{0,s}\right)^2\right) + \frac{b_s}{3}\left(\left(\mathrm{T} - \mathrm{T}_{0,s}\right)^3 - \left(T_{0,cav} - T_{0,s}\right)^3\right)\right)\right) \end{aligned} \tag{3.12}$$

The integral of (3.8) for the spacer (first and third sum term) is highlighted in green, that for the mirrors (second summation term) in blue. With subscript s for spacer, m for mirrors, cav for cavity. L is the spacer length, R the mirror radius, $\boldsymbol{\delta}$ is the coupling coefficient for axial length deformation (bulging) of mirrors due to radial stress, $T_{0,x}$: zero crossing temperature of element x, $T_{0,cav}$; deformation-free temperature of cavity assembly (assembly temperature assumed to be 20° C).

The coupling coefficient δ is independent of temperature and thermal expansion coefficients. It only depends on the structure and geometry of the assembly as well as on mechanical materials properties (Youngs modulus, density, Poisson's ratio). To analytically describe the cavity's thermal length expansion, δ is the only unknown. It is obtained by fitting equation (3.12) to FEM simulation data of the cavity expansion. Effectively, I simulated the cavity's length deformation (at the centre of the mirrors) for various temperature steps, starting from an arbitrarily chosen cavity assembly temperature at $T_{0,cav} = 20°\,\mathrm{C}$.

I did not include the mirror coatings in these simulations as they only minimally contribute to a shift of the CTE-ZC temperature [81]. However, the coatings significantly contribute to the thermal noise and to the light power dependence of the cavity resonance frequency, with estimated drifts on the order of $20\ \mathrm{Hz/mK}$ [64,77].

FEM simulation procedure

In practice the FEM software[28] ignored temperature dependent changes of material properties when simulating large temperature steps[29]. To circumvent this, only temperature steps of 1 K from a non-deformed cavity system were simulated and material parameters and temperatures adapted accordingly. The distance to the centre of the mirrors was taken as on-axis deformation. I determined the cumulative axial deformation ΔL by trapezoidal integration of the individual deformations, with the offset (arbitrarily) chosen such that zero deformation would occur at $T_{0,cav} = 20°\,\mathrm{C}$. Material properties are given in Table 3.1.

To obtain the resulting relative deformation $\Delta L/L$ over temperature, I fitted the cavity thermal expansion model in equation (3.12) to the simulation data, with no additional fitting parameters required. Testing this procedure on the model of a cylindrical cavity with one ULE and one FS mirror as analysed in [78], we obtained comparable values for the structural constant of $\delta \approx 0.35$ and the minimal temperature sensitivity at 10.8 °C, which is well within the error range of the result published.

FEM simulation results for an all ULE cavity

Next, I performed the FEM simulation for the "football" cavity completely made of ULE. The resulting relative cavity deformation over temperature is shown in Figure 8. Fitting equation (3.12), we obtained a structural constant of $\delta \approx 0.42$. Simulating a cavity with ULE spacer having a CTE-ZC at 10° C and ULE mirrors with CTE-ZC at 35 °C gives an effective cavity CTE-ZC temperature at 13.8 °C.

Knowing the structural constant δ, I analytically evaluated the cavity's thermal expansion for various combinations of spacer and mirror ULE CTE-ZC temperatures. We wanted to know if the cavity's effective CTE-ZC temperature would be within the operation range of our Peltier setup. So, I tested the combinations of spacer and mirrors CTE-ZC temperature with both being at the (same) upper/lower specified extrema. And to know about temperature shifts, I checked

[28] Autodesk Simulation Mechanical 2015

[29] This seems to be a recurring problem, as it was also mentioned in reference [81].

the combinations of spacer and mirrors CTE-ZC temperatures being at the opposite extrema specified.

For the cavity spacer, *ATF* guaranteed the CTE-ZC temperature to lie between 10° C and 30° C. For the mirrors, *ATF* used Corning "Premium Grade" ULE with a mean CTE within 0 ± 30 ppb/°C in the range of 5 to 35 °C [75]. Table 3.2 shows the calculated temperature shifts resulting from the combination of different thermal expansion coefficients for spacer and mirrors. In all cases, the shift was below 4° C away from the spacer's CTE-ZC temperature. Thereby, the effective cavity CTE-ZC temperature would be close to room temperature. This result is also confirmed in a technology note by M. Notcutt at *Stable Laser Systems* [82]. We thus could expect to operate the new cavity at its CTE-ZC temperature, being around room temperature, with the existing thermoelectric cooler and vacuum setup.

Temperature sensitivity

The cavity's CTE, given in equation (3.10), is the base function of the thermal length expansion. Thus, the cavity's CTE gives its temperature sensitivity at certain temperature. As the relative length change of the cavity is proportional to the relative change of the resonance frequency, as shown in equation (3.1), the temperature sensitivity can be expressed in units of Hz/K.

Figure 9 plots the sensitivity of the cavity's resonance frequency in dependence of the temperature difference between the cavity operation temperature and its CTE-ZC temperature. The shown temperature sensitivity plot is valid for all temperature combinations of an all ULE cavity, the deviations from the CTE-ZC temperature variations between spacer and mirrors are insignificantly small. At a temperature difference of $1\ \mathrm{K}$ between cavity operation and the CTE-ZC, the temperature sensitivity of the cavity resonance frequency is about $1{,}2\ \mathrm{kHz/mK}$. At a difference of $0{,}1\ \mathrm{K}$, the expected temperature sensitivity is about $100\ \mathrm{Hz/mK}$.

We assume to be able to adjust the cavity's temperature within 1° C to its CTE-ZC temperature in the estimated region around room temperature. The estimate given here can be compared to the experimentally determined temperature sensitivities of the 'initial' cavities with ULE spacer and FS mirrors operated far away from the CTE-ZC temperature: for "initial cavity 1" the sensitivity was $-35\ \mathrm{kHz/mK}$ at a temperature difference of $\Delta T \approx 34\ \mathrm{K}$ [53], and for "cavity 2" the sensitivity was $-26\ \mathrm{kHz/mK}$ at $\Delta T \approx 27\ \mathrm{K}$ [58].

With the general requirement of the cavity CTE-ZC temperature to be close to room temperature expected to be met by all ULE cavities, we ordered new cavities for the clock setup. The experimentally determined CTE-ZC temperature and sensitivity of the new, all-ULE cavity 1 are presented in the following sections.

Property	Unit	ULE [81]	Fused Silica [78,83]
Density	10^9 g/cm³	2,21E-09	2,20E-09
Young's modulus	N/mm²	67600	72700
Poisson number	-	0,17	0,16
CTE: *a*	1/K²	2,21E-09	2.2E-09
CTE: *b*	1/K³	-1,22E-11	0
CTE at ≈ 20°C	1/K	0	5,00E-07
CTE-ZC T_0	° C	10 ... 30	-207

Table 3.1: Material properties of ULE and FS used in FEM simulations.

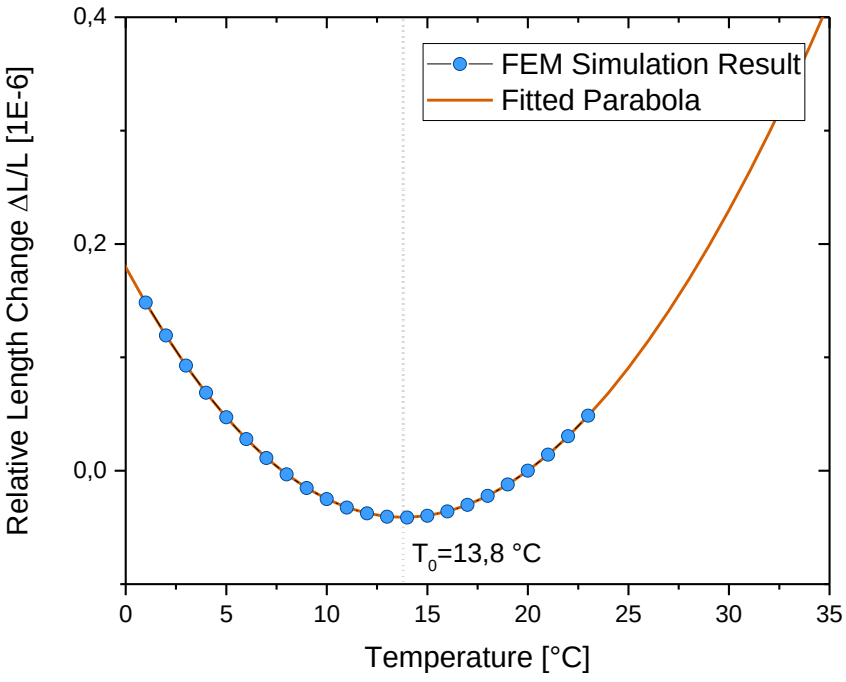

Figure 8: FEM simulation result of the relative length change of the ATF "football" cavity, with all components made of ULE, as a function of temperature. The dots give the FEM simulation results, the red line (parabola) shows the fit of equation (3.12), giving the structure constant of $\delta \approx 0.416$. In this FEM simulation, the spacer temperature of minimal thermal expansion $T_{0,s}$ was set to $T_{0,s} = 10$ °C and the mirror CTE-ZC temperature was set to $T_{0,m} = 35$ °C. The effective temperature of minimal thermal expansion of the cavity is at $T_{0,cav} = 13.8$ °C, shifted by $+3.8$ °C away from the spacer temperature of minimal expansion.

Combination of spacer and mirror CTE-ZC temperatures	CTE-ZC temperatures			Shift ΔT [°C] from spacer $T_{0,s}$
	Spacer $T_{0,s}$ [°C]	Mirror $T_{0,m}$ [°C]	Resulting Cavity $T_{0,cav}$ [°C]	
Spacer low T_0, mirrors high T_0	10	35	13,8	+3,8
Spacer high T_0, mirrors low T_0	30	3	26,8	−3,2
Spacer and mirror high T_0	30	45	32,2	+2,2
Spacer and mirror low T_0	10	3	9,1	−0,9

Table 3.2: The effective temperature of minimal thermal expansion (CTE-ZC temperature) of a cavity with all components made of ULE, in dependence on the CTE-ZC temperatures of the spacer and mirrors, as well as the temperature shift with respect to the spacer minimal expansion temperature. In all cases, the shift away from the spacer CTE-ZC temperature is only a few degrees, such that it will be possible to operate the cavity at its effective CTE-ZC temperature around room temperature.

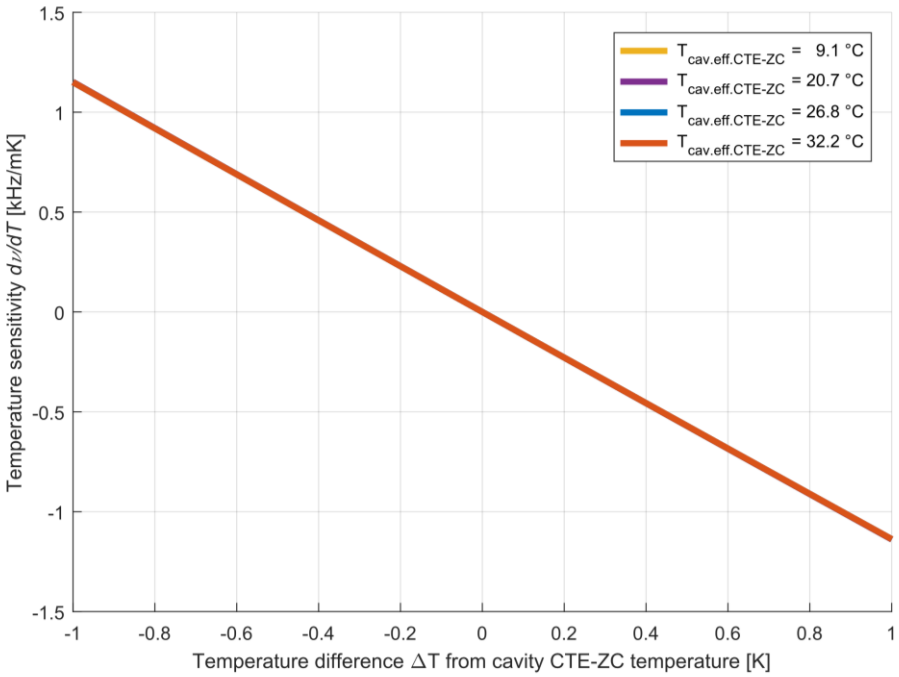

Figure 9: Analytical temperature sensitivity of the cavity resonance frequency close to the cavity's effective CTE-ZC temperature. The change in sensitivity has a linear slope of about $-1.2\ \mathrm{kHz/mK^2}$ for the relevant region considered here. The variation of the cavity sensitivity curve in proximity to the cavity CTE-ZC temperature by different combinations of cavity and spacer CTE-ZC temperatures is vanishingly small.

3.3.4 Cavity Characterization

In this section, I present the experimentally determined characteristics of the new cavity in the rebuilt "clock 1" PDH lock setup.

First, I determined the cavity finesse F by measuring the cavity ring-down time τ, i.e. the exponential decay time of the light transmitted out of the cavity after switching off incoming light. Finesse and ring-down time relate as shown in equation (3.4). The exponential decay time resulting from several measurements recorded several months after evacuation of the vacuum system is $\tau = 17.85 \pm 0.03$ µs. Figure 10 shows an exemplary measurement, together with the exponential fit $f(t) = A \cdot \exp(-t/\tau) + y_0$ and the near-instantaneous switching off characteristic recorded with a photodiode in front of the cavity. The resulting finesse is $F = 216\,900 \pm 400$, which fulfils the demands to an ultra-high finesse cavity.

The free spectral range of our cavity is $\Delta\nu_{FSR} = 1{,}934 \pm 0{,}003$ GHz. We derive it from the cavity length, as shown in equation (3.2). From the ringdown measurement and the free spectral range, we derive the cavity linewidth $\delta\nu$ using equation (3.3). The cavity linewidth is $\delta\nu = 8.92 \pm 0.01$ kHz.

The round-trip power loss of $(1 - \rho) = 29 \cdot 10^{-6}$ is obtained from the finesse by numerically solving equation (3.5).

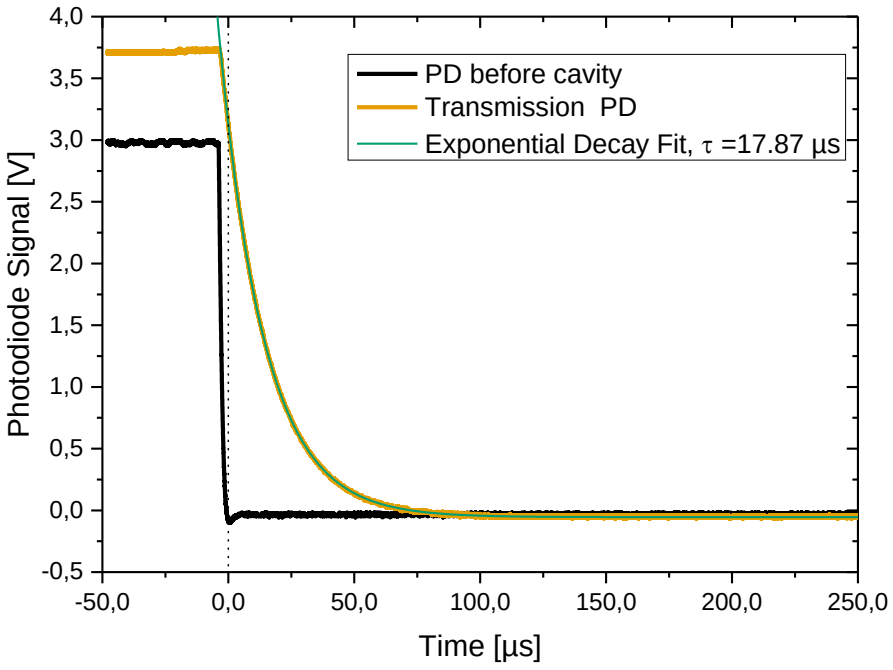

Figure 10: Example measurement of decay of light intensity stored in the cavity (orange line), exponential decay fit (green) to the decay giving a time constant of $\tau = 17.85$ µs and the switching characteristic given by a photodiode measuring the light in front of the cavity in a pickup path (black). The switching characteristic is nearly instantaneous compared to the transmission delay. The exponential decay was fitted to times $t > 0$ only, when no more light was present in front of the cavity.

Mode match

The beam exiting the fibre EOM is collimated to a diameter of $1{,}9 \pm 0{,}1$ mm intensity at 1/e² level. The beam diameter is then reduced with a 4:1 telescope and focussed with a lens of 300 mm focal length onto the first cavity mirror. The cavity mirror geometry consists of a flat mirror and a $f = 500$ mm concave mirror in $L = 77{,}5$ mm distance. It requires a Gaussian mode with focus size of 182.6 µm radius (1/e² level) at the flat mirror for ideal mode match. I took high care to align the beam focus to the distance of the first cavity mirror and to obtain a Gaussian beam mode of desired size.

Measuring the incoming, transmitted and reflected beam powers, I determine the mode matching coefficient of the beam to the cavity mode. The mode matching coefficient is calculated following [53,84]. I paid attention to account for the beam power in the EOM's modulation sidebands for the PDH lock, as only the power in the carrier at resonance frequency is relevant for the mode match. I verified this by taking the same measurement at very low EOM modulation depth such that no significant power was transferred to the sidebands.

The transmission coefficient $\mathcal{T}$ and reflection coefficient $\mathcal{R}$ are determined from the relative transmitted, respectively reflected beam power with the laser being locked to the cavity resonance. The measured values are shown in equation (3.13).

$$\begin{aligned} \mathcal{T} &= \frac{P_T}{P_{in}} = 17{,}3\ \% \pm 0{,}1\ \%\,; \\ \mathcal{R} &= \frac{P_R}{P_{in}} = 36{,}1\ \% \pm 0{,}1\ \%\,; \\ \mathcal{A} &= 1 - \mathcal{T} - \mathcal{R} = 46{,}6\ \% \pm 0{,}1\ \% \end{aligned} \tag{3.13}$$

P_T is the transmitted power, P_R is the reflected power and P_{in} is the total incoming power, always only at the carrier frequency.

The average per-roundtrip mirror transmission and loss coefficients (T, resp. A) and the cavity mode match ϵ are obtained from the following calculations.

$$\begin{aligned} \alpha &= \frac{P_T}{P_{in} - P_R} = \frac{\mathcal{T}}{1 - \mathcal{R}} = 0{,}271 \pm 0{,}002 \\ T &= \frac{2\alpha}{1+\alpha}\frac{\pi}{\mathcal{F}} = (6{,}17 \pm 0{,}04) \cdot 10^{-6} \\ A &= \frac{1-\alpha}{1+\alpha}\frac{\pi}{\mathcal{F}} = (8{,}32 \pm 0{,}04) \cdot 10^{-6} \\ \epsilon &= \frac{P_T}{P_{in}}\frac{(T+A)^2}{T^2} = (95{,}4 \pm 1{,}0)\ \% \end{aligned} \tag{3.14}$$

Repeating this measurement with varying modulation depths gave an average mode match coefficient of $\bar{\epsilon} = 95{,}4\ \% \pm 2{,}0\ \%$. This high mode match is an improvement by over 10% compared to the initial setup and satisfactory for our purpose.

Equation (3.13) shows that $\mathcal{A} \approx 47$ % of the incoming power in the carrier is absorbed by the cavity mirrors and coatings. The absorbed power heats the mirrors and cavity, causing thermal expansion and shifting the cavity's resonance frequency. This shows the necessity of an excellent intensity stabilisation of the laser beam at the cavity, otherwise laser power fluctuations result in variations of the resonance frequency. We regard the absorption of the transmission windows of the vacuum system as negligible. Those windows are anti-reflection coated and essentially transparent at 578 nm. Furthermore, the beam passes these windows only once in contrast to the many reflections on the cavity mirrors. I show sensitivity measurements of the cavity resonance frequency to beam power variations in this chapter's last subsection (p. 45).

The high mode match to the cavity reduces the off-reflected part of the carrier, which contributes to laser noise and an offset signal at the photodiode recording the PDH lock signal. Variations in this offset signal cause frequency instability of the laser in PDH lock.

CTE zero-crossing temperature and temperature sensitivity

Expressing temperature change-induced frequency changes as function of time
Relative changes in in cavity length are proportional to relative resonance frequency changes, as discussed in section 3.3.3. We can thus observe the thermal length expansion or contraction of the cavity by monitoring its resonance frequency. We monitor the frequency of our 578 nm laser locked to the cavity by beating it with a tooth of a frequency comb. We change the cavity temperature via the set point of the temperature controller, which acts via the Peltier element located at the outer cavity heat shield.

In our cavity setup, we do not directly measure the temperature of the cavity to avoid thermal or vibrational distortions transmitted by a sensor attached to the cavity. The closest temperature measure available is the in-loop signal of the cavity temperature regulation, acting on and measuring at the cavity heat shield. After setting a temperature via the temperature control, we typically wait several hours for the outer heat shield to thermalize and the regulation loop to settle. We model the cavity temperature, $T_{cav}(t)$, to exponentially approach the temperature of the outer shield, T_{shield}, as shown in equation (3.15).

$$\begin{aligned} T_{cav}(t) &= (T_{cav}(t_0) - T_{shield}) \cdot \exp\left(-\frac{t}{\tau}\right) + T_{cav}(t_0) \\ &= \Delta T \cdot \exp\left(-\frac{t}{\tau}\right) + T_{cav}(t_0) \end{aligned} \tag{3.15}$$

Where T_{cav} is the cavity temperature, T_{shield} is the temperature of the outer heat shield, τ the effective exponential approach time, and t_0 the time of the temperature change. $T_{cav}(t_0)$ is the cavity temperature at the start of the temperature change.

To phenomenologically match the observed resonance frequency changes to a cavity expansion, the cavity's effective thermal expansion is described with a linear coefficient of thermal expansion α_{phen} around its zero-crossing temperature, shown in equation (3.16).

$$\alpha_{phen} = a \cdot (T_{cav}(t) - T_{CTE\ ZC}) \tag{3.16}$$

With the cavity's effective linear expansion coefficient a ($[a] = \mathrm{K}^{-2}$) and the temperature at zero expansion $T_{CTE\ ZC}$.

We obtain an expression for temperature induced frequency changes as function of time in equation (3.17) as follows: We use the phenomenological thermal expansion coefficient (equation (3.16)) in the differential thermal length expansion (equation (3.8)), relate the cavity length to its resonance frequency (equation (3.1)) and integrate the expression. Last, we insert the exponential-approach time evolution of the cavity temperature (equation (3.15)).

$$\begin{aligned}\Delta\nu(t) &= -\nu_0 \cdot \frac{a}{2} \cdot (T_{cav}(t) - T_{CTE\ ZC})^2 \\ &= -\nu_0 \cdot \frac{a}{2} \cdot \left(\Delta T \cdot \exp\left(-\frac{t}{\tau}\right) + T_{cav}(t_0) - T_{CTE\ ZC}\right)^2 \\ &= -\nu_0 \cdot \frac{a}{2} \cdot \left(\Delta T^2 \cdot \exp\left(-\frac{2t}{\tau}\right) + 2 \cdot \Delta T \cdot \exp\left(-\frac{t}{\tau}\right) \cdot \right. \\ &\qquad \left. (T_{cav}(t_0) - T_{CTE\ ZC}) + (T_{cav}(t_0) - T_{CTE\ ZC})^2\right)\end{aligned} \tag{3.17}$$

ν_0 is the initial cavity resoance frequency, ΔT the temperature change, $T_{cav}(t_0)$ is the cavity's initial temperature at starting time t_0.

Measurement conditions and fitting properties

Figure 11 shows the observed beat frequency changes over time for several temperature steps, also listed in Table 3.3. With fits to the individual temperature steps we obtain the final frequency and time constant for each step. However, we cannot reliably determine the material parameters (a and the CTE-ZC temperature) from these fits du to (experimental) uncertainties and interdependencies between the individual terms and parameters of equation (3.17). To avoid uncertain inputs in the fitting process and to enable a reliable fitting routine, we simplified equation (3.17) to a few independent, free fitting parameters, shown in equation (3.18), and used that expression to fit the measured data.

$$\nu(\mathrm{t}) = A \cdot \exp\left(-\frac{2 \cdot (t - t_0)}{\tau}\right) + B \cdot \exp\left(-\frac{(t - t_0)}{\tau}\right) + \nu_{offset} \tag{3.18}$$

Where A, B and ν_{offset} are taken as independent parameters (without physical meaning) for the fit.

The first frequency measurement during day 0-2 was taken after the cavity setup had thermalized for several days enclosed in a noise isolation box to reduce effects of temperature changes among other things. Due to the breakdown of the self-built temperature controller described in section 3.2.1, the first temperature step during day 2-3 could not be evaluated. The controller was exchanged to a commercial thermoelectric controller[30] which offers a simpler temperature adjustment and readout over a larger temperature range. The temperature stability

[30] Wavelength Electronics WTC3243

of the chip, taken from its data sheet, is 1 mK. Connecting the new controller with additional cabling introduced a reduced sensitivity of the temperature regulation loop not considered in the chip's temperature stability. Nevertheless, large integration times of the temperature controller average out small, temporary signal fluctuations introduced by external influences.

Frequency errors in individual frequency data points, as displayed in the inset of Figure 11, are of the order of 140 kHz. They primarily result from the width of the comb teeth which beat with the clock laser. The full width at 90% level of a Gaussian fit was taken as frequency error value. The beat was recorded on a spectrum analyser averaging each data point for about 60 seconds average out comb frequency fluctuations and to obtain a better signal-to-noise ratio against the background signal. The error in the temperature set point results from the error range of the thermistors' characteristic curve and from the resistance readout. The error in the final frequency accounts for variations in fit results when slightly varying the input data range or initial parameters. This is a result of having several free fitting parameters with strong interdependencies in equation (3.18).

Using a global fit of equation (3.17) to the set of all temperature shifts, and thereby finding global optimum fit values for the common parameters a, τ and $T_{cav}(t_0)$ might give improved fit results. However, for this to work the temperature ranges of the individual steps, as required in equation (3.17), need to be estimated well enough. It was not done here as the relevant parameters (time constant, CTE-ZC temperature, effective CTE) can be derived from the follow-up data analysis.

Observations in the measurement data

We observed **a linear drift of the beat frequency** after letting the cavity settle sufficiently long from a temperature shift. This drift observed in this measurement (at day 0, days 28-29 and days 40-43) is on the order of $1{,}2 \pm 0{,}1$ kHz/h, respectively $0{,}33 \pm 0{,}03$ Hz/s. As the drift varied, a subsequent subtraction from the measured values for the whole observation time is questionable. For large temperature shifts above several degrees the effect on the final frequency is minimal and vanishes within the uncertainty. For smaller temperature shifts, the drift was on the same order as the settling frequency excursion and thus limits the available observation time. We assume the drift results from the aging of the cavity. At time of the measurement, we could not exclude other undesired influences onto the measurement. Such influences could be environment temperature drifts acting on the cavity or its temperature regulation. A temperature log of the vacuum system is discussed below, see also Figure 14. A drift of the frequency comb was unlikely, regarding its GPS reference. The linear drift observed here against the frequency comb is compared with the cavity drift observed against the atoms' clock transition presented in chapter 4.1.

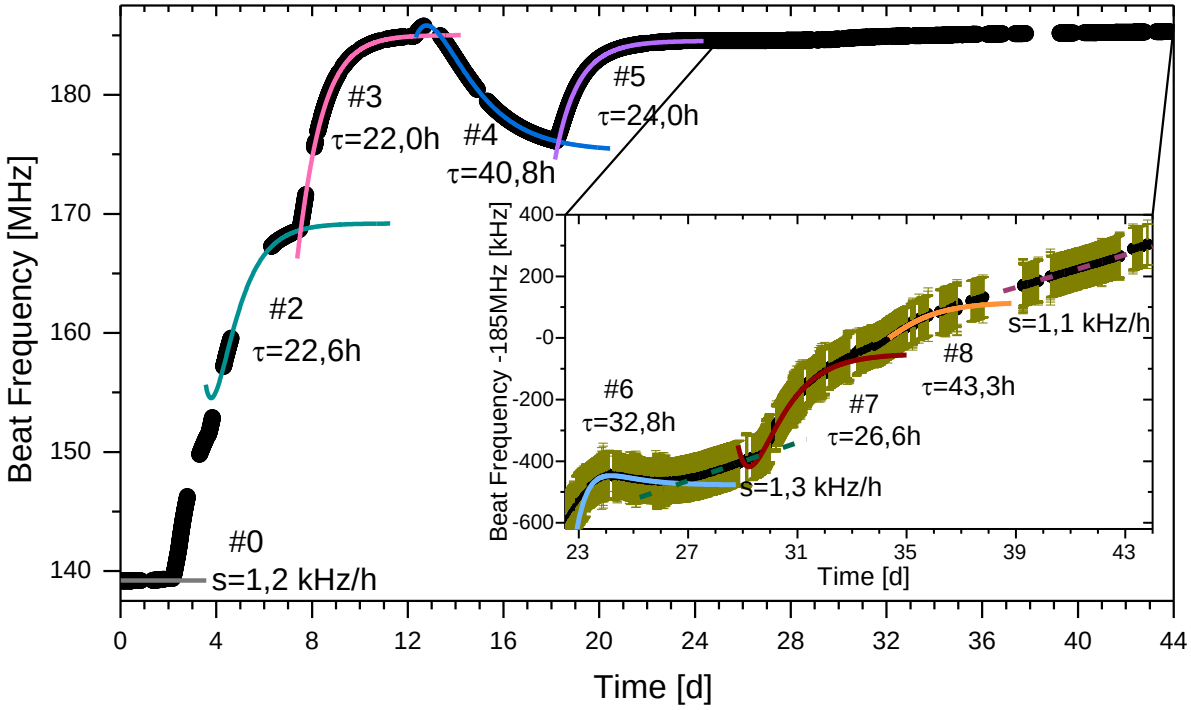

Figure 11: Beat frequency measurement of cavity resonance against a tooth of the frequency comb, recorded over time. Several changes of the temperature set-point were performed and a modelled frequency change (equation (3.18)) was fitted to these periods individually. The inset shows a magnification for the last three, small temperature steps around the CTE-ZC, resulting in sub-MHz changes of the resonance frequency. The inset shows frequency error bars of individual data points. Number labels of the temperature change and the corresponding exponential time constant, resp. linear slope are shown for each fit. Detailed discussion in the text.

Temperature shift #	**Time [days]**	**Temperature setting [°C]**	**Fitted final frequency [MHz]**	**Fitted time constant τ [h]**
0	0 - 2	20,3 ± 1,0	139,2 ± 0,3	-
1	2 - 4	failed due to controller breakdown		
2	4 - 7	25,0 ± 0,5	169,2 ± 0,3	22,6 ± 0,1
3	7,5-12	31,0 ± 0,2	185,0 ± 0,2	22,0 ± 0,1
4	12 - 18	38,0 ± 0,3	175,3 ± 0,2	40,7 ± 0,2
5	18 - 22	32,3 ± 0,2	184,5 ± 0,2	24,0 ± 0,8
6	23 - 26	31,0 ± 0,2	184,5 ± 0,2	w/o dc: 24,5 ± 0,2 with dc: 32,5 ± 0,1
7	29 - 32	31,7 ± 0,2	185,0 ± 0,1	w/o dc: 26,6 ± 0,2 with dc: 19,8 ± 0,1
8	34 - 36	32,0 ± 0,2	185,1 ± 0,2	w/o dc: 29,1 ± 0,2 with dc: 18,9 ± 0,1

Table 3.3: Temperature setting of the cavity outer heat shield, as well as the final cavity frequency and the time constant obtained from fitting an exponential temperature approach to a linear thermal expansion model of the cavity resonance frequency (equation (3.18)) to individual temperature changes. For small temperature shifts #6-#8, the fitted time constant is shown for fits without and with drift compensation (dc).

The **exponential approach time τ** of the cavity resonance frequency to adapt to a temperature change at the outer heat shield ranges from 19 h to 41 h. A slight variation in exponential approach time could be attributed to influences of the environment temperature onto the vacuum system. We do not understand the reason for the large deviation of the exponential approach times, especially for the temperature step #4 going from 31 °C to 38 °C with $\tau = 40{,}7 \pm 0{,}2$ h. Subsequently subtracting the linear drift observed in temporal proximity for the small temperature steps influences the fit results of the exponential approach times. When going away from the CTE-ZC temperature, as in temperature shift #6, the observed frequency decrease is amplified by subtracting a positive linear slope from the data. The fitted approach time then increases from $\tau_{ts\#6,no\_dc} = 24{,}5$ h to $\tau_{ts\#6,dc} = 32{,}5$ h with drift compensation (dc). Vice versa, for temperature steps which approach the CTE-ZC as in temperature shift #7, the fitted $\tau_{ts\#7}$ decreases from 26,6 h without dc to 19,8 h with dc. In temperature shift #8, which further approaches the CTE-ZC temperature, $\tau_{ts\#8}$ decreases from 29,1 h without dc to 18,9 h with drift compensation. As we did not understand the reason for the large variations in decay time, we did not exclude individual temperature shifts based on this parameter in our cavity analysis.

Another observation is a **shift of the beat frequency's absolute value** measured for the same temperature setting but at separate times. This effect hindered approaching the cavity's ideal CTE-ZC temperature for the cavity, as the absolute frequency value did not serve as orientation. Figure 11, Figure 12 and Table 3.3 help following the discussion below:

One comparison of absolute frequencies is when passing the CTE-ZC temperature. First, the CTE-ZC was passed during temperature step #4 (shifting from 31 °C to 38 °C) at time 12,8 days with maximum beat frequency 185,8 ± 0,1 MHz. During temperature shift #6, the cavity's CTE-ZC was passed at time 24,0 days with a peak frequency of 184,6 ± 0,1 MHz. This is an offset of the maximum frequency value of -1,3 ± 0,1 MHz after 11,2 days. When adding a linear drift compensation (which removes a steady frequency increase over time), the frequency difference increases to -1,6 ± 0,2 MHz.
To get another absolute frequency comparison, we wanted to reproduce the result of temperature shift #3 with the next temperature shift, #6. The outer heat shield temperature was set to 31,0 °C in both measurements. The difference of the final fit frequencies between these measurements is -0,5 ± 0,3 MHz, resp. -1,0 ± 0,1 MHz after drift compensation.
Due to the positive linear drift, the initial absolute maximum value of 185,8 MHz was surpassed in the following days. We did not observe another (absolute) frequency maximum in the course, which would have indicated a crossing of the CTE-ZC temperature.
These frequency differences exceed the difference resulting from the temperature uncertainty range (obtained using the parabola fit results discussed below). They are therefore not expected by our (experimental) error estimation.
We could not observe the cavity behaviour (drifting and absolute frequency) longer due to limited time in our experiment schedule. Especially the further behaviour of the linear drift could have indicated if a slow settlement process was acting here, as it approached the initially observed maximum frequency with time.

Compared to large frequency shifts over tens of MHz in previous temperature shifts several degrees away from the cavity's CTE-ZC temperature, the frequency difference observed here is small. In [78], a more pronounced shift of the cavity's resonance frequency at same temperatures was attributed to a settlement of a bad optical contact of one resonator mirror. Other experiments, such as [62,67], also show (slight) deviations in the measurement data to the parabola describing the cavity resonance shift, especially around the CTE-ZC temperature. We decided to approach the cavity CTE-ZC temperature with the following temperature shifts as good as possible to obtain a thermalized cavity and clock laser system ready for experiments.

Determining the Cavity CTE-ZC and the cavity's temperature sensitivity

Figure 12 and Table 3.3 show the fitted final beat frequencies (obtained from fits using equation (3.18)) over the respective temperatures of the outer cavity heat shield. A parabolic fit curve models a linear coefficient of thermal expansion for the cavity, as shown in equation (3.17). The fit gives the coefficient of thermal expansion zero-crossing at $T_{CTE-ZC,all} = 32{,}32 \pm 0{,}09$ °C. Excluding the last three, small temperature shifts for the parabola fit would change the zero-crossing temperature only minimally to $T_{CTE-ZC,TS\#0-5} = 32{,}31 \pm 0{,}16$ °C. Including all temperature shifts in the parabola fit, the parabola describes the temperature dependence of the cavity's resonance frequency (equation (3.17)) with

$$\frac{\Delta\nu(T)}{\nu_0} = -6 \cdot 10^{-10} \cdot (T_{cav}(t) - T_{CTE-ZC})^2 \ \mathrm{K}^{-2} \tag{3.19}$$

The effective linear thermal expansion coefficient of the cavity ULE material results to be $a_{cav1} = 1{,}19 \pm 0{,}03$ ppb/K^2. This is very low and the resulting CTE $\alpha_{cav1} = a_{cav1} \cdot (T - T_{CTE-ZC})$ (equation (3.16)) lies well within the specifications for ULE glass, which is specified to be within the range of $\alpha_{ULE} = 0 \pm 30$ ppb/K for temperatures from 5 °C to 35 °C [75].

Figure 13 shows the sensitivity of the cavity resonance frequency to temperature changes over the temperature difference to the CTE-ZC temperature. The temperature controller was set to $\mathrm{T} = 32{,}0 \pm 0{,}2$ °C for the spectroscopy measurements presented in this thesis. This corresponds to a temperature sensitivity of the cavity's resonance frequency in the range of $\partial\nu/\partial T_{new} = 93 \pm 62$ Hz/mK. This is a significant improvement compared to the previous cavity operating with a sensitivity of $\partial\nu/\partial T_{old} = -35$ kHz/mK. The sensitivity of the new cavity is similarly large as obtained for the modelled cavity at 0,1 °C temperature difference to its CTE-ZC.

Tuning the set temperature of the cavity even closer to its zero-crossing temperature is desirable and was only omitted due to time constraints (regarding the cavity requiring about 3 days to settle) before starting spectroscopy measurements and uncertainty about the origin of the linear drift and frequency offset observed while conducting the measurements.

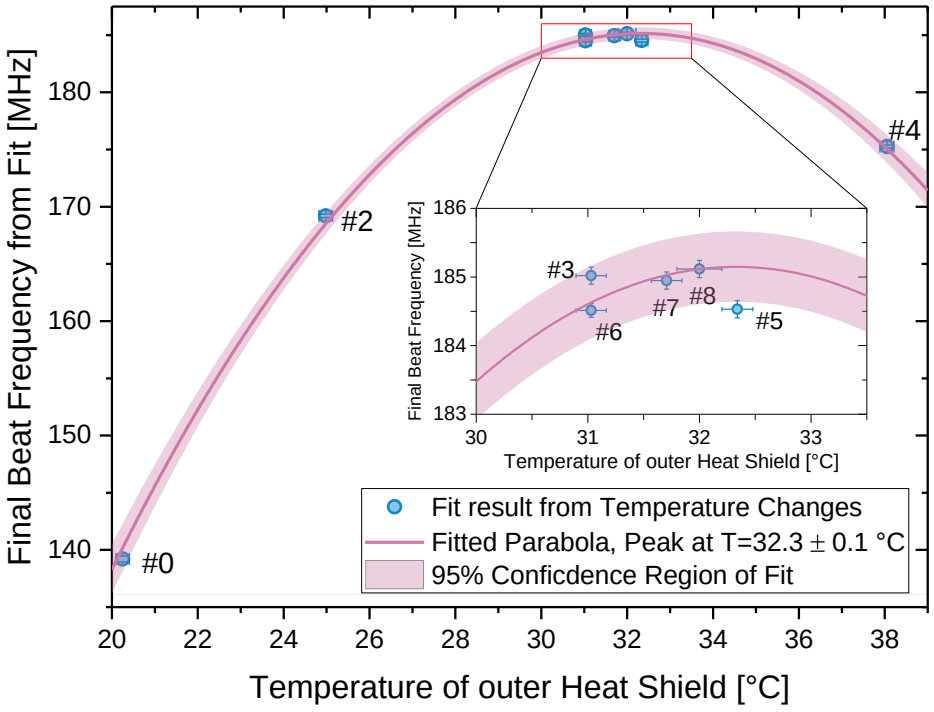

Figure 12: Cavity resonance frequency over set temperature of the outer heat shield. The data points show the final frequencies obtained from fits to measured curves of the resonance frequency after changing the temperature of the outer heat shield. Number labels show the order of temperature steps recorded. Frequency curves and individual fits are shown in Figure 11. The cavity's CTE-ZC temperature is obtained by fitting a linear CTE model resulting in a quadratic temperature dependence to the data points, giving $T_{CTE\text{-}ZC} = 32{,}3 \pm 0{,}1$ °C. The inset shows pronouncedly a shift in absolute resonance frequency when measuring similar set temperatures at separate times. Error estimates are discussed in the text.

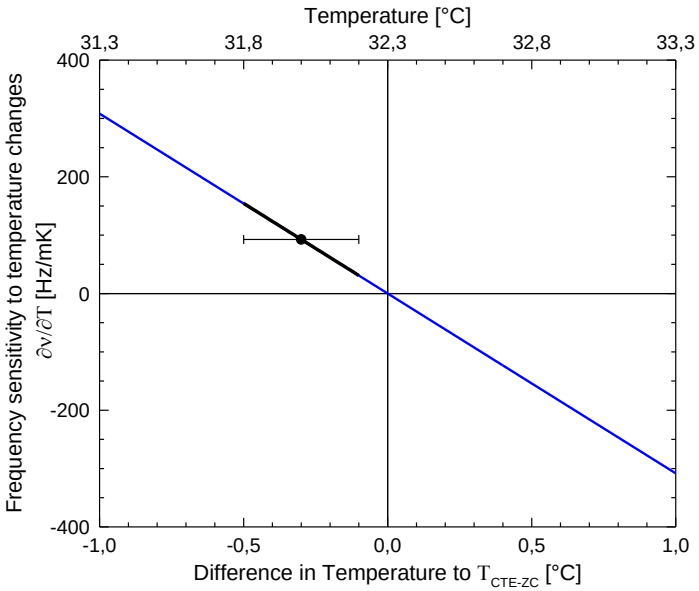

Figure 13: Temperature sensitivity of the cavity resonance frequency close to the cavity's CTE-ZC temperature. The data point and error bar indicate the operating temperature of the cavity and its uncertainty for the spectroscopy measurements performed, $T_{cav} = 32{,}0 \pm 0{,}2$ °C. The corresponding sensitivity is $\partial\nu/\partial T = 93 \pm 62$ Hz/mK. Absolute temperature values are shown in the top axis.

Temperature log of the outer vacuum chamber

We could not directly measure the temperature of the cavity or its heat shields out of the regulation loop. We mounted a thermistor at the outer side of the vacuum chamber to record the temperature of the vacuum chamber. The temperature measurement includes actions of the Peltier element attached to the inside of the chamber. It also includes influences the environment temperature of the overall setup, which was in a closed wooden box placed under a temperature stabilizing flow box. Figure 14 shows the measured temperature during a spectroscopy measurement period. Temperature fluctuations on the order of 30-100 mK occurred over 12-24 hours, roughly following the work times in the lab. This system's temperature stability of about 0,1 K over one day is a very good working condition for the temperature regulation of the outer heat shield. An estimation of the temperature isolation of the cavity done by Thomas Rützel [72] concluded that the Peltier element of the temperature controller dominates the temperature influence onto the cavity.

The data sheet for the temperature controller acting onto the outer heat shield gives a stability of 1 mK for the chip. However, we can assume that the effective stability of the whole temperature regulation loop is worse. The temperature stabilized outer heat shield and the cavity in the inner heat shield can be assumed to be at least one order better than that of the outside environment. We assume the temperature stability of the cavity in the current system to be a few millikelvin, following the small changes of the outer heat shield with the measured time constant of $\tau \approx 20$ h. This will be compared with the residuals after linear drift subtraction in the atom spectroscopy measurements presented in chapter 3.7.2.

A comparison to the results of the FEM analysis in chapter 3.3.3, especially the structural constant δ, is not possible as the precise ULE material parameters of the mirrors and spacer are not known, leaving too many open parameters.

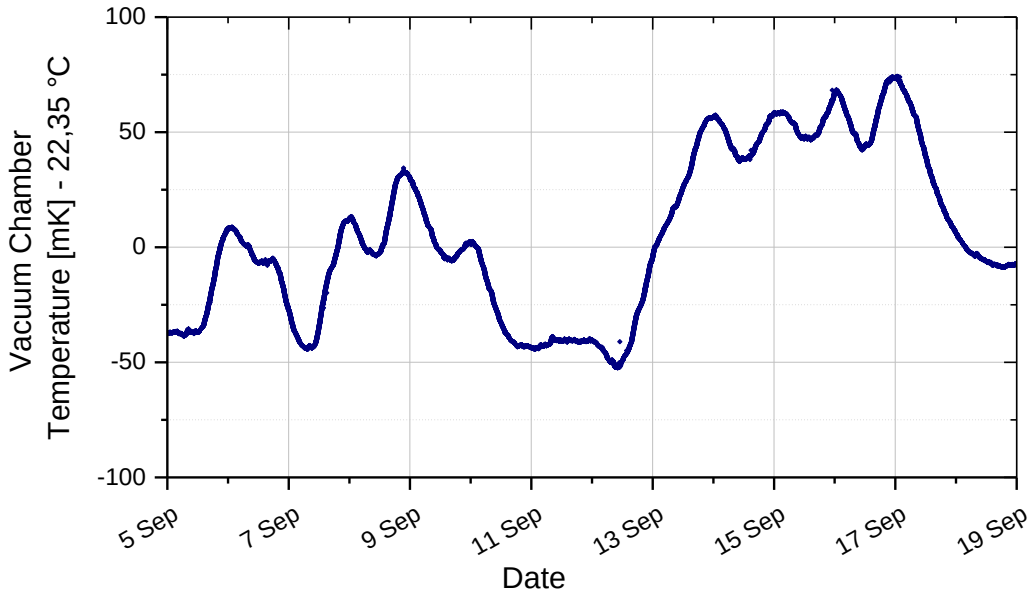

Figure 14: Temperature of the vacuum chamber, measured at the lower bottom side, during a spectroscopy measurement period. The measured temperature is influenced by actions of the Peltier element and by the overall temperature of the setup inside a wooden box. We observe temperature excursions on the order of 30-100 mK over 12-24 hours. The spectroscopy measurements determining the cavity resonance frequency drift over time in Figure 29 start at 9 pm on 7th of September.

Resonance Frequency Sensitivity to Intracavity Power

Along with the mode match, I evaluated that about 46% of the resonant light power impinging onto the cavity is absorbed, predominantly by the cavity mirror material and coatings. The power deposited in the cavity results in a deformation which changes the cavity resonance frequency. Especially the thin mirror coatings have a low heat capacity and a high linear CTE, estimated to correspond to a temperature sensitivity of $20\ \mathrm{Hz/mK}$ [64]. Fluctuations in the light power coupled into the cavity thus result in near-instantaneous fluctuations of the cavity resonance frequency. To minimize such unwanted fluctuations, we stabilize the light power in the cavity by an intensity regulation to the transmitted intensity. I measured the sensitivity of the cavity resonance frequency to intensity fluctuations which allows me to estimate the required intensity stability.

To quantify the power sensitivity of cavity 1, I modulated the incoming light power and observed the change of the cavity resonance frequency in a beat note with the undisturbed laser branch which was independently locked to the cavity 2 (setup details are given in chapter 3.7.1). The modulation was done via the set value of the intensity control loop acting via the driving power of an AOM on the path to the cavity. The modulation function was a square function switching between 100% and 72% of the standard operating power. This large relative modulation amplitude was necessary to clearly observe a shift in the beat frequency induced by the intensity modulation against drifts and other fluctuations. I recorded the beat frequency with a spectrum analyser, paying attention to a sufficiently fast time resolution with sweep times between $0{,}2\ \mathrm{s}$ and $0{,}6\ \mathrm{s}$ for resolution bandwidths of $10\ \mathrm{Hz}$ down to $3\ \mathrm{Hz}$.

Figure 15 exemplarily shows the beat frequency changing by about $12{,}9 \pm 3{,}5\ \mathrm{Hz}$ at an intensity modulation frequency of $0{,}1\ \mathrm{Hz}$ and a modulation amplitude of $\Delta P = 261 \pm 3\ \mathrm{nW}$ transmitted power. I observed near-instantaneous changes in beat frequency, faster than the temporal resolution of the spectrum analyser. I did not observe a thermalization process in the beat frequency change. Figure 16 shows the power sensitivity of the resonance frequency (in Hz over µW of transmitted power) for modulation frequencies from 0,1 Hz to 2,0 Hz. A specific responsivity to certain frequencies does not turn out in that range. Faster modulations could not be recorded due to low signal quality and limited sweep time of the analyser. The observed average frequency sensitivity to power modulation of the all ULE cavity in the PDH system is $46{,}0 \pm 10{,}1\ \mathrm{Hz/\mu W_{tr}}$ with respect to the power transmitted through the cavity.

The large intensity modulation also affected the bandwidth and offset of the PDH lock. The PID settings were optimized to the high-power setting. When switching to lower power, the regulation bandwidth of the PDH lock reduced from about 1,0 MHz to 0,9 MHz with less aggressive servo bumps and the overall spectrum of the PDH photodiode around the modulation frequency being 5-10 dB lower. Monitoring the offset, I evaluated the effect of intensity modulation at the PDH photodiode onto the PDH offset voltage to be $86 \pm 20\ \mathrm{\mu V/\mu W_{PDH\,PD}}$ (with $\mathrm{\mu W_{PDH\,PD}}$ relating to the power on the PDH photodiode) which corresponds to $600 \pm 140\ \mathrm{\mu V/\mu W_{tr}}$ relating to the power transmitted through the cavity. The large relative error results from large fluctuations of the PDH offset independent from intensity modulation compared to the steps caused by intensity modulation.

The error signal slope on resonance is 107 ± 26 µV/Hz for cavity 1. To quantify the error signal slope, I monitored changes of the beat frequency of the laser while modulating the cavity 1 PDH error signal offset voltage around the setting for minimal PDH error signal offset. This measurement is elaborated in section 3.4.2.

We can combine these results to isolate the power sensitivity of the cavity itself. The effect of the intensity modulation on the PDH offset corresponds to a frequency change of $5{,}6 \pm 1{,}9$ Hz/µW$_{tr}$. This reduces the power sensitivity of the cavity itself to $40{,}4 \pm 10{,}3$ Hz/µW$_{tr}$. For technical reasons, I could only statistically evaluate subsequent measurements of PDH offset and beat frequency change during intensity modulation. Evaluating the PDH offsets (ideally of both cavity locks) simultaneously recorded with the beat frequency will likely reduce uncertainties in the results.

The power sensitivity of the all-ULE cavity is significantly lower than that of the cavities with FS mirror substrates operating far away from the resonance frequency. The sensitivities of the latter were $3{,}45 \pm 0{,}38$ kHz/µW$_{tr}$ for cavity 1 and 620 ± 30 Hz/µW$_{tr}$ for cavity 2, showing a thermalization with exponential time constant of 1,5 s [53,58]. Sensitivities between 10 ± 2 Hz/µW [80] and 65 Hz/µW [63] were reported by other groups for this vertical mounted cavity geometry. The new cavity fits very well into this range.

Knowing the power sensitivity of the cavity in the PDH system, we can estimate a stability requirement for the intensity controller. We assume a high value for the system's power sensitivity of 55 Hz/µW$_{tr}$ and demand a laser stability below the 1 Hz level, which corresponds to a relative stability of 10^{-15} at the laser frequency of $\nu_{clock} = 518{,}2946$ THz. This requires the transmitted intensity to be stable to 9 nW. The recorded transmitted power is 945 ± 2 nW, the fluctuations (standard deviation) indicating a relative intensity stability of $2 \cdot 10^{-3}$, surpassing the required intensity stability of $1 \cdot 10^{-2}$. Furthermore, taking peak fluctuations of the transmission intensity of $5 - 10$ nW and the power sensitivity of 56 Hz/µW, the intensity fluctuations correspond to frequency fluctuations of $0{,}3 - 0{,}6$ Hz in a large estimate. Thus, the intensity stabilisation control loop meets the required overall intensity stability for a sub-Hz laser linewidth for this PDH system very well. The intensity regulation is further discussed in chapter 3.5.

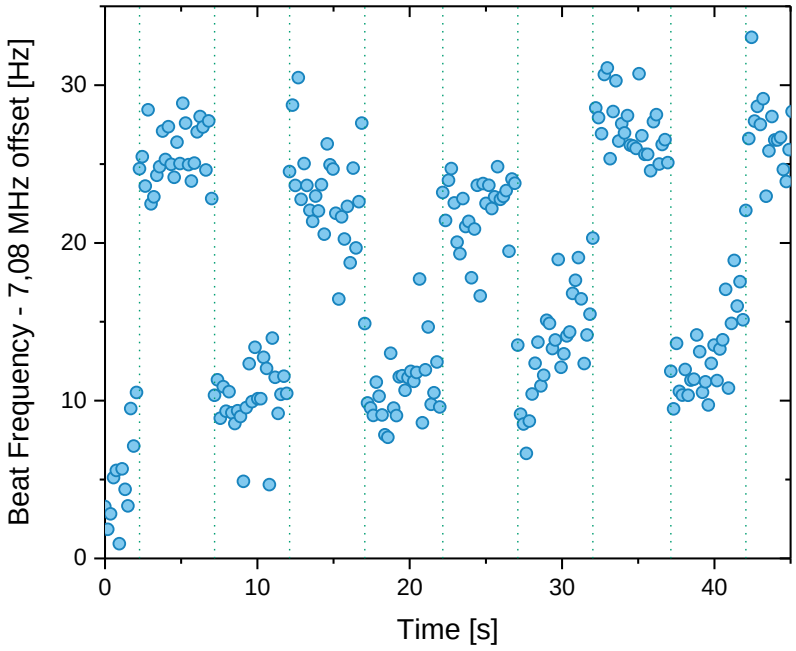

Figure 15: Beat frequency change at beam intensity modulation. Excerpt of the beat frequency of the two laser branches, independently locked to the two cavities, recorded over time, while the light power to cavity 1 was modulated by 38%, corresponding to a transmitted power difference of $\Delta P = 261 \pm 3$ nW, at a frequency of 0,1 Hz (vertical dotted lines indicate half-periods). The observed frequency shift of this measurement is $\Delta f = 12{,}9 \pm 3{,}5$ Hz, giving a sensitivity of $49{,}4 \pm 13{,}6$ Hz/µW. The excerpt shows fluctuations of the beat frequency of $\Delta f_{fluct} = 3{,}3$ Hz relative to the respective mean level.

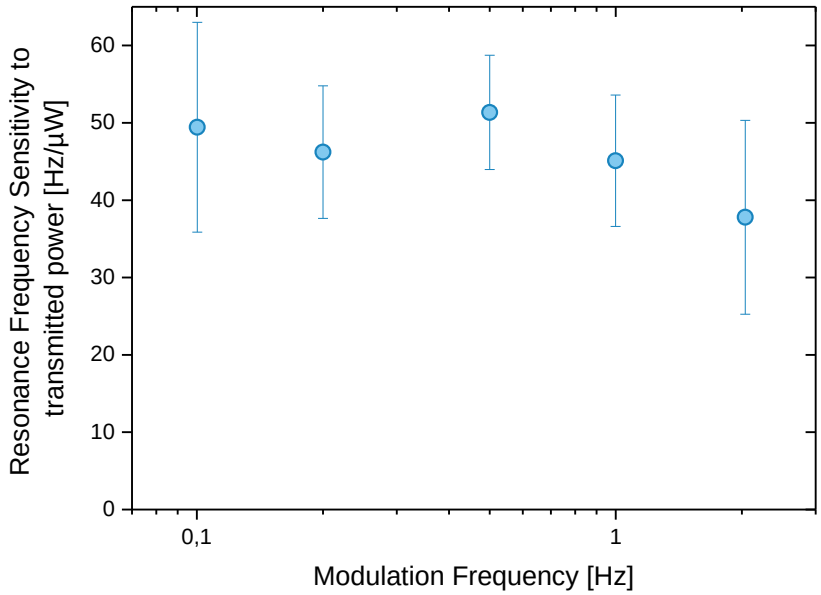

Figure 16: Sensitivity of the cavity resonance frequency to power fluctuations over modulation frequency. The blue dot data points were determined via a modulation of 28% reduction from the maximum light power, corresponding to $\Delta P = 261 \pm 3$ nW. Error bars indicate the standard deviation for the respective set of observed steps. The average frequency sensitivity to power fluctuations of the all-ULE cavity is $46{,}0 \pm 10{,}1$ Hz/µW with respect to the power transmitted through the cavity.

3.4 Fibre EOM and PDH lock

3.4.1 Advantages of using a fibre EOM and EOM characterization

The initial PDH setup contained a free space, bulk crystal EOM. The modulation signal at $f_{PDH} = 17.8$ MHz was provided by a function generator, amplified by an RF amplifier and a succeeding impedance matching resonant circuit. The free space EOM required a high modulation voltage of 200 V for a phase shift of $\lambda/10$, corresponding to a modulation depth $\beta = \pi/5 \approx 0{,}63$. The initial setup achieved a modulation depth of $\beta \approx 0{,}48$, resulting in only 65% of the error signal slope compared to operation at optimal modulation depth of $\beta_{opt} = 1{,}08$ [66].

The waveguide-based EOM[24] used in the new setup has several advantages to a bulk crystal EOM. The $LiNbO_3$ birefringent crystal embedded in the surrounding substrate has a cross section diameter of only a few micrometres. This enables a low modulation voltage of only a few volts for a phase shift of π for light polarized along the extraordinary crystal axis and the electric field applied along the same axis. Together with a fast electro-optic response, this enables modulation frequencies up to several gigahertz [85,86].

The low modulation voltage allows the additional tuning of the crystal by applying a DC electric field on top of the RF signal. The DC field adds an offset to the RF signal, enabling to tune the characteristic curve of the modulator, respectively rotate the alignment of the crystal axes. This enables to maintain an optimal matching of the crystal alignment to the linear polarization of the light by remote tuning. Deviations from an initial alignment may result from temperature changes and other environmental changes over time. A varying mismatch of the light polarization to the crystal axes takes effect as a cross-coupling of the phase modulations of the two crystal axes, changing the beam polarization and causing unequal frequency modulation sidebands in the light exiting the EOM. A varying output polarization in combination with unavoidable polarization selective elements downstream in the setup results in undesired light power modulation. The other effect resulting from unequal modulation sidebands is residual amplitude modulation (RAM) noise, which is harder to compensate against. RAM especially effects the quality of error signals of frequency-modulation-based locking techniques, such as the PDH lock used in this setup. Being able to control the temperature of the EOM and the DC electric field across the crystal allow to stabilize the light and modulation against changes in the environment and therefore enable control against RAM [87–90].

An important detail of the waveguide-based EOM used is that only light polarized along the extraordinary axis of the crystal is wave-guided by internal reflection. Light polarized along the ordinary axes is scattered into the surrounding substrate and thus lost. This inhibits a major source of RAM but also creates a problem for the regulation of remaining RAM noise. RAM noise and the monitoring solution in our setup are discussed in chapter 3.6.1.

Furthermore, stress in the fibre, especially at the interface to the waveguide, degrades the linear polarization of the light. This results in an effective polarization extinction ratio of 2000:1 at the output fibre of the EOM, as stated in the data sheet. We placed a Glan-Taylor polarizer with extinction ratio of 100 000:1 after the EOM to ensure a clean and well-defined polarization.

The small dimensions of the EOM with connectors make a temperature stabilisation well realizable. We mounted the EOM on a small copper block which was temperature controlled[31] via a foil heater with integrated thermistor[32]. To be able to apply DC voltages to the crystal, the EOM was electrically isolated from ground, as recommended by the manufacturer [85]. Furthermore, we placed the EOM in an aluminium box to isolate it from RF noise in the laboratory.

In a test setup, I characterized the EOM's modulation efficiency. I measured a beat signal between the beam passing the EOM and a reference beam while varying the power of the modulation signal. The EOM modulation frequency was $\omega_0 = 16$ MHz in this measurement and the reference beam frequency was shifted by $\Delta f = 0{,}9$ MHz to the beam passing the EOM. A spectrum analyser processed the beat signal, giving the signal powers of the carrier at frequency Δf and of the first sidebands at $\omega_0 \pm \Delta f$. Figure 17 shows the signal powers as function of modulation voltage with fits of scaled, squared Bessel functions of 0th, respectively 1st order, as shown in equation (3.20).

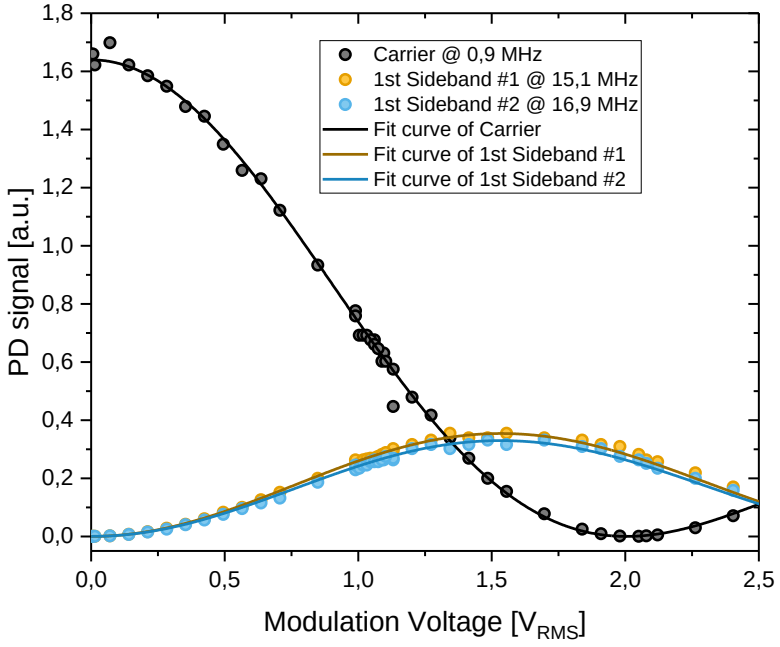

Figure 17: Characterization curve of EOM modulation efficiency. The signal powers of the carrier and the sidebands are plotted as a function of the RMS modulation voltage applied to the EOM. For this measurement, the beat of the beam passing the EOM, running at modulation frequency $\omega_0 = 16.0$ MHz, with a reference beam, shifted by $\Delta f = 0{,}9$ MHz, was analysed on a spectrum analyser. Fit curves of scaled, squared Bessel functions of 0th, resp. 1st order and with common horizontal scaling factor are shown. The obtained modulation efficiency of the EOM is $b = 1{,}200 \pm 0{,}003$ rad/V_{RMS}.

[31] Wavelength Electronics WTC3243

[32] Thorlabs HT10K

$$P_i(V_{RMS}) = a_i \cdot J_\alpha(b \cdot V_{RMS})^2 \quad (3.20)$$

V_{RMS} is the applied modulation voltage, a_i are individual fitting amplitudes, J_α is the Bessel function of order α (0^{th} and 1^{st} order in this measurement) and b is the modulation efficiency of the EOM ($(b \cdot V_{RMS})$ is the modulation depth). A global fit with common modulation efficiency for the three curves gave $b = 1{,}200 \pm 0{,}003\ \mathrm{rad/V_{RMS}}$. The fit amplitudes of the two sidebands differed by 7%, with the first sideband at lower frequency persistently having the larger amplitude than that at higher frequency. The reason for that difference is unknown.

The low modulation voltage, a simple RF isolation and a simple temperature stabilisation make the waveguide-based fibre EOM a good working device for our PDH lock. A downside could be the increased sensitivity of the light frequency to external vibrations when passing the additional optical fibres. We fixed the EOM's fibres to the breadboard on the vibration isolation platform located in a wooden box, ideally minimizing external perturbations. Frequency and phase noise from fibre links and more extensively from the whole optical path to the cavity could be compensated by an elaborate fibre noise cancellation scheme, which will be discussed along other potential, future improvements in chapter 3.8.

3.4.2 Pound-Drever-Hall lock characteristics

With the laser, cavity and EOM, the crucial components to realize a Pound-Drever-Hall lock are in place. After the brief description of the PDH locking technique in chapter 3.1, I now present an experimental characterisation of the PDH lock realized in the clock 1 setup.

We operate at a modulation frequency of $\omega_0 = 17.8$ MHz. This is about 2000 times the cavity linewidth and 9 ‰ of a free spectral range. Therefore we work in the fast PDH modulation regime [66].

PDH error signal

Figure 18 shows the qualitative PDH error signal and the corresponding transmission signal when scanning the frequency of the unlocked laser over a cavity resonance. To recover the error signal from a significant noise background, a moving average filter was applied by the oscilloscope to the recorded signal. The recorded error signal qualitatively recreates the expected course, with poles occurring when the carrier and sidebands cross the cavity resonance. The magnitudes of the error signal in positive and negative direction are expected to be equal. This deviation in the recorded signal is assumed to result from the scanning direction in combination with the high noise level in the unfiltered error signal and thus the required averaging process.

The scanning speed via the laser's master oscillator piezo was about -870 MHz/s, which was necessary to avoid laser frequency fluctuations in the ≈ 100 kHz wide laser linewidth while passing a cavity resonance. However, at this high scanning speed a proper build-up of the intracavity field is not possible as the laser passes the cavity resonance of 9 kHz FWHM in about 10 µs, which is faster than the cavity time constant of $\tau = 17{,}9\ \mu s$. Nevertheless, the transmission signal, simultaneously recorded and processed with a moving average filter,

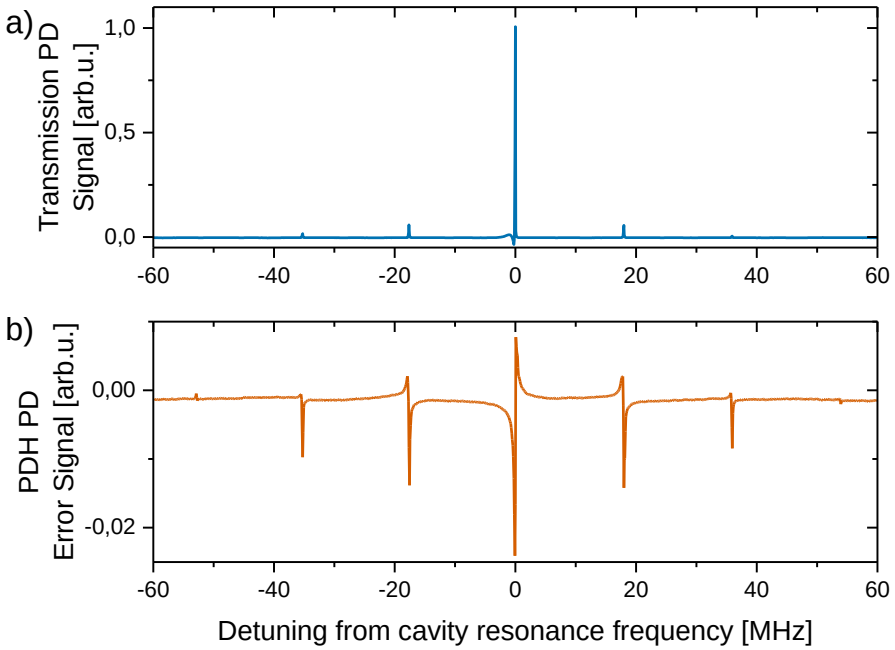

Figure 18: Qualitative transmission and PDH error signals recorded when scanning the unlocked clock laser over the cavity resonance. The carrier and up to second sidebands are visible in the transmission signal (top). The PDH error signal (bottom) qualitatively matches the theoretical error signal curve. The unequal magnitude of the signal in positive and negative direction is assumed to be an artefact resulting from the scanning direction (coming from above the resonance frequency) and the signal processing (moving average) of the oscilloscope. Similarly, the spike to negative values in the transmission signal when the carrier is on resonance is not expected but assumed to be an artefact of the photodiode or oscilloscope.

qualitatively shows the carrier and sidebands coupling into the cavity in accordance with the error signal resonances.

For detailed, quantitative information on the error signal, one would scan the cavity resonance more precisely. However, the unlocked laser did not provide a sufficiently stable, narrow frequency spectrum. Providing an independently locked, stable, and narrow frequency in front of cavity 1 is not well feasible in the current setup. Attempts to lock the laser to cavity 2 by current modulation did not establish a stable lock due to an insufficiently fast current-frequency modulation behaviour of the 1156 nm laser diode (a detailed evaluation of the diode's frequency response is given in [53]). Locking the laser with fast and slow feedback to the second cavity did not provide a sufficiently narrow beam at cavity 1 as the branches to the two cavities are essentially independent from one another. An idea not tested is to simply forward the fast correction signal of the cavity 2 PDH lock to the fast AOM of cavity 1. This will likely achieve a sufficiently narrow, stable signal to scan the cavity resonance, despite adding compensated noise of the cavity 2 regulation path to the beam at cavity 1.

Nevertheless, I could measure the PDH error signal slope, i.e. the error signal voltage over frequency, at resonance. Adding a modulation to the PDH error signal voltage at the PID input and observing changes in the beat frequency of the two cavities gives the error signal slope around resonance. The obtained error signal slope on resonance is 107 ± 26 µV/Hz. The PDH error signal voltage was modulated with a square function applied at the differential input of

the PDH PID controller. The modulation amplitude was up to a few millivolts around the optimum setting at which the PDH error signal offset turns minimal. Fluctuations of the beat frequency on each level being large with respect to the frequency shift induced by the offset voltage modulation caused the large relative error of the result.

This error signal slope is about five times larger than that of the initial system with free space EOM and a cavity with broader resonance [53], compared to the new setup with fibre EOM at optimum modulation depth and a cavity with a ¼ narrower linewidth.

Lock regulation bandwidth

We monitor the signal of the PDH photodiode outcoupled to a spectrum analyser before it is mixed with the local oscillator signal. Figure 19 shows the recorded PDH photodiode power spectral density around modulation frequency $\omega_0 = 17{,}8\,\mathrm{MHz}$ with the laser locked to the cavity. The signal at the modulation frequency corresponds to the PDH error signal. First regulation loop resonances ("servo bumps") appear at $\pm\,1{,}1\,\mathrm{MHz}$ distance from ω_0 and indicate a similarly large regulation bandwidth. The signal at modulation frequency being above background level indicates a frequency offset of the laser to the cavity resonance frequency which did not vanish over 1 s averaging time. I discuss variations of this signal (i.e. the PDH error signal) over time in the next section. We adjusted the overall gain and PID parameters of the PDH lock to minimize noise around the carrier and obtain a large regulation bandwidth with the overall feedback staying well below regulation loop oscillations.

A Bode plot and noise density analysis of the PDH error signal for the initial PDH setup is given in the thesis of Alexander Thobe [53], showing a regulation noise density enabling a 1 Hz linewidth. As the capability of hertz-level linewidth has been shown for that initial setup and as the laser, detection photodiode and regulation electronics remained the same in the new setup, we did not expect different results and relied on the already existing noise analysis.

The electronic PDH lock is highly stable against external perturbations, with the laser lock rarely failing. However, when observing the beat of the two laser branches locked to their respective cavities, slight air currents or pressure fluctuations in the lab caused significant fluctuations in the beat frequency and distortions of the laser stability, discussed in chapter 3.7.1.

Monitoring the PDH photodiode signal at modulation frequency

When enabling an "unlimited integrator" of the PDH lock (giving a slow feedback to the master oscillator laser piezo), we fine tune the PDH input signal voltage set point at the PID regulator to minimize the carrier amplitude at modulation frequency ω_0, ideally for it to vanish to the low, noise-suppressed level of the PDH locked laser. It is not always possible to achieve a good suppression of the carrier amplitude, as can be seen in Figure 19. Furthermore, we observe long excursions from the initial minimal carrier signal amplitude over time, in addition to fast fluctuations. We interpret the carrier at modulation frequency ω_0 as a combination of an (electronic) signal offset and the signal corresponding to the PDH error signal, indicating frequency excursions of the laser around cavity resonance. Ideally, we would expect this signal

to fluctuate around a constant, minimal offset voltage value. We could not isolate the cause of the long-term excursions of the carrier amplitude.

Figure 20 exemplarily shows such fluctuations of the electronic carrier amplitude of the PDH photodiode signal (effectively the PDH error signal) over time while the laser is locked to the cavity. The signal was recorded with the spectrum analyser in zero-span mode. The spectrum analyser resolution bandwidth captured the carrier peak while still being fast enough to record fast fluctuations. The signal in the resolution bandwidth is dominated by the carrier peak, the contribution of the highly suppressed noise floor around the carrier peak is insignificantly small. The excursions of the carrier amplitude are over 0,6 mV over 30 s from a minimal average voltage and with 0,14 mV standard deviation. Variations of the PDH error signal can be converted into frequency deviations from the cavity resonance via the error signal central slope of 107 µV/Hz and after subtracting an averaged signal offset around which the error signal voltage was minimal. The corresponding frequency excursions are about 5 Hz (over 30 s) with standard deviation of 1,3 Hz. A similar measurement showed excursions below 0,4 mV (corresponding to 3 Hz) with a standard deviation of 0,06 mV (0,6 Hz), indicating variations in the PDH error signal offset and in the regulation stability at separate times.

In a subsequent measurement, I recorded the beat frequency of the two undisturbed, cavity stabilized beams, shown in Figure 20 b). We observe frequency excursions on the order of 30 Hz over 10 s and fluctuations of 7 Hz standard deviation, after subtracting a linear drift of 0,21 Hz/s.

These two measurements show that the laser frequency fluctuations can partly, but not dominantly accounted for by an instability of the electronic PDH error signal and its offset. We assume that the drift of the optimal offset setting also results from small environment changes such as the temperature of the electronics. To limit such influences, we placed the laser control electronics under the temperature stabilized flow box of the laser table in our setup.

To properly correlate fluctuations of the beat frequency to error signal fluctuations, a simultaneous measurement of the PDH error signal, ideally of both cavity locks, and the beat frequency needs to be recorded. This would give estimates on the influence of undesired PDH offset signal excursions on the frequency instability of the clock 1 laser in contrast to desired corrections of the laser frequency to the cavity resonance. Beat measurements of the two cavity stabilized beams are discussed and evaluated in detail in chapter 3.7.1.

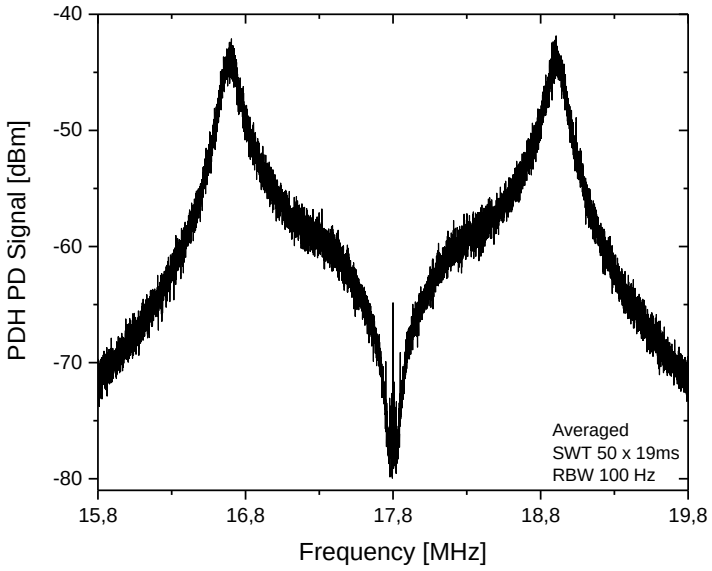

Figure 19: PDH photodiode signal around modulation frequency of $\omega_0 = 17.8$ MHz. The servo bumps of the lock are at more than 1,1 MHz away from the modulation frequency, indicating a similarly large regulation bandwidth. This exemplary plot was recorded with large regulation gain, resulting in the visibly pronounced, slightly spiked regulation loop resonances ("servo bumps"). A non-vanishing signal at modulation frequency indicates an electronic offset or offset of the lock point to the resonance frequency.

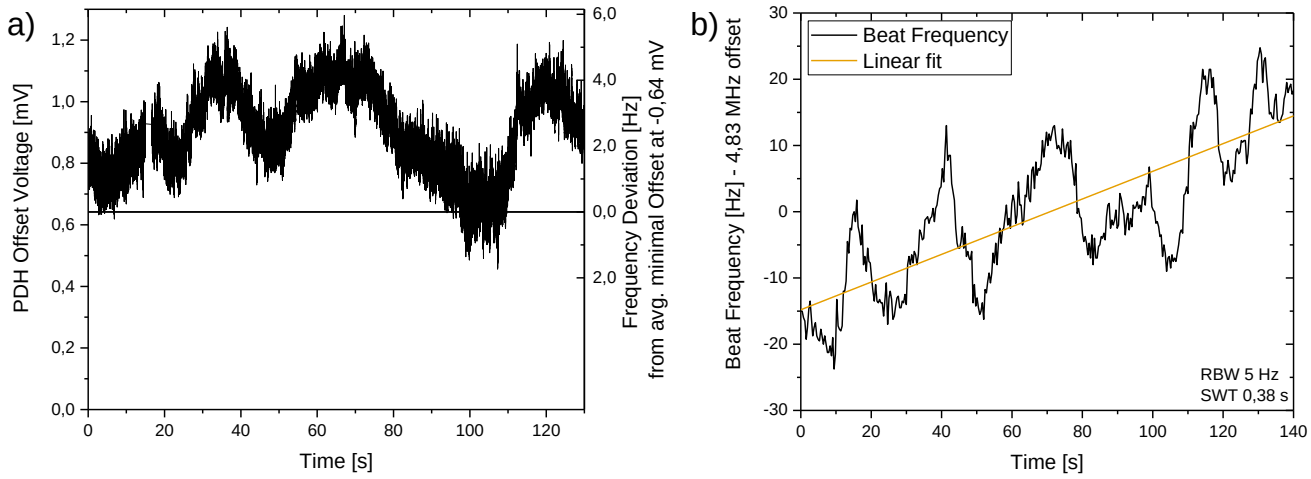

Figure 20: Fluctuations of the PDH offset voltage and laser frequency drifts over time. a) Exemplary data showing the PDH photodiode signal at modulation frequency ω_0, recorded with the spectrum analyser in "zero span" mode at a resolution bandwidth of 300 Hz. The voltage fluctuations are converted into frequency deviations (right y-axis scale) with the central error signal slope value of 107 µV/Hz and after removing an offset of 0,64 mV PDH photodiode signal. This offset was determined by averaging over the minimal offset interval around 100-110 s. b) Drift and fluctuations of the beat frequency between the two PDH locked, undisturbed laser beams over time in a subsequent measurement. The data shows frequency excursions over 30 Hz within 10 s and fluctuations of 7 Hz standard deviation after subtracting a linear drift of 0,21 Hz/s (orange fit line).

3.5 Intensity Stabilisation

I showed the systems' sensitivity to beam power fluctuations of $46 \pm 10\ \mathrm{Hz}/\mu\mathrm{W}_{\mathrm{tr}}$ (with respect to the cavity transmitted power). The cavity (especially its mirror substrates) and the offset in the PDH error signal were found to be sensitive to power fluctuations. To avoid frequency fluctuations of the laser system due to intensity fluctuations of the beam, we use an intensity stabilisation loop in the system. It is realized with a self-built PI-controller acting onto the RF-power applied to an AOM (AOM 2 in Figure 6) just before the fibre link to the vibration isolation table. Two photodiodes are available for intensity monitoring, one monitoring the incoming beam power before the cavity (PD 1) and one monitoring the cavity transmission (PD 2). The former photodiode monitors the light power reflected by a pickup mirror after the EOM. To have a good power sensitivity, 82% of the total incoming light are reflected by the pickup mirror onto the monitoring photodiode[25]. The ratio of power on the photodiode over power in front of the cavity is about 7,4. The second photodiode available for intensity stabilisation is on the transmission side of the cavity. This photodiode[27] was selected to work well for sub-microwatt powers present at cavity transmission.

When determining the power sensitivities of the cavity and of the PDH lock above, I showed that a transmission intensity stability of $1 \cdot 10^{-2}$ (being a high estimate) is required to achieve sub-Hz linewidths regarding the cavity's power sensitivity in the PDH system. Operating with an intensity stabilisation using a photodiode before the cavity in these measurements, I showed a relative transmission intensity stability of $2 \cdot 10^{-3}$ with peak fluctuations up to the relative level of $1 \cdot 10^{-2}$. These values show that the intensity regulation is, in general, working sufficiently well.

In an earlier, intermediate stage of the new cavity and PDH setup, I used an audio analyser to look at the noise spectra of the photodiode signals. The noise spectra help to find a good gain setting in the PI controller and to observe the general effect of the intensity regulation. Furthermore, I wanted to see the effect of the cavity with its low pass characteristic onto the intensity noise.

Figure 21 shows the intensity noise spectra of two photodiodes, one in front of the EOM and the other one in cavity transmission. Two regulation situations were compared, the regulation loop acting via the photodiode in front of the EOM (Figure 21 a) and c)) and the regulation loop via the transmission photodiode (Figure 21 b) and d)). Each noise spectrum shows the intensity regulated and unregulated case for the respective photodiode and regulation configuration.

Looking at the case of regulating the intensity in front of the EOM, the in-loop signal shows that the intensity noise is reduced to the dark noise level of the photodiode for frequencies up to about 6 kHz and then slowly increases for increasing frequencies. Tuning the gain of the PI controller, we could shift the regulation loop resonance up to ≈70 kHz. On transmission of the cavity, intensity noise is reduced especially for frequencies up to 10 kHz, and we see only little effect for higher frequencies. The overall course of the regulated intensity noise spectrum is

decreasing for increasing frequencies. The dark noise level for the transmission photodiode is an order of magnitude below the observed signals. Apart from this, we see no effect of the cavity. We interpret this as a sign that the noise spectrum could be reduced further, or additional noise sources are reducing the effect of the intensity regulation.

In the regulation configuration using the transmission photodiode, the in-loop signal (on cavity transmission) shows a significantly decreased noise spectrum at frequencies below 5 kHz, rapidly increasing and crossing the unregulated level at about 9 kHz. We adjusted the gain such that the regulation loop resonance was at about 13 kHz, balancing a good noise reduction and limited noise level at the resonance. We interpret the reduced regulation bandwidth to result from the low pass characteristic of the cavity having a linewidth of $\Delta\nu_{FWHM} = 8{,}9$ kHz. The respective noise spectra in front of the EOM show a limited effect of the intensity regulation: noise is reduced only up to ≈6 kHz, but to a high noise level of about one magnitude above the photodiode dark noise. Around the regulation loop resonance, over the broad frequency range of ≈6-38 kHz, the in-regulation noise spectrum is significantly above the unregulated intensity noise level.

Overall, we observed a reduced effect of the intensity regulation acting across the cavity. One reason might be the PDH lock actively stabilizing the laser frequency to the cavity resonance. Due to the Lorentzian shape of the cavity resonance, deviations in laser frequency translate into intensity fluctuations. Therefore, an overall worse PDH lock configuration results in higher intensity noise levels on the other side of the cavity. However, converting the PDH error signal via the error signal slope into frequency deviations shows deviations far below 10 Hz with exceptions of up to 100 Hz at the carrier frequency. Compared to the cavity linewidth of 9 kHz, such deviations hardly affect the transmitted power.

For atom spectroscopy measurements at an expected linewidth of several hundreds of hertz, both configurations of the intensity regulation were working sufficiently well. The high-resolution spectra were recorded with the intensity regulation of the transmission photodiode. The reasoning was to minimize power fluctuations inside the cavity, which we achieved best in the transmission intensity regulation.

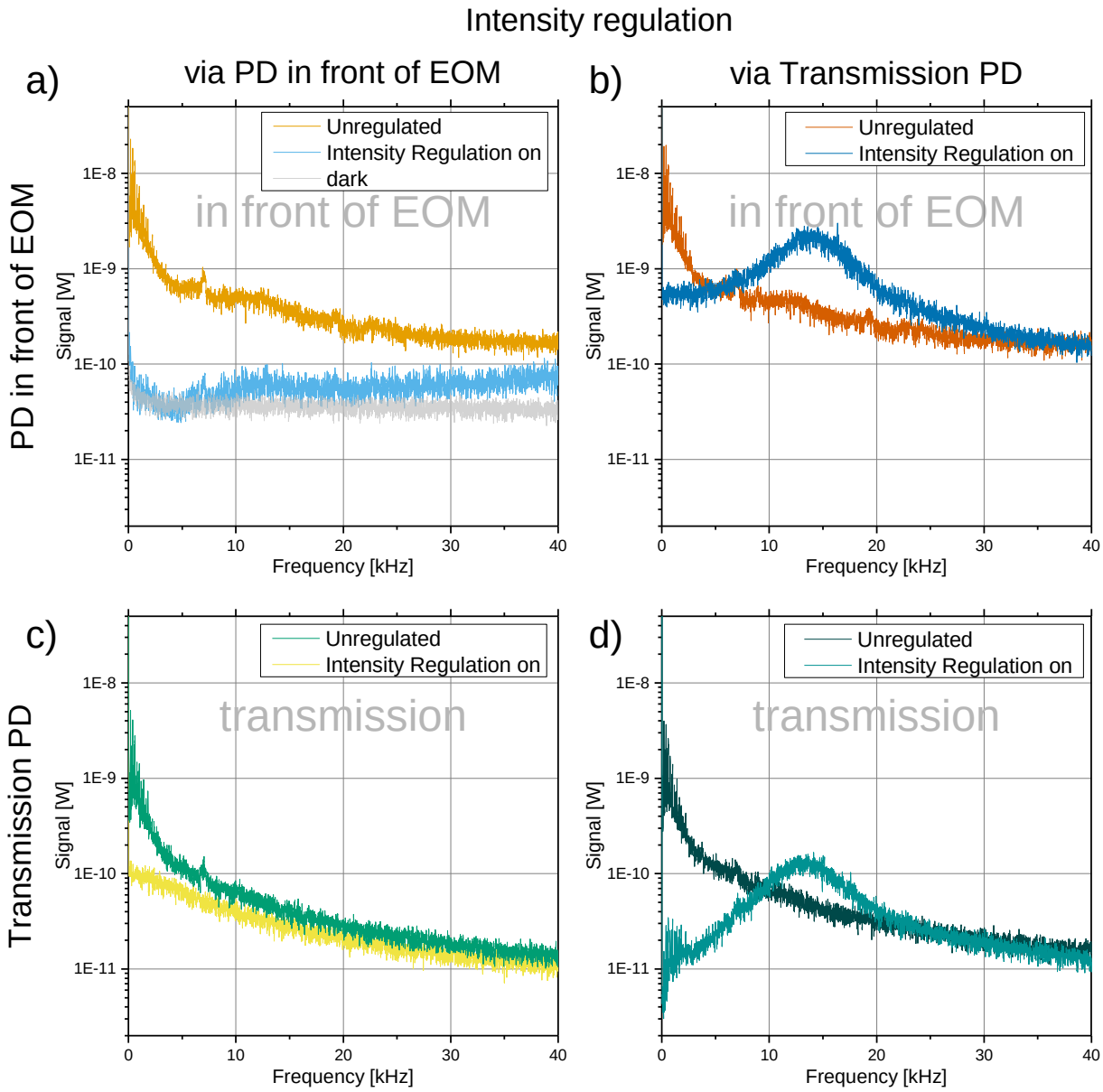

Figure 21: Beam intensity noise in the PDH system, also showing the effect of the intensity regulation on intensity noise on the opposite side of the cavity. Noise spectra of a photodiode before the EOM and of the cavity transmission photodiode are shown for an intensity regulation acting via the photodiode (PD) before the EOM (a) and c)) or via the transmission photodiode (b) and d)). Each graph shows the intensity noise spectra for unregulated and intensity stabilized case. The upper row shows the spectra for the photodiode in front of the EOM, the lower row for the transmission photodiode. Therefore, graphs a) and d) show in-loop spectra, while b) and c) are independent from the intensity regulation loop. A discussion is given in the main text.

3.6 Further changes in the setup

3.6.1 Reduction of Residual Amplitude Modulation (RAM) noise

In our previous analysis we observed a fluctuation of the offset signal in the PDH lock, relating to frequency instability of the lock. Such noise can be caused by residual amplitude modulation (RAM). RAM refers to the imperfections of the sidebands generated in the phase modulation process. Experimental conditions, especially acting on the phase-modulator crystal, may result in the sidebands having unequal magnitude and-or not being opposite in phase. Furthermore, phase modulation projects the unregulated low frequency laser intensity noise to the sideband frequencies. As the interference between sidebands and carrier generates the frequency error signal, noise and impurities in the sidebands transform into offset fluctuations and therefore frequency instability of the laser.

A predominant cause of RAM results from the electro-optic modulator crystal [89]: Temperature dependent birefringence variations, local impurities causing scattering and etalon effects, spatial inhomogeneity of the electric field and amplitude fluctuations of the driving RF power all diminish the phase modulation. Misalignment of the linear laser beam with one of the principal polarization axes of the crystal further causes impure phase modulation [87,88]: Individual phase shifts of light components along the two crystal axes result in an elliptical polarization with different degrees of ellipticity for carrier and sidebands. This effect also converts into amplitude modulation by subsequent polarization selective optical components. In fibre-coupled EOMs a small misalignment between the PM fibres principal axes and the extraordinary crystal axis cannot be avoided during EOM production and cannot be eliminated afterwards by external light polarization adjustment. Outside the EOM, vibrating components, etalon effects between flat surfaces and spatial distortions as beam clipping or scattering cause additional RAM [90]. All these effects are sensitive to external influences such as temperature variations and mechanical vibrations, leading to non-zero, time-varying frequency offset noise. Therefore, an active regulation is necessary to eliminate RAM induced offset variations, to stabilize the remaining offset signal and thereby achieve an optimal locking performance.

A derivation of RAM due to misalignment between the light polarization and the electro-optic modulator crystal is given by Wong and Hall [89]. They describe the phase shifts experienced by a linear polarized electric field propagating along the ordinary (o) and extraordinary (e) axes of the electro-optic crystal. Phase shifts can result from natural birefringence ($\phi_{o,e}$), from birefringence induced by DC electric fields (${\phi_{o,e}}^{dc}$) and by RF electric fields ($\delta_{o,e}\sin(\omega_m)$) applied across the crystal (commonly along the extraordinary axis). Equation (3.21) exemplarily shows the phase shift from the natural birefringence $n_{e,o}$ along the respective crystal axis.

$$\phi_{e,o} = 2\pi \frac{l_{cry}}{\lambda} n_{e,o} \tag{3.21}$$

l_{cry} is the crystal length and λ is the optical wavelength. Next, Wong and Hall define polarization alignments of a polarizer (before the crystal) and an analyser (after the crystal) under the angles β and γ with respect to the crystal's extraordinary axis. From the electric fields, they derive the effective beam power after passing the EOM crystal. In addition to the individual power components along the ordinary and extraordinary crystal axes, an interference term in the output beam power contains the two crystal axes' phase shifts and the RF phase modulation. Considering the output of a monitoring photodiode, they expand the phase modulation into Bessel functions and regard the sideband powers at the Fourier components $k\omega_m$ (with $k > 0$).

$$I(k\omega_m) = \frac{1}{2}\sin(2\beta)\sin(2\gamma)\, P_0\, J_k(M)[\cos(\Delta\phi + \Delta\phi^{dc} + k\omega_m t) + (-1)^k \cos(\Delta\phi + \Delta\phi^{dc} - k\omega_m t)] \tag{3.22}$$

Here, P_0 is the total power, $J_k(M)$ is the kth-order Bessel function with amplitude-modulation depth M. $M = \delta_e - \delta_0$ is the difference of the RF modulation depths of the two crystal axes. $\Delta\phi$ is the phase shift from the difference in natural birefringence of the two crystal axes and $\Delta\phi^{dc}$ is the equivalent phase shift induced by a DC electric field applied across the crystal. These phase shifts are stress and temperature dependant. The two summands in the brackets are the negative and positive order sideband. As discussed above, the interference term vanishes for perfect alignment of the input or output electric field with the extraordinary crystal axes. However, the alignment is sensitive to external influences as temperature and vibrations.

Wong and Hall state that RAM from impure phase modulation due to polarization crosstalk at the electro-optic crystal is present when odd harmonics sidebands powers are present. Therefore, one can monitor RAM by the intensity at the first order of the modulation frequency. Equation (3.22) then reduces to the equation (3.23):

$$I(\omega_m)|_{\mathrm{k=1}} = -\sin(2\beta)\sin(2\gamma)\, P_0\, J_1(M)\sin(\Delta\phi + \Delta\phi^{dc})\sin(\omega t) \tag{3.23}$$

All uneven interference terms vanish at any polarization configuration if $\sin(\Delta\phi + \Delta\phi^{dc}) = 0$, i.e. when phase shift from the natural birefringence is compensated by the phase shift of the DC electric field. Varying the temperature and the applied DC electric field at the crystal enables external control and a feedback loop for the cancellation of RAM. Expression (3.23) holds in first order for fibre coupled EOMs, in which additional misalignments between the light polarization, the slow axes of PM fibres and the crystal axes occur [88].

For RAM monitoring and stabilisation setups presented in [87,89,90], the PDH setup is extended by a pickup and fast photodiode monitoring the incoming light. As the feedback loop stabilizes the RAM up to the monitoring photodiode, the photodiode should be placed close to the cavity. The photodiode RF output at the modulation frequency is mixed down with the local oscillator signal (phase-stable to the EOM modulation) in a double balanced mixer. The in-phase output is the error signal for the DC voltage feedback acting via a PI controller, and the

quadrature output is the error signal for temperature correction. A phase shift of the local oscillator reference signal needs to be adapted for maximal error signals. While the RAM due to polarization mismatch to the crystal axis in equation (3.23) does not contain a cosine quadrature component, effects such as spatial non-uniformity in the wave front or beam steering can produce additional RAM noise [87,89]. The temperature correction extends the RAM regulation bandwidth at low frequencies below 0,1 Hz. Additionally, components are placed slightly tilted to the beam path and optical isolators are used where possible to prevent reflections and etalon effects. Also, care is taken not to cut off parts of the beam which would cause a spatial dependence of the detected RAM signal. With the full RAM compensation active, Zhag et al. [87] achieved to suppress RAM by 56 dB compared to an unregulated signal, with a small remaining peak being stable at the 3% level.

It turned out that the fibre-coupled waveguide-based EOM in our setup[24] only supports light propagation on the extraordinary crystal axis. On the positive side, this property inhibits the predominating RAM (ellipticity of the FM triplet) source originating from cross-coupling of the crystal polarization axes. However, applying a DC voltage has no effect on the RAM but only modifies the total transmitted power, therefore not enabling an active regulation of remaining RAM noise via DC feedback. Foltynowicz et al. [91] compared the performance of a temperature stabilized fibre EOM only guiding along its extraordinary axis (due to a proton exchanged waveguide) with that of an fibre EOM allowing active RAM compensation via DC feedback in a noise-immune cavity-enhanced optical heterodyne molecular spectroscopy (NICE-OHMS) experiment. They showed that the two RAM suppression approaches achieved similarly good sensitivities in doppler-broadened and sub-doppler detection experiments, being far better than without any RAM reduction solution. However, due to the lack of a feedback mechanism in the only temperature stabilized, protonated waveguide-based EOM, slow drifts affected the sensitivity in the passive RAM reduction approach on timescales above a few hundred seconds.

We realized a temperature stabilized fibre-coupled EOM only wave-guiding along the *e*-axis in our setup together with a fast photodiode[26] for RAM monitoring. The special waveguiding behaviour of the EOM resulted in a generally very low RAM signal. Detecting that low intensity RF signal required a high RF sensitivity of the photodiode, which limited the maximum optical power of its optimal linear operation regime to few microwatts. The low operation power rendered the DC monitoring output of the photodiode too insensitive for intensity monitoring and regulation. Therefore, intensity monitoring of the beam before the cavity was realized with another pickup and photodiode. The fibre EOM is mounted on a temperature stabilized copper block and electrically isolated from the ground, as required for potential DC voltage application. It is placed in an aluminium box for temperature and RF isolation.

So far, we only realized a temperature stabilisation to a fixed set-value, without additional regulation input for the quadrature error signal of the RAM photodiode. Li et al. [90] showed that a fixed temperature stabilisation already has large effect in reducing RAM amplitude fluctuations. The temperature periodicity of the phase shift in a magnesium doped LiNiO is

about a period per few Kelvins, depending on crystal doping and on crystal length and optical wavelength (see also equation (3.21)) [90,91]. We qualitatively verified this with our fibre EOM in a test setup. Figure 22 shows the RAM signal while reducing the EOM temperature from $\approx 23{,}9\,°\mathrm{C}$ to $\approx 21{,}9\,°\mathrm{C}$. We observe several cycles of the RAM amplitude while approaching the set temperature in the $2\,\mathrm{K}$ temperature shift. This sensitivity shows the necessity of a temperature stabilisation. In the final setup, we adjusted the EOM temperature to minimize the observed RAM amplitude.

Even though this waveguide-based, fibre coupled EOM may not be well suited for active RAM regulation due to its single-axis waveguiding property, the literature suggests that the dominant RAM noise source of polarization cross-talk in the EOM crystal is eliminated by that feature and remaining RAM drifts are assumed to be on similar scales as in actively regulated configurations. We implemented an important temperature stabilisation of the EOM and a slow RAM regulation feedback loop via the temperature is desirable. As all light mismatched to the crystal's extraordinary axis is lost in the waveguide, remaining drifts in the crystal are expected to reflect on the total intensity after the EOM. With the photodiodes for intensity regulation in our setup located after the EOM, we assume to have an actively stabilizing mechanism in place.

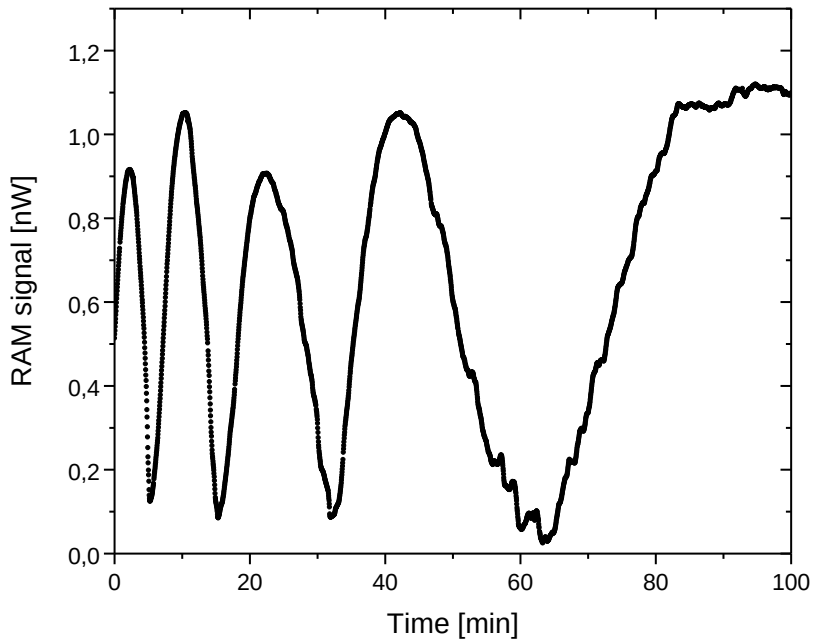

Figure 22: Temperature sensitivity of RAM amplitude in a test setup. Oscillations of the RAM amplitude were observed when reducing the temperature of the fibre EOM by 2 K and approaching set temperature of 21,9 °C. Temperature control by a heating foil and limited heat dissipation are assumed to accentuate the slowing approach to the set temperature indirectly observed here. The temperature (PI-)controller was yet fine-tuned after this measurement. The optical power used in the test setup was significantly larger than in the final PDH setup, therefore the registered amplitudes do not compare to the signal levels present in latter measurements.

3.6.2 Other improvements: Hanging cables, transmission PD tower

I implemented several minor detail changes in the setup with the aim to improve the overall performance. However, it is not possible to quantify the effect of these measures.

Attempting to reduce the transfer of vibrations from the laboratory environment to the vibration isolation table, I rigidly clamped and additionally taped all electric cables to the base optical table. They can be seen on the photos in Figure 7. The cables were then guided over high posts, hanging there loosely to further dampen possible vibrations coming from the laboratory.

At the cavity temperature regulation, I observed a high sensitivity of the resistance signal to the position and movements of the electric cable connection of temperature controller to the cavity chamber (and the thermistors therein). I ensured that the thermistors at the heat shield in the vacuum chamber connect only via copper wiring and copper clamp connectors to the temperature regulation board. On this way, we avoid material transitions which would give rise to thermoelectric voltages varying with the environmental temperature and thus distort the actual thermal resistance signal. To reduce environment influences onto the copper signal cables, I wrapped the cables with aluminium foil for electric isolation and placed them in a guiding tube which was well fixed in the laboratory.

When closing the wooden, noise isolation covered box around the cavity system, the power consumed by enclosed devise causes a rise in temperature in the box. The temperature curve in the box follows an exponential approach with an exponential approach time constant of 8,5 hours and a final temperature difference of 3,5 K to the exterior. Optimal operation with minimal drifts of the clock laser locked to the cavity is therefore only possible several days after closing the box. Additionally, the wooden box delayed and damped larger air humidity changes occurring in the laboratory.

3.7 Stability evaluation

Three methods are available to analyse the drifting behaviour of the cavity: The first method is the beat measurement between the cavity 1 beam and the GPS stabilized comb, as used for the determination of the zero-expansion temperature. In these measurements, frequency drifts unrelated to cavity temperature changes indicated a long-time drifting velocity on the order of 0,31-0,36 Hz/s. The second method observes the beat between two cavity stabilized systems and is presented in the following subchapter. Comparable measurements with the previous cavity setups showed drift velocities of several Hz/s and frequency fluctuations of 20-80 Hz on experimentally relevant time scales (see section 3.2.2). We expect to see a larger drifting behaviour in the cavity beat measurements compared to the cavity 1 - comb - beat measurements, as two independent and not referenced cavity-stabilized systems are involved, especially with cavity 2 showing a high temperature sensitivity. Therefore, the beat of two cavity systems is rather useful for analyses on short and intermediate time scales. The third option to analyse long-term drift behaviour is the logging of the laser frequency setting at resonance with an atomic transition. This is presented in the last subchapter.

3.7.1 Beat measurement of new cavity 1 and old cavity 2 setups

To analyse the linewidth and frequency stability of the clock laser we measured the beat note with an independent PDH lock to a second ultra-stable cavity. Figure 23 shows the schematic setup for beat note measurements between the two PDH setups. Directly at the laser output, the beam is split into two branches going to the two PDH setups. In each branch, a fast feedback AOM enables the PDH lock to the cavity and a second AOM shifts the laser frequency to the cavity resonance as well as serves as actuator for intensity stabilisation of the beam in the PDH setup. Most of the beam power in each branch is picked up after the fast AOM and available for experiments. For the beat note analysis, the two experiment branches are overlapped with a beam splitter and sent onto a photodiode[33]. The beat note is monitored on a spectrum analyser or logged with a frequency counter.

Description of the cavity 2 setup

The second PDH setup is highly like the initial PDH setup at cavity 1, also based on a vertical, "football" geometry ultra-stable cavity in an identical vacuum setup. The cavity is made of fused silica mirrors bonded to an ULE glass spacer, with a finesse of $\mathcal{F} = 103000$ [53] and a zero-expansion temperature at $T_{CTE-ZC}^{cav2} = -26 \pm 2$ °C. It is operated at a temperature of $T^{cav2} \approx 0{,}6$ °C at which temperature its frequency sensitivity to temperature fluctuations was deduced to be $\partial\nu/\partial T = -26$ kHz/mK [58]. The commercial temperature controller chip[34] operates with a stability of 1 mK (given by the data sheet). The photodiode registering the PDH signal is a home-made photodiode with a bandwidth of about 25 MHz [73]. The EOM for phase modulation is a free space EOM[35] with two electro-optic crystals at Brewster angle. The

[33] Menlo FPD510-FV
[34] Wavelength Electronics WTC3243
[35] Linos PM25 VIS

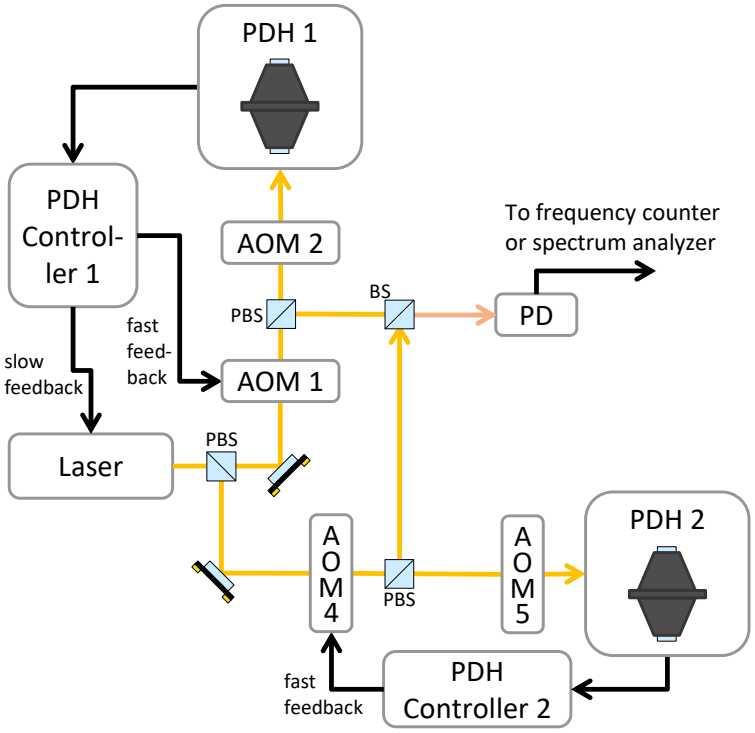

Figure 23: Scheme of the beat measurement setup for stability evaluation of the cavity stabilized laser. A PBS splits the laser beam in two branches, which then pass a fast feedback AOMs (AOM1, resp. AOM4) of two independent PDH lock setups. The slow feedback of the PDH1 setup acts onto the laser's master oscillator ECDL piezo. A second AOM in each beam path (AOM2, AOM5) in double pass configuration serves to shift the laser frequency with respect to a cavity resonance, and for intensity stabilisation in the PDH setup. AOM2 is further used to feed-forward a drift compensation of the laser beam. The major power of each laser branch is available for experiments, such as beat note monitoring via a photodiode and connected spectrum analyser or frequency counter.

modulation frequency is 15,8 MHz and the driving signal is fed to the EOM via a self-built LC resonator. We assume this reaches a modulation depth on the order of $\beta \approx 0{,}48$ (like it was characterized for the initial cavity 1 setup), which corresponds to 60% of the optimum PDH frequency discrimination normalized to the optical power. The intensity stabilisation in that PDH setup was realized via a photodiode before the EOM, in contrast to stabilisation of the cavity's transmitted power in the new cavity 1 setup. Cavity 2 exhibits a large intensity sensitivity of about 620 ± 30 Hz/µW (referring to the cavity's transmitted power). Taking 8 µW power transmitted through cavity 2 and a relative intensity stability of 0,2%, we expect a contribution of short term frequency fluctuations from intensity noise on the order of 10 Hz. The only feedback mechanism for the PDH lock to cavity 2 is the fast AOM in the beam path, as the PDH lock to cavity 1 operates the slow feedback to the laser master oscillator ECDL. The cavity 2 PDH lock has a regulation bandwidth of about 800 kHz.

Without the cavity 2 setup locked, the beat note between the two arms shows the linewidth of the unstabilized laser with a FWHM of about 80 kHz, formed by narrow laser emission line fluctuating fast within the overall emission spectrum.

Beat measurement results and analysis

When both PDH locks are active the power spectral density of the beat note shows a narrow carrier peak which is over 60 dB above a noise pedestal extending the servo bandwidth of 1 MHz, shown in Figure 24 a). Over 99,9% of the power is in the central peak. Zooming in onto the carrier shows the presence of low frequency noise, especially in the frequency range up to 500 Hz, which can be seen in Figure 24 b) and c). Noise sources from the environment are acoustics, air currents and pressure fluctuations, vibrations, and electronic noise. The electric mains couples in electric noise peaks in harmonics of 50 Hz from the carrier frequency, which can be seen in all spectra.

The beat spectra shown in Figure 25 display the ability of the realized laser stabilisation on short and intermediate-short time scales. The observed beats show the sum of the individual laser line widths, assuming Lorentzian line shapes. A Lorentzian line shape would result from a flat noise spectrum of the laser within the relevant bandwidth. At 1 Hz resolution bandwidth (RBW) of the spectrum analyser, with a sweep time (SWT) of 1,9 s, the beat spectrum of the two cavity-stabilized beams is fitted well with a Lorentzian with FWHM of 0,84 ± 0,01 Hz. The 1 Hz RBW was the resolution limit of the available spectrum analyser. Averaging over 36 s, low frequency fluctuations of the carrier broaden the spectrum to a Lorentzian FWHM of 4,29 ± 0,03 Hz. Over longer averaging times the frequency fluctuations broaden the spectrum to a Gaussian line shape: After 62 s, the spectrum fits to a Gaussian with FWHM of 8,41 ± 0,01 Hz, and after 95 s to a Gaussian FWHM of 10,74 ± 0,01 Hz. Linear frequency drifts were compensated by sweeping the frequency of one AOM during these measurements.

To obtain statistics about the laser stability on short time scales, I recorded the cavity beat with the spectrum analyser at reduced resolution bandwidth - and therefore faster sweep time - over several minutes. The consecutive spectra were then fitted with Gaussian line shapes which best matched the resolution limited curves. Figure 26 shows several statistics of the fitted beat width (Gaussian FWHM). At 2 Hz resolution bandwidth, with 0,9 s sweep time, over 70% of the beat spectra were below 3 Hz width. Increasing the resolution bandwidth to 3 Hz, with 0,63 s SWT, over 80 % of the spectra were fitted below 4 Hz width. Over 90% of the fits were well below 5 Hz width. This statistical analysis relies on the fitting curves matching to the spectra observed over the sweep time of the spectrum analyser. The fitting statistics show that the Gaussian curves give reliable fit results for the observed spectral widths.

The observations of the narrow beat spectra at 1,9 s sweep time and the statistical analysis of the spectral widths let us assume that the laser linewidth is on the scale of 1 Hz or better on experimentally relevant short time scales (of tens to hundreds of milliseconds). The width and centre frequency of the monitored beat spectra were highly sensitive to external influences, such as vibrations and pressure changes. We assume that the missing phase stabilisation in the fibres guiding the laser branches to the vibration isolation tables is a significant noise source – especially of low frequency noise – remaining in the cavity 1 laser stabilisation setup.

Implementing a phase- and intensity-stabilisation in the beat monitoring setup will reduce influences from instabilities external to the locking setups onto the observed signal.

With the improvements of the cavity 1 setup, especially the new cavity 1 operating at its zero-expansion temperature, we expect a better frequency stability for the cavity 1 stabilized beam, especially on intermediate to long time scales. However, it is not possible to isolate the performance of only one laser stabilisation system from these beat measurements. Having a third laser system for beat measurements with the clock lasers would enable triangular Allan Deviation measurements allowing to extract the individual locking performances of each laser. The next laser system available in the laboratory for beat measurements with the clock laser is the frequency comb. However, with a spectral width of tens of kHz, the beat is too imprecise and the Allan Deviation too large for comparisons with the narrow, cavity stabilized laser beams, especially on short or intermediate time scales.

Extracting the Allan Deviation from the frequency fluctuations of the cavity stabilized beat could give further information on the combined frequency stability on all time scales. Fast fluctuations of the spectra's peak frequency recorded at short sweep times (and correspondingly low-resolution bandwidth) could give similar information as the statistical analysis of spectra's widths. Such Allan Deviations are shown later in this chapter.

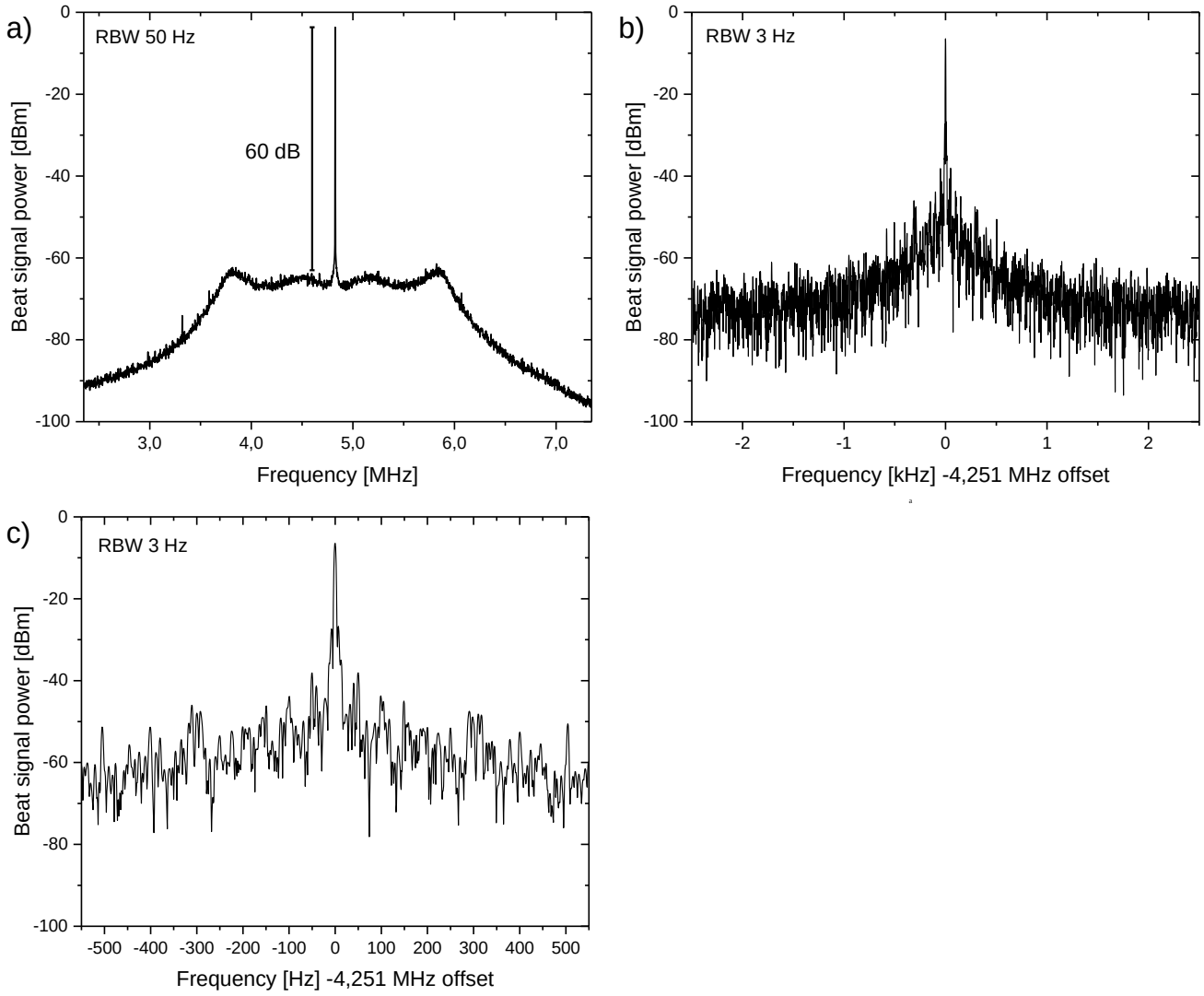

Figure 24: Electric power spectral density plots of the beat note of the clock 1 and clock 2 PDH stabilized laser beams, observed with a spectrum analyser. Plot a) shows the noise pedestal of the ECDL SHG system remaining with the PDH lock active. Corresponding with the PDH lock bandwidth the pedestal extends over ±1 MHz from the carrier and falls off at frequencies beyond that. The carrier peak is over 60 dB above the noise pedestal and contains 99,92% of the total power. Plot b) and c) give detailed views in the kilohertz, resp. hertz range with increased resolution bandwidth of 3 Hz. They show low frequency noise at and close to the carrier, resulting from vibrations, acoustics, and electric noise (latter especially at harmonics of 50 Hz to the carrier).

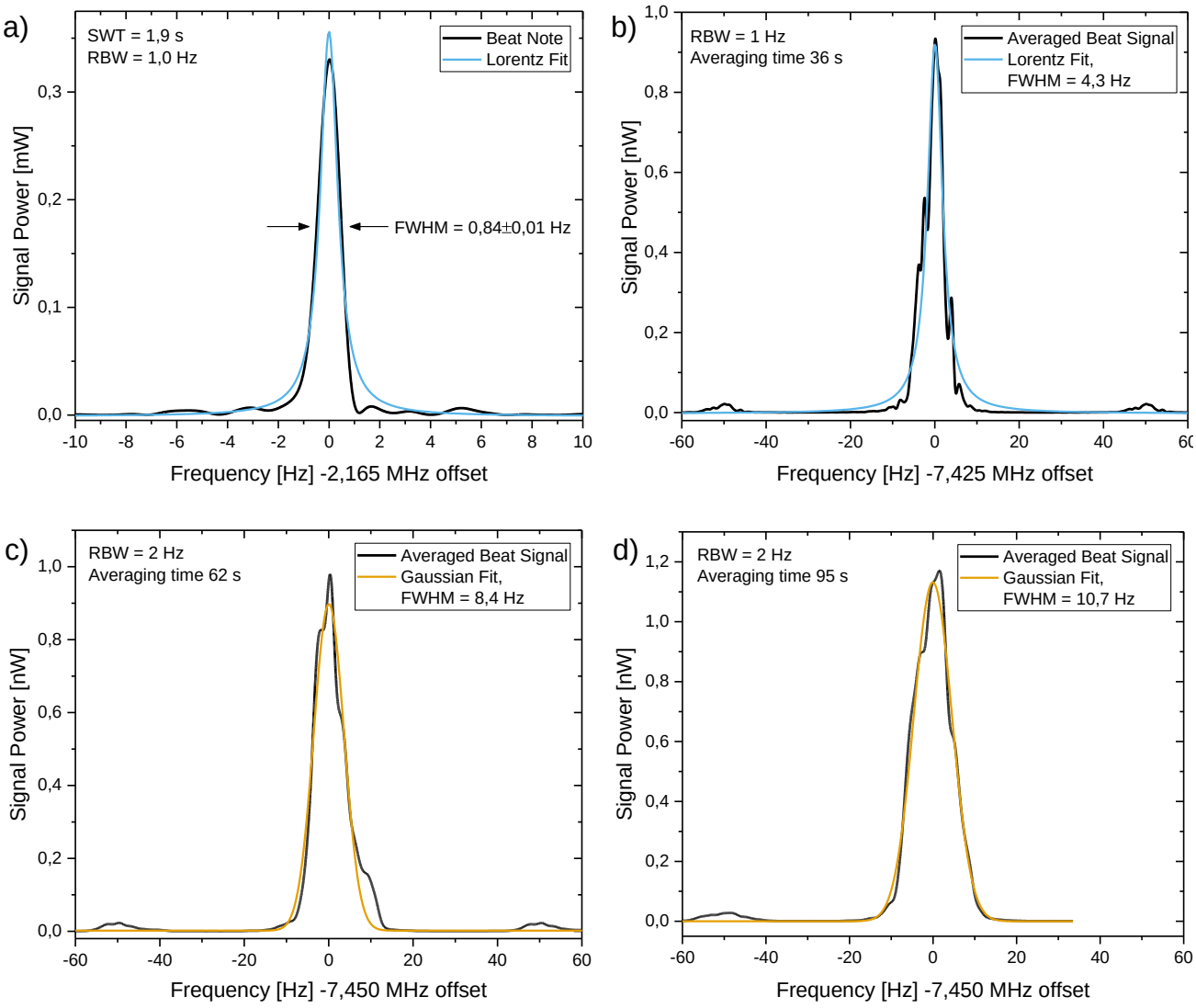

Figure 25: Power spectral density plots of the beat note of the two independently locked clock laser beams. Shown are the electric power at the spectrum analyser around the carrier beat frequency, averaged over various times, together with Lorentzian or Gaussian fits. Plot a) shows a single sweep at resolution bandwidth (RBW) of 1 Hz and sweep time of 1,9 s. A Lorentzian fit with FWHM of 0,84 ± 0,01 Hz matches the spectrum. A linear drift compensation of -1.56 Hz/s via AOM frequency sweep was active during the measurement. Low frequency noise broadens the spectra over extended time scales. Plot b) shows a spectrum averaged over 36 seconds with Lorentzian fit of 4,29 ± 0,03 Hz FWHM. The settings were the same as for plot a). Plot c) and d) show extended averaging times of 62 s, respectively 95 s, with spectra fitting to Gaussian line shapes of 8,41 ± 0,01 Hz, resp. 10,74 ± 0,01 Hz. These spectra were recorded at RBW = 2 Hz (single frame sweep time 0,9 s) and with drift compensation of -1,46 Hz/s. The border of the observed frequency interval cuts the data in plot d). All spectra show small features from power line noise in the electronics at 50 Hz frequency difference from the carrier.

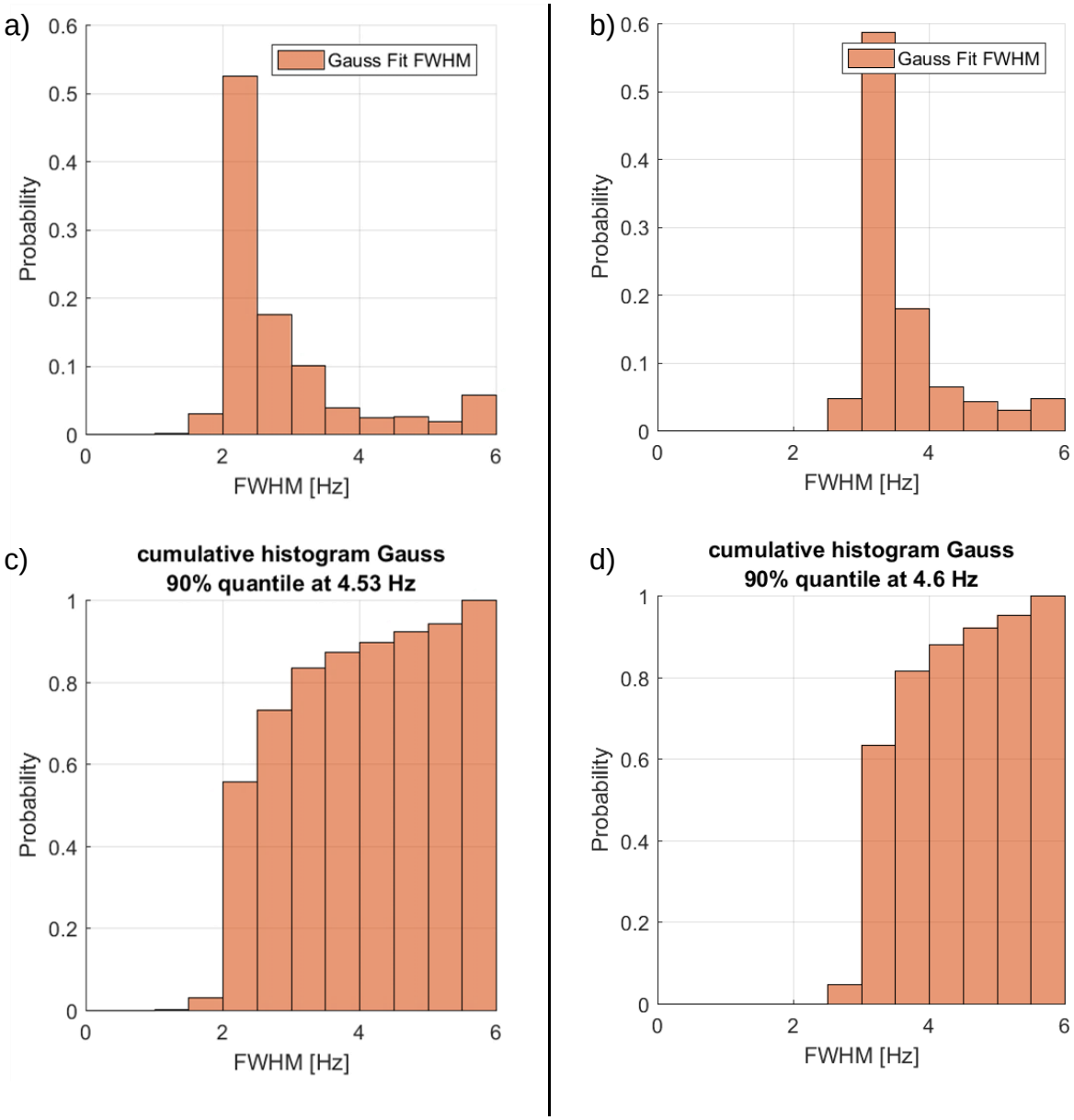

Figure 26: Histograms showing statistics on Gaussian widths (FWHM) fitted to beat spectra of the two cavity-stabilised laser branches. Part a) and c) show for the 2 Hz RBW, at a 0,9 s SWT: Over 70% of the spectra had a fitted width within 1 Hz to the resolution bandwidth, and 90% below 4,5 Hz (statistics of 690 frames). Part b) shows for a slightly shorter sweep time of 0,6 s at 3 Hz RBW: Over 80% of the fits are within 1 Hz of the RBW, and over 90% are below 4,6 Hz width (statistics of 650 frames).

Long-term measurement of the cavity 1 - cavity 2 beat

Long-term drifts and stability of the laser frequency in PDH lock are generally dominated by the temperature stability of the cavity. Another long-term effect is the aging of the cavity spacer material, causing a linear drift of the cavity's resonance frequency. Figure 27 a) shows the beat frequency drift of the two cavity stabilised laser branches observed over 24 h (from midday to midday) after subtracting a linear drift of 2,8 Hz/s. Remaining frequency oscillations are on the order of 25 kHz/day, with the beat further drifting to lower frequencies afterwards. The overall oscillation amplitude matches to the poor temperature sensitivity and -stability of cavity 2: Compared to the large temperature sensitivity of cavity 2 of 26 kHz/mK at ideally 1 mK regulation stability, the sensitivity and stability of the cavity 1 setup of 93 ± 62 Hz/mK at similar regulation stability have little to no impact.

Marked in Figure 27 a), there is a 4,5 h interval with approximately linear drift of effectively 3,8 Hz/s. Figure 27 b) shows the frequency deviations remaining after compensating that linear drift. Within four hours of this interval we observe regular frequency oscillations over 200 Hz at a period of 1,5 - 2 hours. This regular course of the beat frequency and the extended period time enables another iteration of drift compensation over a shorter interval of 1 hour, giving an effective linear drift of 3,7 Hz/s. The remaining frequency drifts and fluctuations in this 1-hour interval, shown in the inset of Figure 27 b), are well within 50 Hz. They show a slightly oscillatory course and short time fluctuations on the order of 20-30 Hz over several minutes.

We can compare this long-term drift measurement to an older, 16 hour beat measurement presented in [53], using the initial cavity 1 setup and the principally unchanged cavity 2 setup. The linear drifts of several Hz/s are similarly large in both measurements. The previous data shows smaller frequency fluctuations of only a few kHz over 24 hours and excursions within only 100 Hz over 4,5 hours, however with changes of the underlying course, or non-linear drifting behaviour, over tens of hertz on time scales of ≈ 20 minutes. Short-time fluctuations were on the order of 10-20 Hz, which fits very well to the intensity sensitivity and stability measured for the initial cavity setups.

We expected the beat between the two cavity systems to show slightly smaller intermediate- to long-term drifting and smaller (short- to intermediate-term) fluctuation behaviour with the new cavity 1, as it shows significantly improved sensitivity and stability characteristics compared to the initial cavity 1. Reasons for the general increase of the long-term drifting amplitude might be in different overall environmental conditions during the measurements presented. The observed continuing drift of the beat towards lower frequency hints to a (temperature) drift occurring. Yet, the now observed frequency course is more continuous, with small drift changes on time scales of 1 hour. This time frame better allows the setting up of a suitable drift compensation and running of a spectroscopy measurement series within one half drift "oscillation". Reasons for slightly increased fluctuations might be in the momentary PDH stabilisation settings, the momentary performance of the individual systems and in a general instability of the beat monitoring setup.

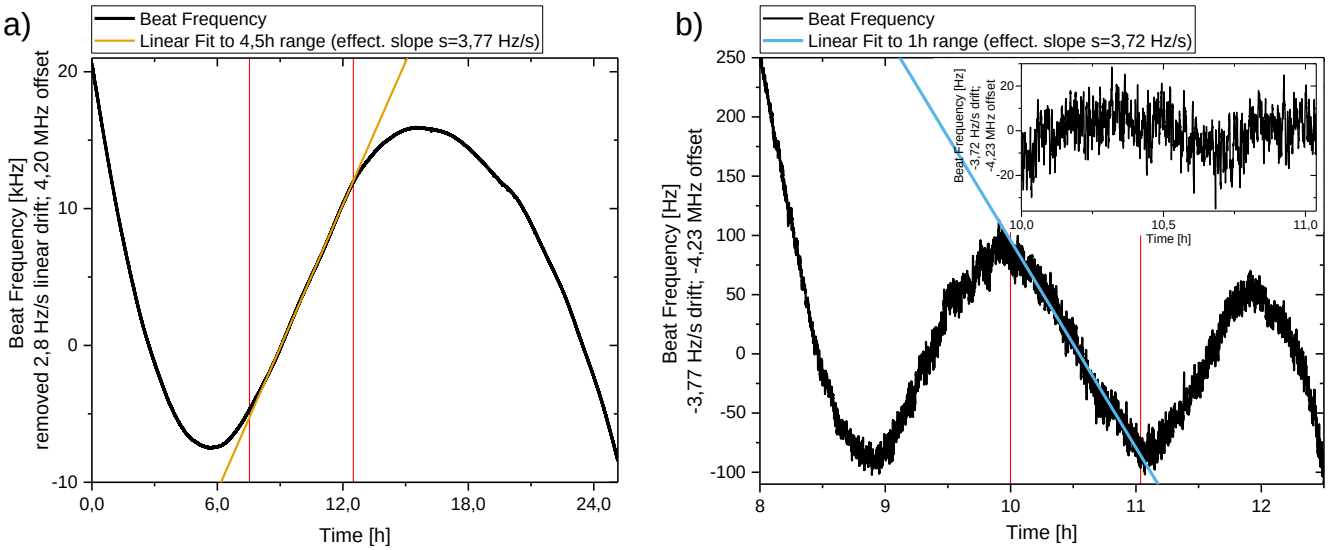

Figure 27: Long term monitoring of the beat frequency of the two cavity stabilised laser branches, starting on a Wednesday at 12:16 h. Plot a) shows that after removing a linear drift of 2,8 Hz/s, a frequency oscillation over 25 kHz over the course of 24 hours remains. A linear line with effective slope of 3,8 Hz/s is fitted to an approximately linear interval of 4,5 h (marked with vertical, red lines). Plot b) shows the residuals of the linear fit, again showing continuous oscillatory behaviour over 200 Hz with 1,5-2 h periods. A linear slope is now fitted to an approximately linear 1 h long interval, giving an effective slope 3,72 Hz/s. The residual frequency course (inset plot b)) shows a drift or oscillation within a 50 Hz range, and short frequency fluctuations on the order of 20-30 Hz.

Allan Deviation

The 1 h beat frequency interval is a good start to extract the Allan Deviation [79,92,93] of the combined cavity stabilised laser systems. However, the resulting Allan Deviation is only useful to categorize the presented data showing the combined performance of the laser systems. It at most only hints towards the performance of the new cavity 1 stabilisation setup. The underlying beat frequency measurement does not compare to Allan Deviation measurements in the clock community. The most significant reason is the large frequency instability of the reference laser, i.e. the cavity 2 stabilized beam, which in all aspects exceeds the stability and performance evaluated for the cavity 1 system. Another important reason is the missing phase and intensity stabilisation in the beat measurement setup itself, as already mentioned above. Furthermore, one should not confuse the Allan Deviation of the free-running cavity stabilised laser beat here with an Allan Deviation derived from actual, active clock operation at an atomic reference.

Figure 28 shows the Allan Deviation of the two cavity stabilized lasers' beat being between 10-15 to 10-14. The blue dots are derived from the 1 h residual frequency trace after linear drift subtraction shown in the inset of Figure 27 b). The time resolution of the frequency counter was 1 second. The Allan Deviation for shorter time scales (orange triangles) is evaluated from another, short measurement using the spectrum analyser at 50 Hz RBW and 0,04 s SWT and includes a retrospective linear drift compensation in the data processing. Additionally, the green triangles show a 'native' Allan Deviation derived from a data set recorded at 5 Hz RBW, 0,4 s SWT, with the drift compensation actively fed forward in the experiment and no post-processing of linear drift.

The overall course of the plots shows the characteristic initial reduction of the Allan Deviation with increasing averaging time τ, here reaching a minimum of few 10-15 at $\tau \approx 1$ s. For larger averaging times up to $\tau \approx 10$ s the Allan Deviation increases up to $\approx 1 \cdot$ 10-14, then decreases slightly towards a local minimum around $\tau \approx 100$ s and starts to increase thereafter.

The Allan Deviation with the new cavity 1 setup is on similar magnitude as an optimal Allan Deviation of the previous cavity 1 setup, latter significantly increasing when analysing data sets above 40 minutes duration. This is in coherence with the discussion of the beat frequency drifts and residuals in the previous section (which makes sense as the same data sets are investigated).

The Allan Deviations shown here show optimal results after data selection and partly retrospective, ideal linear drift compensation. Allan Deviations derived from extended intervals of the beat measurement (such as the 4,5 h interval in Figure 27 a)) coincide well with that of the 1 h interval up to averaging times of $\tau \approx 60$ s, and steeply increase thereafter. In principle one could follow up with an analysis of dominating noise sources, identifiable by the course of the Allan Deviation [79], or check the contribution of individual system components to the total Allan Deviation. Regarding the high instability levels of the cavity systems I focussed on the evaluation of the atom spectroscopy data, presented in the next section.

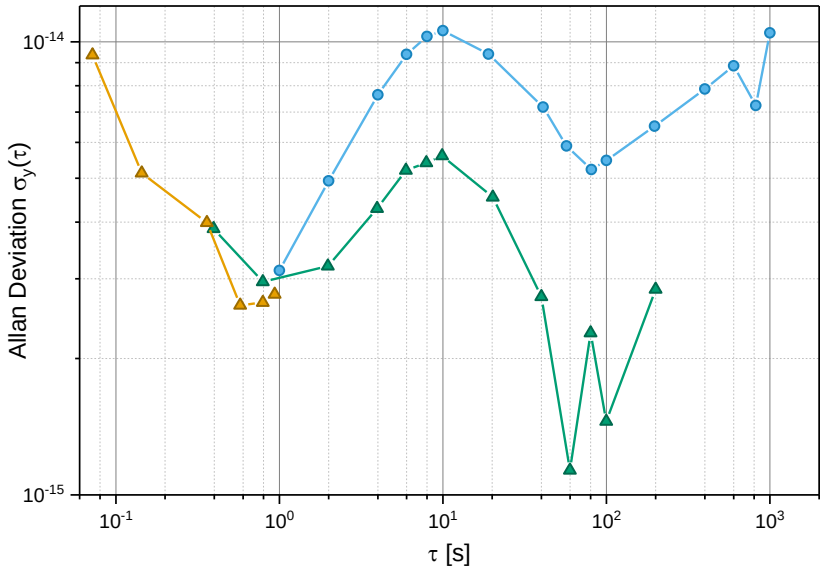

Figure 28: Allan Deviations derived from the beat note measurement between the two cavity stabilised laser beams. The blue, round data points show the Allan Deviation of an 1 h measurement after retrospective linear drift compensation, displayed in the inset of Figure 27 b). Supplementing data for time scales below $\tau = 1$ s (orange triangles) was calculated from a measurement recorded with the spectrum analyser (at 50 Hz RBW, 0,04 s SWT), with total duration of 4 minutes. The green triangles show the Allan Deviation another data set, recorded with the spectrum analyser at 5 Hz RBW, 0,4 s SWT over 7 minutes, where the linear drift compensation was performed actively during the measurement via the frequency shifting AOM.

3.7.2 Drift of the clock 1 laser observed via atom spectroscopy

When performing the spectroscopy measurements on the $^1S_0$–$^3P_0$ transition, we logged frequency shifts by the drift compensation and by manual shifts, both applied to the clock laser via the frequency shifting AOM. The log enables us to relate the positions of the resonance peak to each other over time. This presumes that the atomic resonance position is constant (i.e. comparable experimental parameters applied throughout the spectroscopy series). Deviations of electronics (digital RF sources referenced to GPS signal) are assumed as negligible. Figure 29 shows the drift of the laser resonance frequency setting over nine days of spectroscopy measurements. The long-term drift in Figure 29 a) follows a line with slope of -318 ± 1 mHz/s. This linear drift matches very well with the linear drifts observed alongside the zero-expansion temperature measurements with cavity 1 and the frequency comb. Linear long-term drifts are related to the aging of the cavity material. Values by a factor 4 to 10 smaller were published for this cavity type [64] and other (long, horizontal) cavities [62,79].

The reason for the large linear drift in this setup is unclear. It could result from a non-optimal drift monitoring and compensation scheme of updating the drift compensation between each measurement series. Another reason could be a yet non-settled optical bonding between the cavity mirrors and spacer, affecting the resonance frequency. Yet another reason could be the non-optimal temperature stabilisation solution of the cavity causing the long-term drifting behaviour.

Figure 29 b) shows the residuals to the linear fit. The largest residual frequency difference spans over 3,3 kHz around day 5-6. The inset shows that frequency deviations are within a range of 250-500 Hz on stable days. Linear drifting deviations from the long-term linear fit are up to 12 mHz/s on stable days (day 2, 7-9) and up to 33 mHz/s on days with large drifts (days 1, 5, 6).

Under the assumption that the frequency changes are only caused by temperature changes of the cavity, we can take the temperature sensitivity of the cavity of $\partial\nu/\partial T = 93 \pm 62$ Hz/mK to convert the frequency drifts to temperature changes. The linear fit deviations from the overall linear drift correspond to $0{,}47 \pm 0{,}31$ mK/h for low drifts and $1{,}3 \pm 0{,}9$ mK/h for the large drifts, both occuring over several hours. The large frequency change of 3,3 kHz around day 5-6 would correspond to a temperature change of 36 ± 24 mK over 35 hours. The temperature controller chip is classified with a temperature stability of 2 mK.

Together with the qualitatively observed sensitivity of the resistance signal cables to the environment, this hints towards an insufficient performance of the overall temperature regulation. The implementation of the re-built version of the home-made temperature controller will improve the temperature stability, having a better stability performance and reducing the effect of (lengthy) signal cables and a soldered connection to the controller board as in the temporary solution currently is use. However, the overall temperature stability of the vacuum system during the spectroscopy measurements, shown in Figure 14, does not indicate a continuous, slow drift.

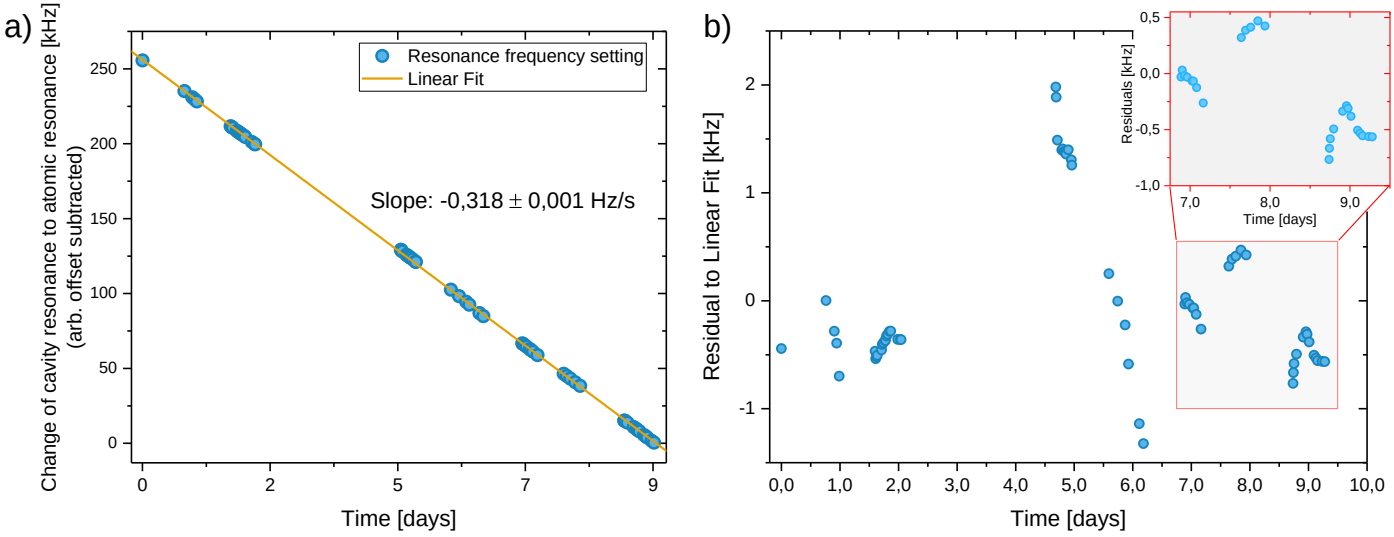

Figure 29: Drift of the cavity resonance with respect to the atomic resonance observed over nine days of spectroscopy measurements, starting on 7th of September 2016 at 9 pm. a) shows the frequency change along with a linear fit with a slope of -318 ± 1 mHz/s. The residuals to the fit are displayed in b), ranging over 3,3 kHz on days with large deviations (days 5-6) and within 250-500 Hz on days with small deviations (inset). The residuals show linear drifts (i.e. deviations from the long-term drift in a)) ranging from 5 mHz/s up to 33 mHz/s (absolute values). Figure 14 shows the temperature of the outer vacuum chamber in this period.

External influences onto the cavity temperature can arise form temperature gradients on the heat shields and fluctuating environment temperature of the vacuum system. Temperature gradients result from the Peltier element attached to the bottom of the outer heat shield and are more pronounced for operation temperatures far away from room temperature. Changes of such gradients reproduced on the cavity cause unwanted frequency drifts. We partly account for this effect by regulating with an average temperature reading from two thermistors at top and bottom outer heat shield. Having a passive heat shield around the cavity is expected to further reduce the effect of temperature gradients and fluctuations, as the heat transfer within each shield is significantly faster than between the shields.

Stabilizing the temperature of the enclosing vacuum system would further reduce influences from the environment and from the waste heat of the Peltier element. The temperature difference between vacuum chamber and outer heat shield could be reduced, further reducing the influence of environment temperature changes.

Fluctuations of the laser power impinging on and coupled into the cavity can cause (fast) frequency shifts. We regularly check and adjust the beam mode match to the cavity via remote controlled mirrors. The beam intensity stabilisation regulates the transmitted beam power. The difference in frequency stability compared to regulating the power based on the incoming beam was not explicitly measured in this setup.

3.8 Future improvement approaches

Along the detailed analysis of the clock laser system, I identified several improvement approaches for future revisions of the clock laser system. First, I present realizable setup modifications in the clock laser system itself and in its integration in the experiment and show how these can improve future experiments. Following that, I point out monitoring and stabilization ideas for clock laser frequency drift on extended timescales. Finally, I give approaches for improved characterization measurements of the clock laser system, as partly mentioned in previous chapters' outlooks.

Regarding the **clock laser and PDH frequency stabilisation setup**, I suggest the following improvements in future setup revisions:

Frequency noise cancellation in the PDH setup

A significant part of frequency fluctuations of the clock laser beams observed in the cavity 1 - cavity 2 beat measurements may result from a missing frequency noise cancelling (FNC) phase stabilisation of the beams towards each cavity. The PDH setup stabilizes the frequency of the beam in front of the cavity with respect to the cavity resonance frequency. However, this adds all frequency noise occurring in the beam path between fast PDH feedback AOM and cavity onto the beam towards the experiment, which is split off right after the fast AOM. Optical fibres, present in the fibre link to the cavity's breadboard and at the fibre coupled EOM, are susceptible to mechanical vibrations which introduces phase/frequency noise. Vibrations at other optical components on the path from the laser to the cavity introduce additional phase noise. In the current setup, we rely on the fibre link having a short fibre, limiting its susceptibility to vibrations, on the fibre-EOM being located on the cavity's vibration isolation platform within the acoustic isolation box, and on all optical components being thoroughly fixed to the breadboards.

A first improvement step would be a fibre noise cancellation (FNC) setup [94,95] for the fibre link between the laser and the breadboard of the cavity and PDH system (which is mounted on a vibration isolation platform). On the laser side of the setup this requires a single-pass AOM for frequency regulation and a Michelson interferometer formed by a local reflection and a reflection from the end facet of the fibre.

The ambitious realization of an FNC implementation is to include the fibre-EOM (located briefly after the fibre link outcoupler on the vibration isolation platform) into the FNC-stabilized beam path. One needs to evaluate in detail whether a useful beat signal can be obtained regarding a low reflected beam power after several fibres and beam splitting optics. Also, the influence of the modulation sidebands which are created in the reverse EOM passage from the modulation sidebands of the first EOM passage and now superimpose at the initial carrier frequency, onto the FNC signal needs to be checked experimentally.

Sebastian Häfner [79] describes an extensive FNC stabilisation solution which covers the whole optical path of the PDH system: For a FNC correction signal of the PDH beam path, they beat the cavity transmission beam with an additional, "local oscillator" beam which is

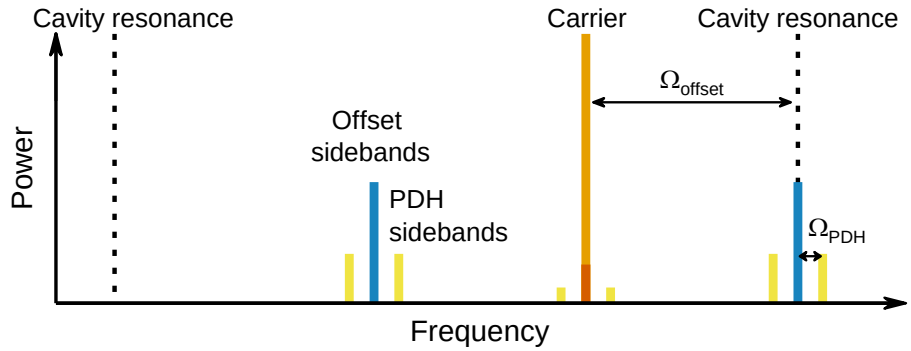

Figure 30: Schematic of a double sideband modulation scheme with a waveguide-based EOM for PDH locking with a frequency offset. The laser (carrier) frequency is close to the atom resonance, a large modulation frequency ($\Omega_{\mathrm{offset}} > 100$ MHz) creates offset sidebands (blue) of which one matches with a cavity resonance. The second modulation at lower frequency ($\Omega_{\mathrm{PDH}} < 50$ MHz) creates additional sidebands (yellow) required for the PDH lock to the cavity. The dark red bar at the carrier frequency indicates carrier amplitude remaining after modulation in the EOM, the carrier amplitude at the experiment is independent of the PDH system. The offset frequency is tuned to shift the clock laser carrier frequency with respect to the atom resonance, to forward a drift compensation and to apply frequency sweeps.

separately fibre guided to the location of the cavity transmission and independently FNC stabilized. The correction signal of the PDH system's FNC beat is fed back to a double-pass AOM before the fibre link to the PDH setup. Frequency fluctuations caused by the fibre-link to the cavity or components in the PDH setup are detected in the cavity transmission beat and corrected by that AOM. Häfner shows that this FNC setup improves the laser stability on timescales starting from 10^{-2} s [79].

A double frequency modulation scheme at the waveguide-based EOM

The waveguide-based EOM requiring a low modulation voltage and operating with modulation frequencies up to several Gigahertz [85,86] enables a double frequency modulation scheme at the EOM [62] for a variable frequency offset in addition to PDH sideband modulation. This is in contrast to bridging frequency offsets with a separate AOM in the current setup.

Figure 30 schematically depicts such a double frequency modulation: A large modulation frequency creates 'offset sidebands' bridging the frequency offset between the laser frequency running close to the atomic resonance and a suitable cavity resonance frequency. The second, significantly lower modulation frequency creates sidebands required for the PDH lock to the cavity (without crossing other carrier or sideband frequencies). The offset frequency is tuned to lock one 'offset sideband' to the cavity while the central laser frequency for experiments remains close to the atomic resonance.

The double frequency modulation scheme allows for frequency sweeps effectively only limited by the regulation bandwidth of the PDH lock. Furthermore, in contrast to an offset-bridging AOM, the EOM can cover large changes in the offset frequency over hundreds of MHz without significant losses in its modulation efficiency. The AOM currently bridging the offset in the cavity stabilisation setup will remain necessary for its other function of intensity stabilisation and possibly as part of an elaborate FNC stabilisation solution mentioned above.

Extracting the RAM signal for feedback on the EOM temperature

So far, we used the RAM monitoring photodetector only for monitoring purposes and in combination with a spectrum analyser. Ideally, we want to realize an active feedback of the RAM signal onto the EOM temperature for a low-frequency RAM stabilisation. To extract the weak RAM signal from the photodetector with sufficient SNR for an analog regulation loop, we need a narrow frequency bandpass at the modulation frequency. The RAM photodetector has a large bandwidth, a large noise effective power and limited amplification. First approximations show that we need a bandpass with bandwidth on the order of 10 kHz at the centre frequency of 18 MHz, corresponding to a filter with large quality factor of 1800, to achieve a minimal signal to noise ratio of a few SNR. Commercially available quartz crystal filters offer quality factors of 10000 and higher and can be implemented in a printed circuit board. With such crystal filters, a simple RAM feedback mechanism can be realized and the effect onto the laser stability evaluated.

At the **clock laser integration in the experiment**, I recommend two significant improvements: A beam power stabilisation at the experiment and a revision of the FNC and clock beam pulse-switching setup.

Stabilisation of clock beam power at the experiment

Currently, the clock beam power at the atoms is not controlled by a feedback loop. A stable beam power of the clock laser, P_{clock}, is relevant in coherent spectroscopy measurements as the Rabi frequency Ω_{Rabi} and therefore the pulse duration $T_{\pi-Pulse}$ covering a pulse area of $1 \cdot \pi$ scale with the spectroscopy beam's power, P_{clock}.

$$T_{\pi-Pulse} = \pi/\Omega_{\mathrm{Rabi}} \propto 1/(2 \cdot \sqrt{P_{clock}}) \tag{3.24}$$

The reduction of relative power fluctuations from about ±10% in the unregulated case down to ≈0,2% with power stabilisation will improve relative fluctuations of the optimal pulse duration from about ±5% down to ≈0,1%. The Fourier-limited FWHM of the sinc² excitation curve for Rabi $1{\cdot}\pi$ pulses relates to the pulse duration by Δ_{FWHM} [Hz] $\approx 0{,}886/(T_{Pulse}$ [s]). Thus, we expect that Rabi oscillations and excitation spectra recorded with beam power stabilisation at the experiment will more clearly follow a certain sinc² curve and show less deviations.

We can realize a beam power stabilisation of the clock beam close to the atoms with an intensity monitoring photodiode on the experiment table after the fibre link. Figure 31 schematically shows a setup arrangement. The feedback can be applied to the AOM on the laser table used for beam switching and FNC regulation ("AOM 3").

Improved FNC setup between laser table and experiment

We use one AOM ('AOM 3' in the Figures 3 and 6) on the laser table to switch the clock beam at the experiment and to enact the FNC stabilisation between laser table and retro-reflector at the experiment. This creates two problems in an experimental cycle: First, after the beam is switched on, the FNC stabilisation first needs to enable its lock which causes the clock beam

frequency at the experiment to perform a short frequency sweep [79]. Second, the FNC regulation electronics requires a reflected power of ≈1 µW for the beat note. If the FNC does not find its lock properly, the clock laser frequency at the experiment is broadened and shifted uncontrolledly. This prevents us from adapting RF power at ‘AOM 3’ to reduce the clock beam power at the atoms to the nanowatt levels needed for high resolution spectroscopy. Modifying the FNC setup on the laser table, as shown in Figure 31, may solve these issues:

The idea is to pick up the back-reflected beam at the FNC AOM (‘AOM 3’) with an isolator, replacing the polarizing beam splitter currently used. The isolator allows to work with a defined, linear beam polarization after the fibre link on the experiment table, which is a crucial improvement. In contrast, picking up the back-reflected beam with an PBS in the current configuration requires the reflected beam polarization to be rotated by $2 \cdot 45°$ in the fibre. This results in working with a circularly polarized beam after the fibre link on the experiment table. The circular polarization prevents an additional AOM (‘AOM 6’) present on the experiment table to work optimally and reproducibly as required for switching operation. Thus, ‘AOM 6’ is only used at fixed power and fixed frequency in spectroscopy measurements. A defined, linear polarization would enable an optimal, reproducible switching operation and power reduction with ‘AOM 6’ on the experiment table. By not using ‘AOM 3’ for switching, the FNC can operate always in locked state, avoiding frequency sweeps and possible locking instabilities.

Using a digital FNC controller can further avoid frequency walk-offs of the phase stabilisation and faster locking. The effects of the sketched updated setup with “always-on” FNC and switching by the AOM on the experiment table need to be checked in detail. Possible issues appearing are beam position fluctuations at the atoms resulting from the AOM switching operation. Also, an effect of a varying reflected beam power, which changes in switching operation, onto the current FNC controller needs to be evaluated.

Alternatively to switching pulses with the AOM at the experiment, a carefully adjusted FNC controller optimized for FNC and switching operation is described in [79].

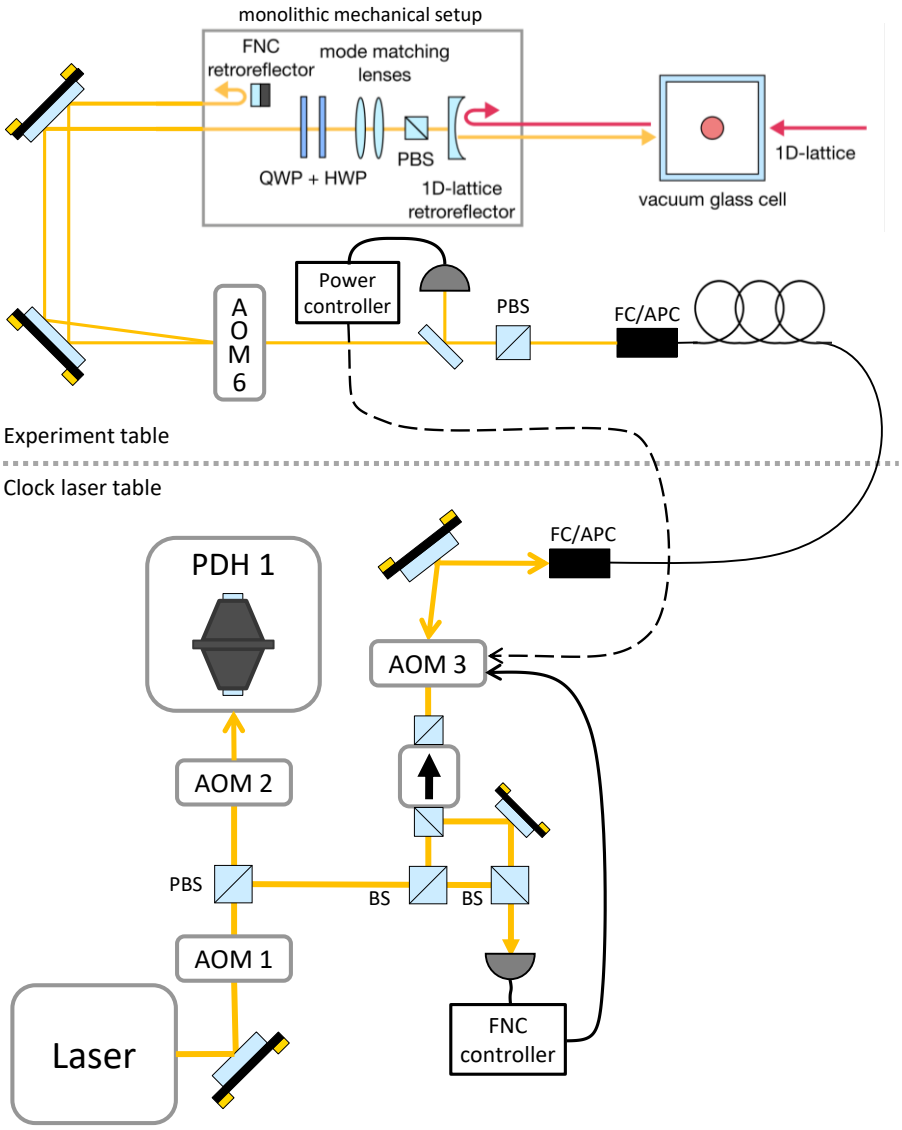

Figure 31: Simplified scheme showing suggested improvements in the clock setup and at the experiment. One change to the current setup is the isolator before 'AOM 3', which enables a linear polarization of the beam exiting the collimator on the experiment table. This allows to use 'AOM 6' to switch pulses at the experiment and leave the fibre link and FNC always in operation. Another setup improvement is an intensity stabilization loop for the clock beam at the experiment. Incorporates Figure 3 which is adapted from [54].

Next, I discuss **improvement approaches involving a frequency reference**, such as a frequency comb or an optical reference signal.

Monitoring the cavity's drift against a frequency comb, a similar cavity, or an optical reference signal

A monitoring of the general drift of cavity 1 could help to identify time windows of approximately linear drift of the cavity. In the following paragraphs I will compare required and available resolutions and timescales. Then I will check if including the second cavity might help for monitoring the drift of the cavity 1 stabilized laser. Last, I point out how a modern frequency comb with narrow-linewidth comb teeth or an optical frequency reference signal could help monitoring drifts and serve for laser frequency stabilization in the experiment.

In first approach, we can (live) **monitor the beat of cavity 1 with the frequency comb**. The comparison of the cavity drift against the atoms in section 3.7.2 indicates the required precision: On top of a long-time linear drift of about 0,32 Hz/s (1,1 kHz/h) we observed peak-to-peak deviations of 250-500 Hz within 6 hours on days with low drift up to ≈750 Hz within 6 hours on days with large drift.

The stability of the frequency comb is limited by the GPS receiver, achieving a relative Allan deviation of $2{,}5 \cdot 10^{-12}$ specified for time scales of $\tau = 30..2000\,\mathrm{s}$. This corresponds to a spectroscopic resolution of 1,3 kHz for the 578 nm clock beam. Taking the observed long-term drift of cavity 1, it takes the laser about 1,1 hours to shift by one resolution width.

When monitoring the beat between the cavity 1 stabilized beam and the frequency comb, it should be possible to detect frequency deviations on the order of 300 Hz after subtracting the linear drift from the data. Such a monitoring can give useful supporting information on the stability of the clock laser when conducting spectroscopy experiments. Of course, information on frequency shifts and drift compensation of the clock laser applied via the experiment control need to be incorporated into the clock-comb beat frequency data collected by the frequency counter of the frequency comb. A simple script could then process the data and live plot the current drift deviations of the clock laser.

Unfortunately, due to a malfunctioning part in the comb, fast fluctuations of the comb's frequency broaden the beat to 140 kHz (full width at 90% level of a Gaussian fit) within a few seconds of averaging. Such a large frequency interval renders the comb not suitable for monitoring of usual linear drifts and deviations of the beat frequency on timescales below several hours.

Long term, simultaneous **drift measurements of the cavity 1 and cavity 2 stabilized beams against the comb** could verify the individual long-term drifts and oscillations of each cavity on timescales of hours and longer. Allan deviations determined from that data will still be limited by the large instability of the comb. It will likely be possible to remove some of the comb's large fluctuations assuming that these correlate in the two beat frequency data sets. However, the resulting data will not exceed the optimal resolution and stability of the comb limited to the kHz frequency scale. Yet, the simultaneous beat measurement would show

differences in the intermediate- and long-term frequency stability of the new all-ULE cavity 1 and cavity 2 consisting of ULE spacer and FS mirrors.

A **second cavity system with similar long-term stability as the rebuilt cavity 1 system** would enable to continuously and live monitor the beat and therefore the combined drift of the two cavity systems on a scale relevant to the spectroscopy measurements. This beat monitor would enable to live identify significant changes in the combined drift of the cavity systems. In combination with few atom spectroscopy data points giving the frequency detuning of the cavity 1 system to the atom resonance, the live beat monitor could help to identify and predict time frames of linear drift of the cavity 1 system. This could be useful to identify laser drifts occurring during spectroscopy measurement series with high resolution and extended duration.

Modern, commercially available, narrow-linewidth frequency combs show stability levels ranging from 10^{-15} down to 10^{-16} in 1 s averaging time, corresponding to comb teeth linewidths below 50 Hz down to single Hz. Such a comb would enable several applications: First, one could live monitor the drift behaviour of the clock laser stabilised to each cavity. The live monitoring would inform us on nonlinear drifting behaviour of cavity 1 while recording measurement series, which could be compensated retrospectively. Furthermore, it would enable us to identify existing error sources acting on the laser stability in the laser systems. Second, narrow comb teeth would enable to set up a phase lock between the cavity stabilised clock laser system and the frequency comb. Ideally, the phase lock could compensate drifting behaviour of the clock laser on timescales of $\gtrsim$10 s, in which we observe uncontrolled clock laser frequency fluctuations, and therefore provide the phase stability of the comb as upper stability limit for the clock laser. If the comb offers sufficient operational stability in the laboratory environment, sufficient output power on the relevant frequencies and sufficient frequency stability, one could use phase locks to such a comb for frequency stabilization of most laser systems in the experiment. This might simplify several laser locking schemes in our setup.

Another approach to obtain a high long-term stability is to use an **optical frequency reference** signal. Such an optical frequency reference signal would be transmitted via optical fibre link from an atomic clock in a metrology laboratory. The Florence group recently used the increased long-term stability of such a referenced clock laser to measure the ^{173}Yb clock transition with unprecedented accuracy, exceeding the GPS limit by factor 20 [67,68].

Last, I (re-)state **improved characterization measurements** and improved **operational parameters** of the clock laser system, as also mentioned in previous sections.

Verification of the intensity stabilisation configuration
For optimal operation of the clock laser, it will be useful to verify the configuration and settings of the intensity stabilisation in the finalised clock 1 setup, as discussed ending chapter 3.5. One can do this by repeating intensity noise measurements for the two intensity stabilisation configurations (using the photodiode before or after the cavity for regulation) and optimizing the intensity controller's operation parameters. A direct comparison of the achievable frequency stability or spectral resolution with the two configurations could reveal an influence of the different intensity stability levels of the clock setup.

Improved measurements of the cavity's sensitivity to beam power fluctuations and of the PDH error signal slope
In the characterization measurements for the cavity 1 and the PDH lock presented in sections 3.3.4 and 3.4.2, such as the cavity's frequency sensitivity to the intracavity beam power, the PDH photodiode's offset voltage sensitivity to the beam power and the PDH error signal slope on resonance, I had to rely on a statistical analysis of subsequently recorded data. Due to large laser frequency fluctuations, this resulted in large relative errors in the extracted properties. To reduce the large uncertainty in the results, I suggest measuring these frequency sensitivities to beam power modulations while simultaneously monitoring the beat frequency and PDH offset voltages (PDH photodiode signal amplitudes at modulation frequency) of both PDH locks. On this way, the modulation applied can be correlated better to observed frequency changes. Combined with an analogously improved measurement of the PDH error signal slope on resonance, by varying the PDH offset voltage with simultaneous recording of the beat frequency and PDH offset voltages, the resulting characterisation values for cavity and PDH system will be far more precise.

Setting the cavity temperature closer to the CTE-ZC temperature
Setting up an improved temperature controller for cavity 1 will require a new temperature scan to ensure operation close to the cavity's zero-crossing temperature of thermal expansion. This allows to match the CTE-ZC temperature even closer as currently adjusted, achieving an even smaller temperature sensitivity of the cavity's resonance frequency.

Finally, one could verify **general characteristics of the setup** that were not specifically re-evaluated for this thesis, such as a Bode plot showing the noise characteristic of the clock laser system in PDH lock.

Chapter 4 Spectroscopy on the clock transition

In this chapter, I present experimental results giving high-resolution spectra and showing effects of many-body physics with ultracold ^{173}Yb atoms in our setup. André Kochanke and I conducted and evaluated these atom spectroscopy measurements in autumn and winter 2016. Making these observations with our experiment was a long-term goal we aimed to achieve with the improvements at the clock laser setup presented in this thesis, and with the multitude of improvements realized at the experiment over the past years. Furthermore, these measurements finally relate our laboratory work to modern experimental physics with ultracold atoms.

First, I discuss the atom preparation for spectroscopy measurements on single- and two-component spin mixtures of ultracold ^{173}Yb in a magic wavelength optical lattice. I present single spin-component high-resolution spectra determining the achievable resolution of the clock laser system. As scanning the full frequency span between expected features in multi-component spectra with applied magnetic field can take one to two hours, it requires a good long-term stability of our experiment and the clock laser system in particular. The high-resolution spectra indicate if the stability of the clock laser will suffice to record clean multi-component spectra and to resolve interaction features therein. Next, I show an optical sideband spectroscopy measurement with a single spin-component gas which characterises our optical lattice.

The last part of this chapter turns to two-component spin mixtures. With focus on our experiment, I give a brief theoretical description of the emergence of spin-exchange interactions between atoms with SU(N) interaction symmetry in a two-orbital system. Next, I present a spectroscopy measurement showing a feature resulting from spin-exchange interactions, thereby proving the system's capability to investigate many-body physics with ^{173}Yb. I then give a brief outlook on complementary measurements investigating the SU(N) symmetry and interaction effects in Yb that are possible to measure with the current system.

4.1 Preparation of ultra-cold atoms in an optical lattice for spectroscopy

In Chapter 2, I gave an overview of the experimental apparatus. Here I give details on the preparation of ultra-cold atoms with one and two spin-components for our spectroscopy measurements, starting from the cold atom gas in the optical dipole trap. In general, we can prepare quantum degenerate ^{173}Yb Fermi gases of up to 10^5 atoms at temperatures of $20\% - 27\%\ T_F$, with atom number and temperature depending on the spin-mixture. Overall, an experimental cycle with an ultra-cold atom Fermi takes about 50 s.

Spin preparation
We populate desired spins by using sigma-polarised light at the 556 nm transition to resonantly pump the cold atoms held in the dipole trap, just before evaporation to ultra-cold temperatures.

For single spin-component spectroscopy measurements of ultracold atoms in a magic lattice, we prepare cold ^{173}Yb atoms in the $m_F = +5/2$ spin state. Working with a single component ("spin-polarized") gas and low atom numbers avoids interaction-induced shifts or broadening of the clock transition. Spin-polarized samples require a small occupation of other spin states for sympathetic cooling during evaporation. We estimate about 5% of the atoms remaining in other spin states after evaporation.
For two component spectra, we prepare ^{173}Yb atoms with the spin-components $m_F = \pm 5/2$.

Optical lattice
After evaporation in the optical dipole trap, we transfer the atoms into the optical lattice. We exponentially increase the power of the lattice beams within 100 ms and then switch off the optical dipole trap beams to avoid additional AC-Stark shifts.

The dipole trap for evaporative cooling features a low average trapping frequency of $\overline{\omega} = 36$ Hz and a Fermi energy of $E_F = h \cdot 1{,}99$ kHz. From an idealized 3D lattice model, we expect to be able to load about $2{,}7 \cdot 10^4$ atoms into the lowest lattice band without higher band occupation. We can check the lattice band occupation with Fermions by using the band mapping technique [96]. Band mapping maps the atoms' quasimomenta in the lattice to real momenta. Thereby it images the occupied Brillouin zones of the lattice. Lattice sideband spectroscopy, discussed below, also indicates the lattice band occupation.

The lattice wavelength is set to the magic wavelength of $\lambda_{mag} \approx 759{,}35$ nm [61,62], based on wave meter readings. The wave meter's absolute accuracy of 10 MHz (within ±200 nm of the calibration wavelength) suffices for the envisaged spectroscopy resolution: The sensitivity of the differential stark shift is on the order of $\Delta V_d(\omega_{lat}) = -22\ \mathrm{mHz}/(\mathrm{GHz} \cdot E_r)$, with lattice frequency ω_{lat} and recoil energy $E_r = \hbar k_{lat}/2M$, where k_{lat} is the lattice laser wavenumber and M the atomic mass [61,97]. For a 45 E_r deep lattice this results in a broadening of only 1 Hz at 1 GHz detuning.

The lattice depths are set to 43 E_r for the 1D lattice (determined by optical sideband spectroscopy in the lattice, shown in the next section) and 33 E_r for the 2D lattice (determined by lattice beam intensity modulation [54,98]). At these lattice depths, we operate in the Lamb-Dicke regime for the lowest band excitations of atoms in the lattice. The large lattice depth results in quasimomentum-independent Rabi couplings in essentially flat Bloch bands with bandwidths below the clock laser linewidth. These features of a deep lattice allow us to perform Doppler-free, Fourier limited spectroscopy.

The periodicity of the lattice potential restricts motional excitations of the atoms to the lattice band energies. The different resonances in the lattice are carrier (electronic excitation while remaining in the same lattice band), blue sidebands (excitations with simultaneously increasing lattice band occupation) and red sidebands (electronic excitation while decreasing lattice band occupation). The lattice bands are several kHz apart in a deep lattice, which we resolve in optical sideband spectroscopy measurements. Due to the anharmonicity of the actual optical lattice, higher lattice bands are not evenly spaced. This allows the attribution of excitations in the lattice spectrum. Furthermore, the Lamb-Dicke regime increasingly suppresses lattice band excitations across several bands.

Spectroscopy on the clock transition

We interrogate the ultra-cold ^{173}Yb atoms on the $^1S_0$-$^1P_0$ transition with the 578 nm clock laser. We work with square-shaped pulses in the time domain. The clock laser is superimposed with the 1D lattice and linearly polarized along a magnetic field providing a quantization axis to drive π-transitions of the atom. An external magnetic field of $11{,}6$ G introduces a spin-dependent Zeeman shift, separating the excitation energies of different spin components. The measurements presented in this chapter are coherent spectroscopy measurements operating with a Rabi pulse area of $1{\cdot}\pi$ for the lowest band carrier excitation of the optical lattice.

The Rabi frequency of a transition scales with the square root of laser power and with lattice depth. Furthermore, the Rabi couplings of different band transitions in the lattice differ due to a finite photon momentum. The Rabi coupling is determined by the Frank-Condon factor contained in the transition matrix element. If the clock pulse length is not adapted to cover a $1{\cdot}\pi$ pulse area of the Rabi frequency for each lattice band transition individually, the relative excitation fraction of a mismatched transition decreases. Analogously, the pulse length and clock laser power must be adapted to experimental conditions, such as the 1D lattice depth, to achieve a maximal excitation fraction (see also equation (3.24)).

When recording a spectrum, the clock laser frequency is shifted sequentially between each experimental cycle. Additionally, we feed-forward a linear drift correction to the clock laser frequency. We determine the magnitude of linear drift correction from shifts of the carrier resonance frequency, which we determine from subsequently recorded spectra and by additional checks for the resonance frequency in between measurement series.

Imaging

After interrogation with the clock laser pulse, we perform band mapping on the atoms by ramping the lattice down within 1 ms and allowing a brief TOF. Then we perform double imaging of ground and excited state by absorption imaging, using the $^1S_0$-$^1P_1$ transition in combination with the repumper laser. Counting atoms of each state allows to work with relative excitations normalized to the total atom population. Relative excitation ratios cancel out fluctuations in the total atom number of about 15%, which are always present in the experiment. The double imaging scheme enables spectra with better signal to noise ratios than just using the ground state atom number.

4.2 Spectroscopy on spin-polarised ^{173}Yb Fermi gases

4.2.1 High-resolution clock spectroscopy

To determine the achievable resolution with our setup, we performed high-resolution clock spectroscopy on the carrier resonance. We prepared spin-polarized Fermi gases of ^{173}Yb atoms in the $m_F = +5/2$ state. The degenerate Fermi gases consisted of 15000 to 30000 atoms at a temperature of 20% - 25% T_F. By operating with a single spin-component and low atom numbers in a 3D magic-wavelength lattice, we avoid interaction effects in doubly occupied lattice sites or higher lattice bands which could shift or broaden the clock transition. Applying an external magnetic field of 11,6 G shifts the excitation energy proportional to the spin state. Thereby we avoid excitations of other, residual spin components remaining in the sample. In this setting, the linewidths of the absorption spectra are only limited by power broadening or by the clock laser stability. We evaluate relative excitation fractions normalized to the total atom count.

We apply square-shaped pulses covering a Rabi $1{\cdot}\pi$ pulse area for maximum excitation. A square pulse of duration T_{Pulse} gives an excitation spectrum with sinc^2 line shape - corresponding to the squared Fourier transform of a rectangle function - with a Fourier-limited FWHM of Δ_{FWHM} [Hz] $\approx 0{,}886/(T_{Pulse}$ [s]) [99]. This relation shows that we need to increase the clock pulse duration to measure higher resolution spectra (towards smaller FWHM). To still achieve maximum excitation in spectra recorded with longer pulse duration, we need to adapt the Rabi frequency to match the condition of a Rabi $1{\cdot}\pi$ spectroscopy pulse. As the Rabi frequency is proportional to the square root of beam power (shown in equation (3.24)), we decrease the clock beam power at the experiment to work with longer Rabi $1{\cdot}\pi$ pulses.

Figure 32 shows five exemplary spectra, reducing the Rabi frequency with each spectrum from 1900 kHz in a) down to 120 kHz in e). Each spectrum was recorded in a single experimental run. Table 4.1 gives for each spectrum the experimentally set pulse duration T_{Pulse} and beam power P_{clock} along with corresponding Rabi frequency Ω_{Rabi}, the theoretically expected Fourier limited sinc² FWHM and the FWHM of a fitted sinc² curve. The fitted sinc² line shapes follow the spectra of Figure 32 a) -d) well. We observe peak excitation fractions of 82% – 97%.

	T_{Pulse} [ms]	Beam power P_{clock} [µW]	Ω_{Rabi} [Hz]	Theory sinc² FWHM [Hz]	Fitted sinc² FWHM [Hz]
a)	1,65	103	1900	539	455 ± 13
b)	3,50	20	900	254	224 ± 8
c)	9,90	3,0	317	90	92 ± 4
d)	18,10	0,95	174	49	50 ± 2
e)	26.50	0,30	120	33	-

Table 4.1: Experimental and fitting parameters for shown single-component spectra: Experimental pulse duration T_{Pulse} and beam power P_{clock}, corresponding, calculated Rabi frequency Ω_{Rabi} and expected sinc² FWHM and FWHM obtained from a sinc² fit for each spectrum.

We also observe that the sinc² fits for the spectra a) and b) undercut the expected Fourier-limited width by 16% and 12%, respectively. The narrowest successfully recorded spectrum has a fitted sinc² linewidth of 50 ± 2 Hz FWHM.

When we tried to further increase the resolution to 34 Hz by operating with a pulse time of 26,5 ms, scattered data points at and around the resonance replaced the clean excitation curves observed in the previous spectra. Figure 32 e) shows such a measurement. The scatter shows multiple peaks in contrast to a homogenously broadened excitation. Overlaying the fitted sinc² curve of the measurement in d) with the scattered points shows that the excitations occur over a similar frequency range as for the 50 Hz linewidth spectrum. These observations indicate that distorting frequency noise can be assumed to be on Fourier frequencies above the inverse of the experimental cycle time of about 53 s, i.e. ≳10 mHz, but below the inverse of the pulse time of T_{Pulse}= 26,5 ms, i.e. ≲40 Hz [53]. **The resolution at which these fluctuations occur fits to the magnitude of the clock laser frequency fluctuations observed in the beat with the second cavity**, shown in Figure 27, respectively chapter 3.7.1.

In the following, I discuss several potential error sources and possible tests: Large frequency drifts of the cavity causing a deformation of spectra's linewidth; non-optimal pulse duration settings; a verification of correct linear drift compensation of the cavity and experimental problems when working with low clock beam powers.

Looking at the frequency shifts of the atomic resonance, we can check if a large **drift of the cavity** could have caused a narrowing of these spectra. Spectrum a) was recorded on a day with high deviation from the linear long-time cavity drift (at time 0,94 days in Figure 29). However, the linear deviation from the cavity's overall linear drift accounts only to a small degree for the difference in width. Similarly, we cannot explain the deviation of spectrum b) solely by the clock laser's non-linear drift behaviour.

Another error source might be **non-optimal pulse duration** settings overestimating the Fourier-limited width. Incoherent spectroscopy spectra recorded with clock pulse areas of a few π give narrower and lower central excitation peaks with increased side-peak amplitudes compared to a coherent spectroscopy spectrum recorded with Rabi 1·π pulses. However, the

central peaks show high peak extinction ratios which therefore does not hint towards this error source.

Recording subsequent spectra in alternating directions of the clock laser detuning sequence, i.e. recording once with steps of increasing detuning versus steps of decreasing detuning, allows to **identify a non-optimal drift compensation** as the widths of the two spectra would differ. We did this for the narrowest successful spectrum, shown in Figure 32 d), verifying in several measurements that the spectra's widths were not narrowed or broadened by a non-optimal drift compensation.

Experimental problems occurred when we needed to reduce the clock beam power at the experiment below 1 µW, such as to 300 nW for spectrum attempt e):
Once, the **fibre noise cancellation** (FNC) towards the experiment table requires about 1 µW beam power in the beat to reliably lock the laser frequency at the beginning of each pulse. Changing the FNC setup as discussed in section 3.8, that is introducing an isolator to split off the reflected beam, addresses these problems. Furthermore, frequency walk-offs and sweeps due to the FNC jumping into lock can be reduced with a digital FNC controller or minimised with an optimised controller configuration [79].
Inserting **neutral density filters and aligning polarizing beam splitters to low transmission** to reduce the laser power at the experiment can distort the beam profile and change the beam position at the atoms. An uneven illumination of atoms causes a varying Rabi frequency across the sample, limiting the achievable excitation. It needs to be checked if this is already the cause for the slightly lower excitation ratio in spectrum d).

Furthermore, a currently **missing intensity stabilisation** of the clock beam at the experiment is undoubtedly unfavourable. Relative power fluctuations of about ±10% cause ±5% error in Rabi frequency, as discussed in chapter 3.8.

In course of these single component spectroscopy measurements, we obtained the data on the drift of the cavity resonance with respect to the atomic resonance shown in section 3.7.2 and Figure 29.

The achieved, high spectroscopic resolution of 50 Hz along with clean excitation curves in the spectra show a significant improvement compared to the spectroscopy results measured with the initial setup at the beginning of my PhD. With the many improvements realized at the clock laser system and at the overall experiment taking effect, we expect to observe and resolve spin-exchange interaction features in two-component spectra.

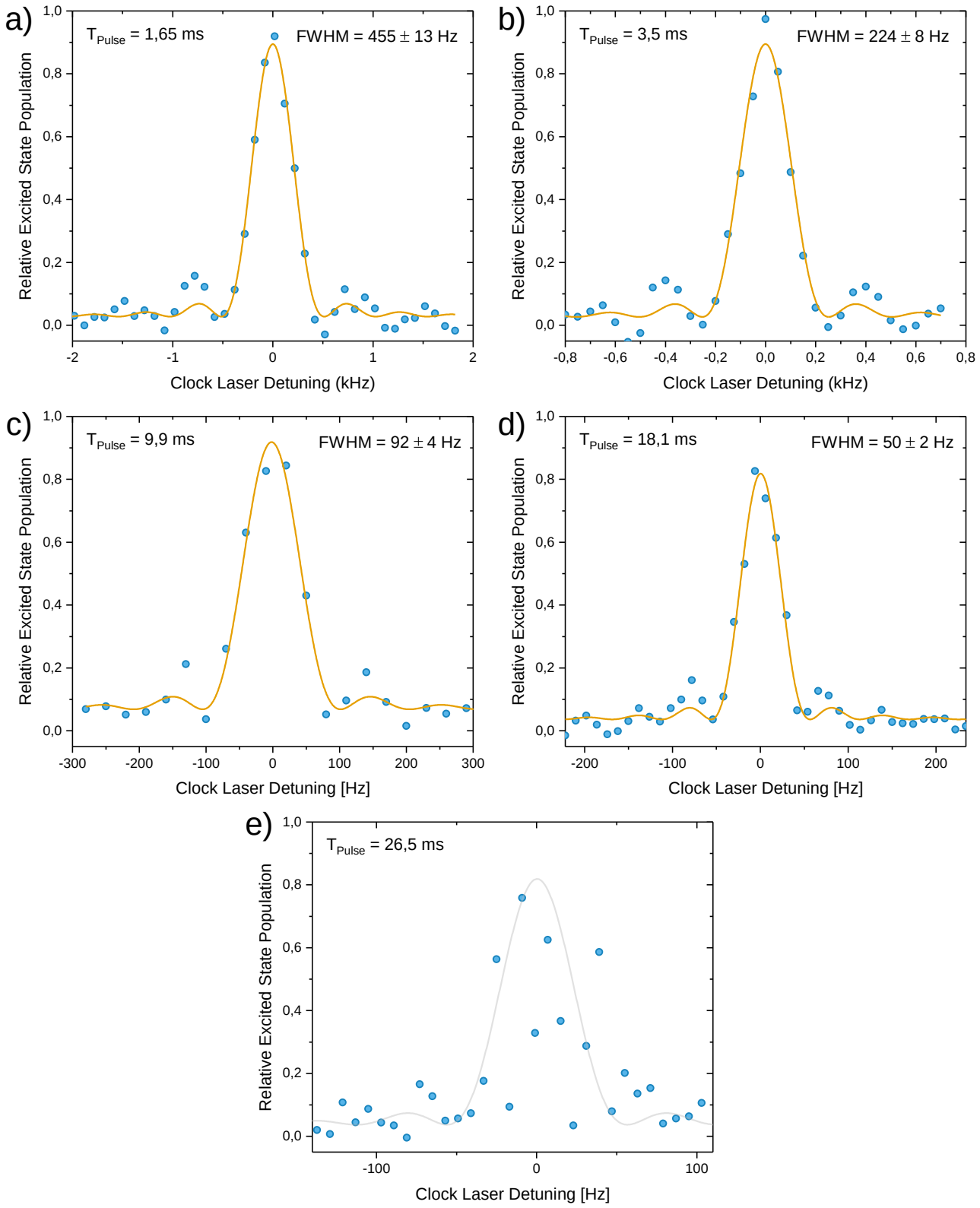

Figure 32: High-resolution clock spectroscopy measurements on ultra-cold gases of spin-polarised ^{173}Yb in an optical lattice. The plots show the relative excited state population, normalized to the total atom count. All spectra show single experimental runs, with clock laser pulses at Rabi $1{\cdot}\pi$ pulse duration. We observe excitation ratios of 82-97%. Sinc² curves (solid orange lines) expected from theory fit well to spectra a)-d). However, spectra a) and b) undercut the Fourier-limited FWHM by over 12%. We successfully recorded spectra down to a Fourier-limited resolution of 50 Hz FWHM. Attempting to access a higher resolution in spectrum e) (with overlay of sinc² fit of spectrum d) in gray), shows multiple excitations scattered over a similar width as for the 50 Hz spectrum. This indicates that low-frequency noise limits a higher spectroscopy resolution.

4.2.2 Optical sideband spectroscopy

To characterise our lattice, we measured a spectrum of spin polarised ^{173}Yb loaded into the lattice over a large frequency range covering carrier and sideband excitations. For this measurement, we prepared degenerate Fermi gases of about 35000 atoms in the $m_F = +5/2$ spin-state at a temperature of $(26 \pm 1)\%\ T_F$. For the 578 nm clock pulse we used a power of 5 mW and 220 µs pulse duration, corresponding to a Rabi-1·π-pulse for the carrier transition at Rabi frequency of $\Omega = 2\pi \cdot 2{,}3$ kHz. The expected Fourier-limited resolution is 4,0 kHz FWHM for the carrier transition.

Figure 33 shows the relative excited state atom population over a frequency range of 80 kHz. Two excitations showing the carrier and first blue sideband resonances are visible. We see no features at the frequencies of the first red or second blue sideband. We locally fitted Lorentz functions to the excitation peaks. The fitted carrier FWHM of $4{,}1 \pm 0{,}4$ kHz matches to the expected Fourier-limited resolution. The frequency spacing between the carrier and first blue sideband is $23{,}8 \pm 0{,}2$ kHz, which corresponds to a lattice depth of $43\ E_r$ for the 1D lattice. This lattice depth is well in the regime required for Fourier-limited spectroscopy measurements in the lowest lattice bands. We observe no excitation at the frequency detuning of the red sideband. We also observe no excitation at the detuning of the second blue sideband. This was expected for no-significant population present in the first lattice band when working in the Lamb-Dicke regime. Furthermore, the relative Rabi frequency is highly reduced for that transition in a deep lattice, resulting to be on the background noise level of the spectrum. This measurement shows the clean preparation and loading of several 10^4 atoms into the lowest band of the deep, magic-wavelength optical lattice.

The fitted amplitude of the first blue sideband is about 64% of that of the carrier. This ratio coincides very well with the relative reduction in coupling strength of 62% which we expected due to different the Rabi couplings for the two transitions.

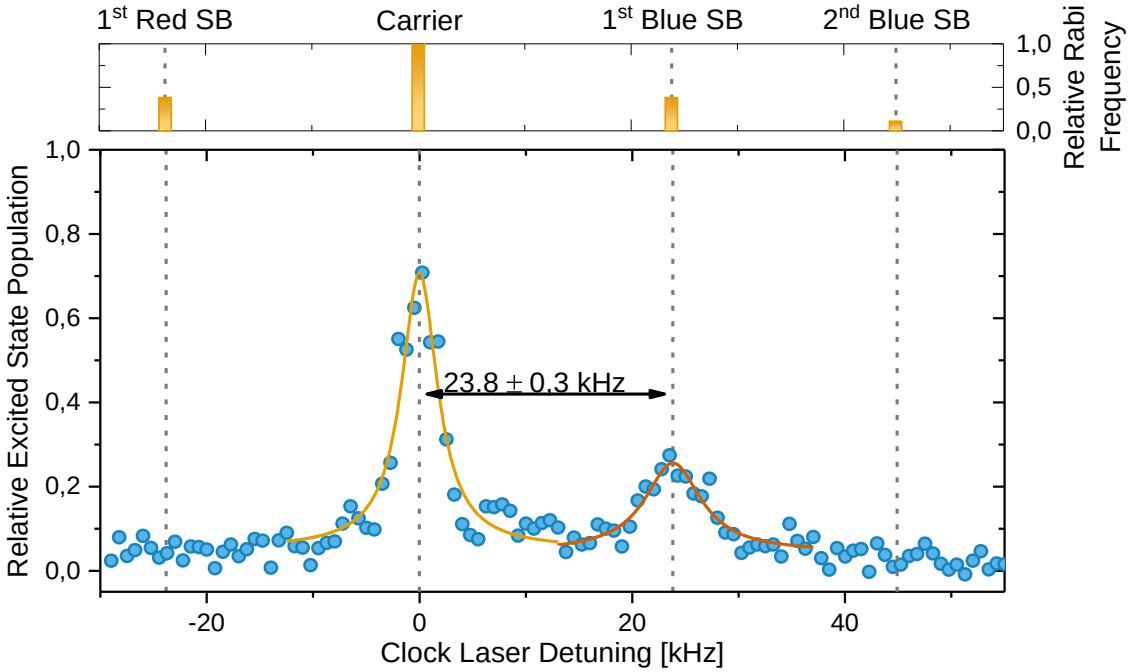

Figure 33: Clock spectroscopy of spin-polarized ^{173}Yb in a three-dimensional optical lattice, covering several lattice band excitations. The spectrum shows the relative excited state atom population against the frequency detuning of the clock laser. The samples consisted of ≈3,5·10^4 atoms in the $m_F = +5/2$ spin state at 26% T_F. The lattice depths were 43 E_R in the 1D lattice and 33 E_R in the 2D lattice. The clock pulse length was fixed to 220 µs, corresponding to a $1{\cdot}\pi$ – pulse of the carrier transition. The spectrum shows two excitation peaks to which we associate carrier and first blue sideband excitations of the lattice. Locally fitted Lorentz functions give a frequency distance between the fit centres of 23,8 ± 0,3 kHz, resulting in the 1D lattice depth of 43 E_R. We observe no other excitations in the spectrum. No excitation at the clock laser detuning of the first red sideband indicates an insignificant occupation of higher lattice bands. The top graph shows calculated relative Rabi frequencies of the lattice transitions relative to the carrier excitation transition. The amplitude ratio of first blue sideband to carrier of 64% coincides well with the relative Rabi frequency ratio.

4.3 Two-particle interactions with spin- and electronic degree of freedom

In the previous sections we verified a clean atom preparation of ultracold ^{173}Yb atoms in the optical lattice and measured single atom clock excitation spectra with 50 Hz resolution. We now turn towards a long-standing aim of this project, to observe and analyse quantum many-body physics in two-orbital ^{173}Yb. I begin with a brief theory summary, describing two Fermionic particles with SU(N) symmetry and with spin- and electronic degree of freedom in a deep optical lattice. Next, I present our spectroscopy results and discuss the observed spin-exchange interaction feature. In view of this first successful result with our experiment, section 4.4 then gives an outlook on possible further, closely related measurements, orienting on [26,27], which would make use of the experiment's capabilities. André Kochanke and I conducted and evaluated the measurements presented in this chapter.

4.3.1 Theory overview: SU(N) symmetric two-particle interactions in a deep optical lattice

In this section I recapitulate the theory on atomic interactions which are the basis for many-body physics. I show the emergence of spin-exchange interactions in fermionic Ytterbium following detailed explanations given in [53,55,62].

4.3.1.1 Electronic properties of Ytterbium

AE and AEL atoms such as Ytterbium possess favourable electronic properties for an investigation of many-body effects with ultra-cold atom gases: A metastable electronic state and a SU(N) symmetry enable experimental realizations of complex Hamiltonians. In fermionic ^{173}Yb, we can populate up to six different spin components, $m_F = 5/2$ to $+5/2$. For our initial interaction spectroscopy measurements, we used two spin-component mixtures.

The low-lying metastable electronic state $^3P_0$ can be coherently controlled from the ground state $^1S_0$ by the ultra-narrow clock transition. This opens an 'orbital' degree of freedom and complementing a spin degree of freedom in fermionic Ytterbium.

The nuclear spin I and the electronic angular momentum J are highly decoupled in the electronic states $^1S_0$ and $^3P_0$. For the $^3P_0$ state, this results from a vanishing hyperfine interaction in first order, which strongly decouples its nuclear spin from the electron cloud. Furthermore, in the fermionic ^{173}Yb, solely the nuclear spin (I) determines the spin degree of freedom in these two electronic states, as each state has zero electronic angular momentum ($J = 0$).

An SU(N) symmetry in two-body collisional interactions of Fermions arises from the decoupling of nuclear spin and electronic angular momentum. Short-range two-body collisional interactions become effectively spin-independent when no angular momentum is present. Furthermore, the individual spin-projection m_F of each Fermion is preserved in atomic collisions, which reduces available scattering channels to only one for each electronic state combination. This simplifies possible collisional interactions between Fermions with spin-degree of freedom. This allows to tailor systems with SU($N = 1 \ldots 6$) symmetry, depending on the number of spin states N.

In this analysis, I regard two-particle interactions. From four possible single particle states, six two-particle states emerge which are allowed by the Pauli principle. Regarding two electronic states, termed $|g\rangle$ and $|e\rangle$, and two spin states, $|\uparrow\rangle$ and $|\downarrow\rangle$, the two-particle states in the atomic interaction basis Hilbert subspace are:

$$|gg\rangle|\uparrow\downarrow\rangle^-,\ |eg\rangle^+|\uparrow\downarrow\rangle^-,\ |eg\rangle^-|\uparrow\uparrow\rangle,\ |eg\rangle^-|\uparrow\downarrow\rangle^+,\ |eg\rangle^-|\downarrow\downarrow\rangle,\ |ee\rangle|\uparrow\downarrow\rangle^- \qquad (4.1)$$

Here, + and – indicate the symmetric and anti-symmetric superpositions in the electronic states and in the spin states, respectively.

$$|eg\rangle^{\pm}|\uparrow\downarrow\rangle^{\mp} = \frac{1}{\sqrt{2}}(|eg\rangle \pm |ge\rangle) \otimes \frac{1}{\sqrt{2}}(|\uparrow\downarrow\rangle \mp |\uparrow\downarrow\rangle) \qquad (4.2)$$

Corresponding to the four different electronic configurations of two-particle states in the SU(N) symmetric system, four scattering channels exist. The inter-orbital two-particle states are coupled by the spin-exchange interaction, shifting their eigen energies as will be shown below.

Investigating interaction-induced many-body effects in bulk ultra-cold atom quantum gas mixtures of several (thousand) atoms is difficult: The kinetic energy is predominant the system and interactions and atom losses in a large population may further inhibit a theoretical or experimental analysis.

4.3.1.2 Interactions in a deep optical lattice and interaction Hamiltonian

By loading a two spin-component Fermi gas into the lowest band of a deep optical lattice, we simplify the many-body system to an array of two-body systems. Tunnelling between the lattice sites must be negligible on experimental timescales to isolate the lattice sites. This is satisfied in the Lamb-Dicke regime of deep optical lattice potentials confining atoms to a space smaller than the clock laser wavelength. For deep lattices, the quasimomentum dispersion relation of the Bloch bands turns essentially flat. The Rabi coupling of the clock laser transition is then quasimomentum-independent and all quasimomenta can be excited equally well, which equals to Doppler-free, Fourier limited spectroscopy resonances.

Interband transitions are increasingly suppressed with increasing lattice depth. Due to an anharmonicity of the optical lattice, its energy levels are not equally spaced. This enables to spectrally resolve individual band transitions.

In a simplified description, a deep optical lattice with flat, narrow Bloch bands can be regarded as a system of many individual lattice sites with the energy levels of a harmonic oscillator. This figurative description of individual lattice sites holds when only the lowest lattice band(s), respectively energy levels of each site, are populated. This allows to describe each lattice site as individual trap with large level spacing $\hbar\nu \gg E_R$, E_R being the recoil energy in the lattice.

The combination of two electronic states and spin degree of freedom in AEA and AEL elements enable two atoms on a lattice site, forming two-particle states which satisfy the Pauli principle. Latter requires the two-particle states to be an anti-symmetric combination of spin- and electronic state. The Hamiltonian of a two-body system with spin- and orbital degrees of freedom can be solved analytically.

The two-orbital SU(*N*) Fermi-Hubbard Hamiltonian, shown in equation (4.3), describes cold fermionic AEL atoms in a single band of an optical lattice [25].

$$\begin{aligned}\hat{H}_{2FH} = &- \sum_{\langle j,i\rangle,\alpha,m} J_\alpha \left(\hat{c}^\dagger_{i\alpha m}\hat{c}_{j\alpha m} + h.c.\right) \\ &+ \sum_{j,\alpha} \frac{U_{\alpha\alpha}}{2}\hat{n}_{j\alpha}\left(\hat{n}_{j\alpha} - 1\right) \\ &+ V\sum_j \hat{n}_{je}\hat{n}_{jg} + V_{ex}\sum_{j,m,m'} \hat{c}^\dagger_{igm}\hat{c}^\dagger_{iem'}\,\hat{c}_{igm'}\hat{c}_{iem}\end{aligned} \tag{4.3}$$

The operator $\hat{c}^\dagger_{j\alpha m}$ creates an atom at lattice site j at position $\boldsymbol{r}_i$ in state $|\alpha m\rangle$, where α=g, e denotes the electronic state and $m = \uparrow,\downarrow$ denotes the spin state. Correspondingly for annihilation operator $\hat{c}_{i\alpha m}$. The number operator for state $|\alpha m\rangle$ in site j is $\hat{n}_{j\alpha m} = \hat{c}^\dagger_{j\alpha m}\hat{c}_{j\alpha m}$, and the sum over all spin states is $\hat{n}_{j\alpha} = \sum_m \hat{n}_{j\alpha m}$.

The first line describes tunnelling between neighbouring lattice sites i, j with tunnelling energies $J_\alpha = J_g, J_e$ for ground and excited state atoms, given in equation (4.4). $\langle i,j\rangle$ denotes the summation over nearest neighbour-lattice sites. In a magic-wavelength optical lattice, ground and excited state potentials are equal as the Wannier functions are equal for both states.

$$J_\alpha = -\int d^3r\, w_\alpha(\boldsymbol{r})\left(-\left(\frac{\hbar^2}{2M}\right)\nabla^2 + V_\alpha(\boldsymbol{r})\right)w_\alpha(\boldsymbol{r} - \boldsymbol{r_0}) \tag{4.4}$$

Here, $w_\alpha(\boldsymbol{r})$ is the Wannier function for the atom in electronic state α at position $\boldsymbol{r}$, M is the atomic mass, V_α the lattice potential and $\boldsymbol{r_0}$ the lattice spacing. When working with deep optical lattices and short experimental time scales compared to the tunnelling time constants, we can neglect tunnelling processes and drop these terms in the following considerations.

The remaining terms describe interactions of two atoms on a lattice site. Elastic collisions shift the energy of two atoms in the same electronic state by U_{gg} and U_{ee}, respectively, given in equation (4.5). Two atoms in different electronic states experience energy shifts by direct interaction V and exchange interaction V_{ex}, given in equation (4.6). They relate to the inter-orbital interactions U_{eg^+} and U_{eg^-} as shown in equation (4.7) and (4.8).

$$U_{\alpha\alpha} = \frac{4\pi\hbar^2}{M}a_{\alpha\alpha}\int d^3r|w(\boldsymbol{r})|^4, \qquad \text{with } \alpha\alpha = gg, ee \tag{4.5}$$

The direct interaction V and exchange interaction V_{ex} terms are:

$$\begin{aligned} V &= (U_{eg^+} + U_{eg^-})/2 \\ V_{ex} &= (U_{eg^+} - U_{eg^-})/2 \end{aligned} \tag{4.6}$$

Equation (4.7) explicitly shows the effect of the direct and exchange interaction energies, V and V_{ex}, shifting the energies of the two inter-orbital interaction states.

$$\begin{aligned} U_{eg^+} &= \mathrm{V} + \mathrm{V_{ex}} \\ U_{eg^-} &= \mathrm{V} - \mathrm{V_{ex}} \end{aligned} \tag{4.7}$$

$$U_{eg^{\pm}} = \frac{4\pi\hbar^2}{M} a_{eg^{\pm}} \int d^3r |w_e(\boldsymbol{r})|^2 \left|w_g(\boldsymbol{r})\right|^2 \tag{4.8}$$

The scattering lengths a_{eg^+} and a_{eg^-} are linked to the collision channels of the symmetric and anti-symmetric two-particle states with the two atoms occupying different electronic levels: $|eg\rangle^{\pm} = (|eg\rangle \pm |ge\rangle)/\sqrt{2}$. In a magic lattice, the Wannier functions of ground and excited state equal, which simplifies equation (4.8) to the form of equation (4.5). This description holds only in the regime of weak interactions, where all interaction energies U are assumed to be significantly smaller than the energy spacing of the relevant band gap, such that on-site interactions do not reach different Bloch bands of the lattice. In case of significantly large scattering lengths, one needs to take the actual optical lattice potential into account.

4.3.1.3 Differential Zeeman shift and Zeeman Hamiltonian

Next, we introduce the effect of an external magnetic field on the two-particle states' energy levels. A differential Zeeman shift occurs between the ground and excited state of ^{173}Yb in the presence of an external magnetic field. The nuclear Zeeman shift in presence of an external magnetic field B is $\Delta E_{nZ} = g_I \cdot m_F \cdot \mu_N \cdot B$, with the nuclear Landé factor g_I, varying between electronic states, and the nuclear magneton μ_N. Due to the hyperfine interaction induced by the nuclear spin, the excited state $^3P_0$ is mixed with the $^3P_1$ state, distorting the excited state's electronic wave function. This results in a differential Landé factor δg between the ground state $^1S_0$ and excited state $^3P_0$. The excitation frequency of a π-transition is only sensitive to non-common shifts of the ground and excited state energy, ΔE_Z, given in equation (4.9).

$$\Delta E_Z = \delta g \cdot m_F \cdot \mu_B \cdot B \tag{4.9}$$

For ^{173}Yb, the differential Zeeman shift is $\Delta E_Z = h \cdot m_F \cdot B \cdot 113\ \mathrm{Hz/G}$.

As we work with symmetric spin states and drive π-transitions with the spectroscopy laser, we are only sensitive to the differential Zeeman shift. For atoms pairs in same electronic state and therefore in anti-symmetric spin state $|\uparrow\downarrow\rangle^-$, the Zeeman shift completely cancels out. States with one atom in ground and one in excited state solely experience an effect of the magnetic field, which is via the differential Zeeman shift. These are the two-particle polarized Zeeman eigenstates $|eg\uparrow\downarrow\rangle$ and $|eg\downarrow\uparrow\rangle$. $|eg\uparrow\downarrow\rangle$ is the symmetric and $|eg\downarrow\uparrow\rangle$ is the anti-symmetric superposition of the atomic interaction states $|eg\rangle^{\pm}$:

$$\begin{aligned} |eg\uparrow\downarrow\rangle &= \frac{1}{\sqrt{2}}(|e\uparrow g\downarrow\rangle - |g\downarrow e\uparrow\rangle) = |eg\rangle^-|\uparrow\downarrow\rangle^+ + |eg\rangle^+|\uparrow\downarrow\rangle^- \\ |eg\downarrow\uparrow\rangle &= \frac{1}{\sqrt{2}}(|e\downarrow g\uparrow\rangle - |g\uparrow e\downarrow\rangle) = |eg\rangle^-|\uparrow\downarrow\rangle^+ - |eg\rangle^+|\uparrow\downarrow\rangle^- \end{aligned} \tag{4.10}$$

The Zeeman Hamiltonian for two particles is then:

$$\widehat{H}_Z = \Delta E_Z \cdot (|eg\uparrow\downarrow\rangle\langle eg\uparrow\downarrow| - |eg\downarrow\uparrow\rangle\langle eg\downarrow\uparrow|) \tag{4.11}$$

Therefore, the magnetic field and Zeeman Hamiltonian introduce a coupling between the inter-orbital interaction eigenstates $|eg\rangle^-|\uparrow\downarrow\rangle^+$ and $|eg\rangle^+|\uparrow\downarrow\rangle^-$.

4.3.1.4 Two-particle Hamiltonian containing atomic interactions and the Zeeman effect

Before combining the two-particle Hamiltonian, I anticipate two considerations of clock spectroscopy on the atoms: The initial state in the experiment is the ground state $|gg\rangle|\uparrow\downarrow\rangle^-$. Electronic excitations via π-transitions do not couple the ground state with the spin-aligned states $|eg\rangle^-|\uparrow\uparrow\rangle$ and $|eg\rangle^-|\downarrow\downarrow\rangle$. I omit the spin-aligned states in the following considerations.

Equation (4.12) shows the two-particle Hamiltonian consisting of the atomic interaction Hamiltonian $\widehat{H}_{int}$ and the Zeeman Hamiltonian $\widehat{H}_Z$ and as matrix representation in the atom-atom interaction basis $\{ |gg\rangle|\uparrow\downarrow\rangle^-, |eg\rangle^+|\uparrow\downarrow\rangle^-, |eg\rangle^-|\uparrow\downarrow\rangle^+, |ee\rangle|\uparrow\downarrow\rangle^- \}$:

$$\widehat{H}_{int,Z} = \begin{pmatrix} U_{gg} & 0 & 0 & 0 \\ 0 & U_{eg^+} & \Delta E_Z & 0 \\ 0 & \Delta E_Z & U_{eg^-} & 0 \\ 0 & 0 & 0 & U_{ee} \end{pmatrix} \tag{4.12}$$

The magnetic field acts via the off-diagonal elements as it only links to eigenstates of the Zeeman Hamiltonian, as shown in (4.10), which can be written as a superposition of the inter-orbital interaction eigenstates.

Diagonalizing the central block of equation (4.12) gives the eigen energies $E_\pm$ of the inter-orbital interaction eigenstates under consideration of the Zeeman effect, $|+\rangle$ and $|-\rangle$. The eigen energies $E_\pm$ are given in equation (4.13), the corresponding eigenstates in equation (4.14).

$$E_\pm(B) = V \pm \sqrt{V_{ex}^2 + \Delta E_Z^2(B)} \tag{4.13}$$

The two-particle states' eigen energies $E_\pm$ contain the on-site inter-orbital interaction energies, U_{eg^+} and U_{eg^-}, as shown in equations (4.6) and (4.7). The coupling of the inter-orbital interaction states $|eg\rangle^+|\uparrow\downarrow\rangle^-$ and $|eg\rangle^-|\uparrow\downarrow\rangle^+$ by the differential Zeeman shift introduces the additional energy dependence on $\Delta E_Z(B)$.

Measuring the energy of $E_+(B)$ or $E_-(B)$ for different magnetic field strengths B enables to determine the interaction parameters $U_{eg^\pm}$ and from that the scattering lengths $a_{eg^\pm}$. Figure 34 sketches the magnetic field dependence of the two inter-orbital interaction energies $E_\pm(B)$.

Equation (4.14) shows the eigenstates $|+\rangle$ and $|-\rangle$ in the atomic interaction basis:

$$\begin{aligned} |+\rangle &= c_1(\Delta E_Z) \cdot |eg\rangle^+|\uparrow\downarrow\rangle^- + c_2(\Delta E_Z) \cdot |eg\rangle^-|\uparrow\downarrow\rangle^+ \\ |-\rangle &= c_1(\Delta E_Z) \cdot |eg\rangle^-|\uparrow\downarrow\rangle^+ - c_2(\Delta E_Z) \cdot |eg\rangle^+|\uparrow\downarrow\rangle^- \end{aligned} \tag{4.14}$$

The eigenstates $|+\rangle$ and $|-\rangle$ contain the magnetic field-dependent mixing coefficients $c_1(\Delta E_Z)$ and $c_2(\Delta E_Z)$ which are given in equation (4.15).

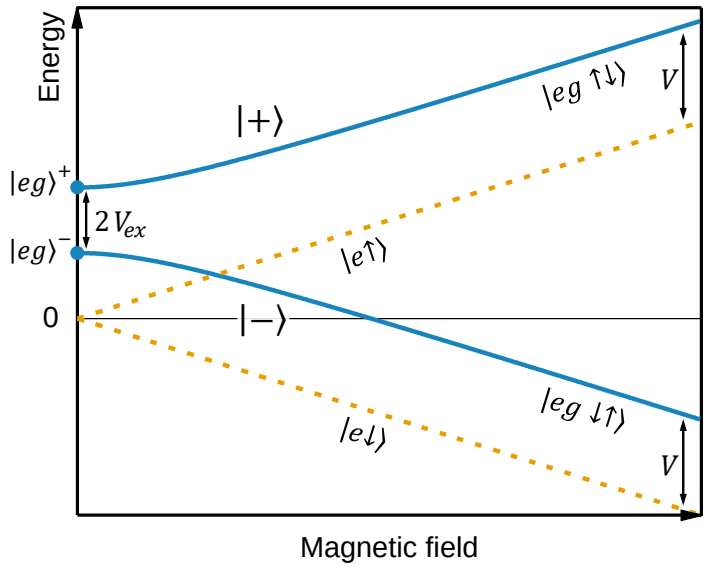

Figure 34: Illustrative graphic of energy splitting for single- and two-particle states in a magnetic field. The dotted orange lines show the energy splitting of single particle states $|e\uparrow\rangle$ and $|e\downarrow\rangle$ in singly occupied lattice sites. The differential Zeeman effect shifts their excitation energy linearly with increasing magnetic field. The solid blue lines show the two particle states $|+\rangle$ and $|-\rangle$ in doubly occupied sites. Two limiting cases can be identified: At negligible magnetic field, respectively when $V_{ex} \gg \Delta E_Z$, the Pauli principle only allows the inter-orbital interaction two-particle states $|eg\rangle^+|\uparrow\downarrow\rangle^-$ and $|eg\rangle^-|\uparrow\downarrow\rangle^+$. These are separated by the exchange interaction $2V_{ex} = U_{eg^+} - U_{eg^-}$ and offset by the direct interaction energy $V = (U_{eg^+} + U_{eg^-})/2$. Applying a magnetic field mixes these states into the two-particle states $|+\rangle$ and $|-\rangle$. At dominating magnetic field, resulting in $V_{ex} \ll \Delta E_Z$, the two-particle states reduce to the polarised Zeeman two-particle eigenstates $|eg\uparrow\downarrow\rangle$ and $|eg\downarrow\uparrow\rangle$. Energy levels and possible transitions driven by a π-polarised spectroscopy laser in the limiting cases are depicted in Figure 35. The state mixing and energy dependence allows to determine $U_{eg^\pm}$ from the magnetic field dependence of already one two-particle interaction state.

$$c_1(\Delta E_Z) = \frac{V_{ex} + \sqrt{V_{ex}^2 + \Delta E_Z^2}}{\sqrt{2V_{ex}^2 + 2E_Z^2 + 2V_{ex} \cdot \sqrt{V_{ex}^2 + \Delta E_Z^2}}}$$
$$c_2(\Delta E_Z) = \frac{\Delta E_Z}{\sqrt{2V_{ex}^2 + 2E_Z^2 + 2V_{ex} \cdot \sqrt{V_{ex}^2 + \Delta E_Z^2}}} \quad (4.15)$$

We identify two limiting cases from the mixing coefficients: For vanishing influence of the differential Zeeman energy shift compared to the exchange interaction, $\Delta E_Z \ll V_{ex}$, we obtain $c_1 = 1$ and $c_2 = 0$. In this regime, such as at zero magnetic field, the states $|+\rangle$ and $|-\rangle$ reduce to the inter-orbital interaction states without external magnetic field $|eg\rangle^+|\uparrow\downarrow\rangle^-$ and $|eg\rangle^-|\uparrow\downarrow\rangle^+$, respectively. In the limit of dominating influence of the differential Zeeman shift, i.e. $\Delta E_Z \gg V_{ex}$, such as for large magnetic fields, we obtain $c_1 = c_2 = 1/\sqrt{2}$. This corresponds to a reduction of the Rabi couplings and the states $|+\rangle$ and $|-\rangle$ effectively turning into the polarised two-particle states $|eg\uparrow\downarrow\rangle$ and $|eg\downarrow\uparrow\rangle$.

4.3.1.5 Spectroscopy Hamiltonian

Next, we regard the coupling between the atoms and the spectroscopy laser in the basis of possible two-particle atomic interaction states $\{\ |gg\rangle|\uparrow\downarrow\rangle^{-}, |eg\rangle^{+}|\uparrow\downarrow\rangle^{-},\ |eg\rangle^{-}|\uparrow\downarrow\rangle^{+}, |ee\rangle|\uparrow\downarrow\rangle^{-}\ \}$. Equation (4.16) shows the two-particle atom-laser coupling Hamiltonian for clock spectroscopy with π-polarised light on atom samples with symmetric spin states and without external magnetic field applied.

$$\widehat{H}_{L,\pi} = \sqrt{2}\cdot\frac{\hbar\Omega}{2}\left(|eg\rangle^{-}|\uparrow\downarrow\rangle^{+}\langle gg|\langle\uparrow\downarrow|^{-} - |ee\rangle|\uparrow\downarrow\rangle^{-}\langle eg|^{-}\langle\uparrow\downarrow|^{+} + h.c.\right) \tag{4.16}$$

Ω is the Rabi frequency. Only two transitions can be coupled by a clock pulse with π-polarization: The ground state $|gg\rangle|\uparrow\downarrow\rangle^{-}$ couples to the anti-symmetric inter-orbital interaction state $|eg\rangle^{-}|\uparrow\downarrow\rangle^{+}$. And $|eg\rangle^{-}|\uparrow\downarrow\rangle^{+}$ can only couple to the doubly excited state $|ee\rangle|\uparrow\downarrow\rangle^{-}$. For both transitions, the Rabi frequency is enhanced by a factor of $\sqrt{2}$ compared to a single particle state excitation.

Regarding the couplings of the ground state $|gg\rangle$, we now include the Zeeman effect in presence of an external magnetic field. Equation (4.17) shows the Hamiltonian for atom-light coupling and magnetic field, $\widehat{H}_{L,Z,\pi,\langle gg|}$, which now shows the couplings of the ground state to the states $|+\rangle$ and $|-\rangle$.

$$\begin{aligned}\widehat{H}_{L,Z,\pi,\langle gg|} \;=\; & \sqrt{2}\cdot c_2(\Delta E_Z)\cdot\frac{\hbar\Omega}{2}\cdot|+\rangle\langle gg|\langle\uparrow\downarrow|^{-} \\ & +\sqrt{2}\cdot c_1(\Delta E_Z)\cdot\frac{\hbar\Omega}{2}\cdot|-\rangle\langle eg|^{-}\langle\uparrow\downarrow|^{+} + h.c.\end{aligned} \tag{4.17}$$

Again, the mixing coefficients introduce two limiting cases: For strong atomic interaction and negligible differential Zeeman energy shift, $\Delta E_Z \ll V_{ex}$, which occurs at vanishing magnetic field, the Hamiltonian $\widehat{H}_{L,Z,\pi,\langle gg|}$ simplifies to the two-particle atom-laser coupling Hamiltonian without external magnetic field $\widehat{H}_{L,\pi}$ in equation (4.16). In this limit, the states $|+\rangle$ and $|-\rangle$ reduce to the inter-orbital interaction states $|eg\rangle^{\pm}|\uparrow\downarrow\rangle^{\mp}$.
In the limit of dominating influence of the Zeeman energy shift, $\Delta E_Z \gg V_{ex}$, as is the case with a strong magnetic field, the mixing coefficients cancel the enhancement factor of $\sqrt{2}$ to the Rabi frequency. The Rabi frequency then equals to that of single atom transitions. Furthermore, the states $|+\rangle$ and $|-\rangle$ turn into the polarised two-particle (Zeeman eigen-) states $|eg\uparrow\downarrow\rangle$ and $|eg\downarrow\uparrow\rangle$.

Figure 34 illustrates the energy shift of the two-particle states against increasing magnetic field strength and the transitioning between the two limiting cases. Figure 35 displays a schematic energy level diagram for the limiting cases showing the transitions coupled by π-polarised spectroscopy, and the coupling and mixing of interaction states by increasing Zeeman shift or by increasing atom-atom interaction, respectively.

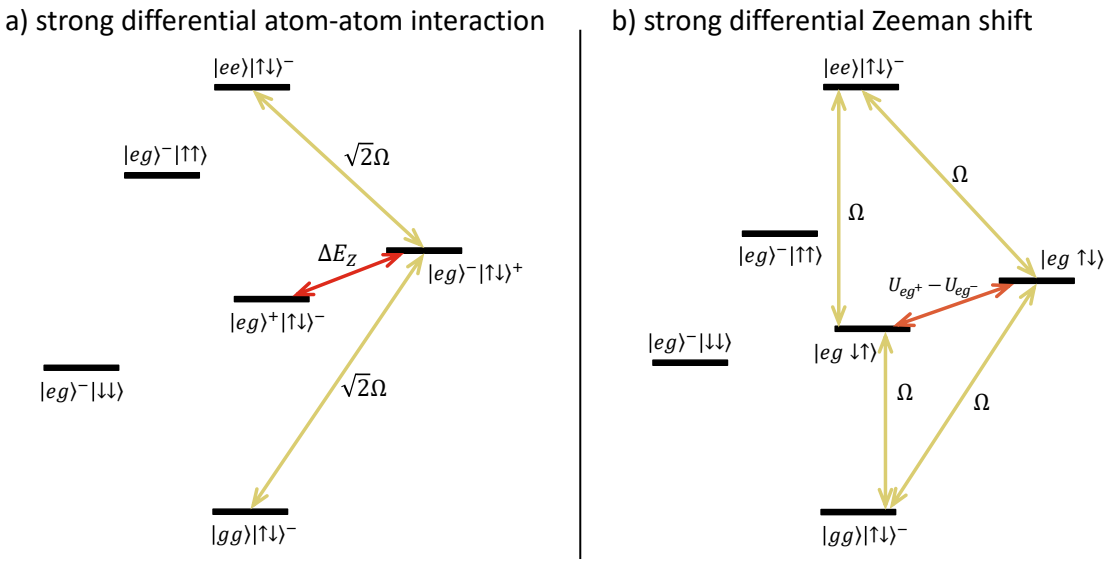

Figure 35: Energy level diagram of two-particle states with Rabi frequencies of transitions connected from the ground state $|gg\rangle|\uparrow\downarrow\rangle^-$ by π-polarised clock spectroscopy. Two limiting cases are depicted: In a) the atom-atom interaction dominates over the differential Zeeman shift, $V_{ex} \gg \Delta E_Z$, which occurs at negligible magnetic field. The two-particle interaction states $|eg\rangle^{\pm}|\uparrow\downarrow\rangle^{\mp}$ will be mixed with increasing Zeeman energy shift (red arrow), forming the two-particle states $|+\rangle$ and $|-\rangle$. In b), the differential Zeeman shift dominates the interaction, $V_{ex} \ll \Delta E_Z$. Here, an increasing the atom-atom interaction V_{ex} will couple and mix the polarised states (red arrow), forming the two-particle states. Adapted from [53].

Atoms in the doubly excited state $|ee\rangle|\uparrow\downarrow\rangle^-$ experience strong inelastic collisions and escape from our system. As we use relative excitation fractions normalized to the total atom number in our data analysis, we see no feature of the doubly excited state. When operating with stable initial atom numbers, we would expect an excitation feature of the $|ee\rangle$ state in the non-normalized data. In total, we expect three excitation features in our normalized spectrum of ultracold, two spin-component gases of ^{173}Yb loaded into the lowest band of a deep, magic-wavelength optical lattice and with external magnetic field applied: We expect two clock excitation features of singly occupied sites and a feature of the $|-\rangle$ state in between excitation energies of the former two.

In our experiment, we perform spectroscopy on the $^1S_0$-$^3P_0$ clock transition with two-component spin mixtures in the $m_F = \pm 5/2$ spin states. The electronic ground state is $|g\rangle = {}^1S_0$, the excited state as $|e\rangle = {}^3P_0$, the spin up state is $|\uparrow\rangle = |m_F = +5/2\rangle$ and the spin-down state is $|\downarrow\rangle = |m_F = -5/2\rangle$. The clock laser is linearly polarised, inducing electronic π-transitions. As we work with opposing spin states, the Clebsch-Gordan coefficients of the two π-transitions, and therefore also the transitions' Rabi frequencies, have equal magnitude but opposite sign.

4.3.2 Spectroscopy of a two-component Fermi gas

We prepared samples of $(33 \pm 2) \cdot 10^3$ ^{173}Yb atoms at temperature $T/T_F = 25\%$ with a balanced spin distribution in the $m_F = \pm 5/2$ spin states. We loaded the atoms into the lowest band of the three-dimensional magic-wavelength optical lattice. The lattice depths were $43\ E_R$ in the 1D lattice along the clock laser and $33\ E_r$ in the triangular 2D lattice. We applied clock pulses covering a pulse area of Rabi $1{\cdot}\pi$ for single particle excitations with pulse duration of 2 ms, corresponding to a FWHM of 445 Hz, and with clock beam power of 52 ± 5 µW. We sequentially shifted the clock laser's frequency detuning between every cycle and additionally forwarded a continuous, linear drift compensation. At the end of a coherent spectroscopy cycle we performed absorption imaging and counted the atom numbers in ground and excited state.

We applied an external magnetic field of 11,6 G along the y-axis in the setup (axis label relates to setup graph in Figure 1 b)). The magnetic field defines the quantization axis and introduces a Zeeman energy shift to the clock excitation energies. We use the Zeeman splitting of singly occupied lattice sites as reference in the spectra: First, we determine the effective magnetic field strength from the frequency spacing between the peaks. Furthermore, the mid-frequency between the two single-particle excitations gives the unshifted clock transition frequency. The unshifted clock transition frequency serves as reference between different spectra recorded when the magnetic field strength is varied.

Figure 36 shows the measured spectrum with three excitation peaks in the relative number of ground state atoms. We associate the two outer, large excitation peaks to excitations of the single-particle states $|e\uparrow\rangle$ and $|e\downarrow\rangle$ in singly occupied lattice sites. In between the two peaks, close to the zero-frequency value marking the unshifted clock excitation energy, we observe the excitation peak of the $|-\rangle$ two-particle interaction state. Considering the applied magnetic field strength and taking results for V, V_{ex} from [26,27] into account, this measurement is in the limit of $\Delta E_Z \ll V_{ex}$, with the $|-\rangle$ state predominantly being the $|eg\rangle^-$ state.

The excitation amplitudes of the single particle states sum up to about 85% of the detected atoms, leaving up to 15% of atoms possible in doubly occupied lattice sites. However, this does not coincide with the expectations from a lattice simulation in [55], giving the 29% of atoms in doubly occupied sites. The excitation amplitude of the $|-\rangle$ state of 11% can also be used to determine the amount of doubly occupied sites, but requires two considerations: First, a reduced excitation fraction resulting from a mismatched Rabi frequency for the $|-\rangle$ state by factor $\sqrt{2}$ and the mixing coefficient $c_1(\Delta B_Z) \approx 98\%$ for our experimental into account underestimate the peak amplitude by 31%. Second, the excitation peaks of the two-particle interaction state results from doubly occupied lattice sites of which only one atom is excited. In total this gives about 31% of atoms paired in doubly occupied lattice sites, which coincides well with the simulation result. The discrepancy to the relative amount of single excitation peaks is unclear.

The most interesting feature of the spectrum is the excitation frequency of the two-particle interaction state $|-\rangle$. We observe the position of the $|-\rangle$ state at -240 ± 20 Hz in our

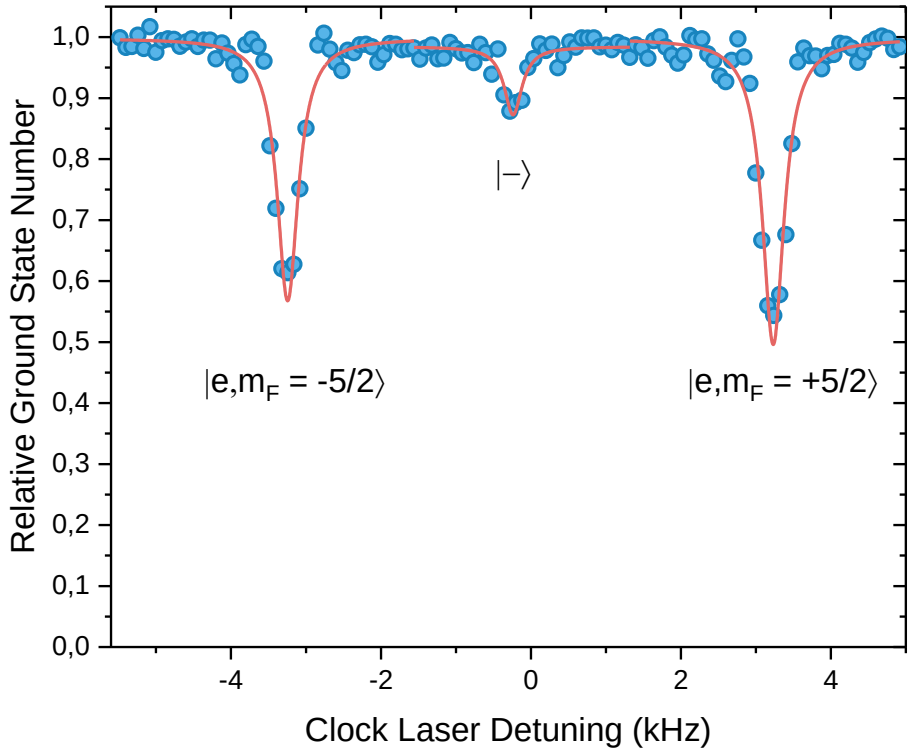

Figure 36: Spectrum of a ^{173}Yb quantum-degenerate gas, with the spin-components $m_F = \pm 5/2$, in the lowest band of a magic-wavelength optical lattice and at 11,6 G external magnetic field strength. We used coherent spectroscopy with Rabi 1·π pulses of 2 ms duration and π-polarizion of the clock laser. The spectrum shows the relative ground state fraction with locally fitted Lorentz curves at the excitation dips. We associate the two outer peaks to singly occupied sites with $m_F = +5/2$ and $m_F = -5/2$ spin-state atoms, the degeneracy lifted by the differential Zeeman effect. These peaks were used to define the zero-detuning in the spectrum, giving the unshifted single particle clock excitation frequency. The central peak relates to the two-particle state $|-\rangle$, as shown in the illustrative energy diagram in Figure 34.

measurement shown in Figure 36. We did not record a measurement set with varying magnetic field strengths in the course of this PhD. We can compare the position of our single measurement with results from comprehensive measurement series and results published by groups in Munich [26,34,62] and Florence [27]. However, the peak position in our measurement does not coincide with their data at similar conditions, expecting the peak position at approximately $+200$. For a founded analysis of this discrepancy, additional measurement series varying the magnetic field strength and varying the spin combinations are necessary.

From the magnetic field dependence of the interaction state one can determine the direct and exchange interaction strengths V and V_{ex}. Equations (4.6) and (4.8) show that these are directly related to the inter-orbital interaction energies U_{eg^+} and U_{eg^-} in the optical lattice. In combination with ground state scattering length $a_{gg} = 199{,}4\ a_0$ [100], the interaction energies reveal the *s*-wave scattering lengths a_{eg^-} [26] and a_{eg^+} [27,34] (the precise value of latter differs slightly in its first, recent publications):

$$a_{eg^-} = 219{,}5\ a_0$$

$a_{eg^+} = 3300 \pm 300\ a_0$ [27], respectively $a_{eg^+} = 1878 \pm 37\ a_0$ [34]

The large difference of the scattering lengths and the resulting large exchange interaction strength, together with the possibility to tune the exchange interaction strength via the lattice confinement, makes ^{173}Yb a promising candidate to experimentally investigate the phase diagram of the Kondo lattice model [25,39,43].

4.4 Further experiments on spin-exchange interactions

I presented that, with our experiment, we successfully observed a feature of spin-exchange interactions in a spectrum of a two-component spin mixture of ^{173}Yb. As mentioned above, the next step would be to record the magnetic field dependent frequency shift of the interaction peak and to **extract the spin-exchange interaction energies** and respective scattering lengths. In this section, I list complementing measurements for a systematic investigation of (many-body) features in ^{173}Yb which can be realized with our setup as presented, orienting on the experiments published in [26,27,53,62].

Extracting the exchange interaction strengths in ^{173}Yb for varying the combinations of two spin components can **verify the SU(N) symmetry** of the atoms if matching interaction strengths are obtained. And measuring the **magnitude of loss processes** present in the system, especially of the excited two-particle states, gives valuable information for the realization of complex many-body systems with Yb in the future.

The **direct observation of spin oscillation dynamics** in a two-component mixture, as presented in [27], is another approach to obtain the spin-exchange interaction strengths. It requires the preparation of the many-body state in a strong magnetic field of ≈ 60 G and the capability to reduce the magnetic field strength within ≈30 μs to sufficiently populate the $|eg\rangle^+$ state in the starting configuration for interaction induced spin-oscillations at low magnetic field strength. This measurement also verifies the coherence of the spin-exchange process.

A measurement of **Rabi oscillations** of π-transitions in a spin-polarised Fermi gas would give information on the coherence time of the clock laser and dephasing effects of the excitation. This information would complement the high-resolution spectra. Rabi oscillations of π-transitions in a six-component spin mixture would show the relative strengths of the spin-state dependent Rabi frequencies superimposed.

Measuring the clock excitation frequencies for single-component spectra of opposite spin states in a magnetic field gives the excitation frequency of the clock transition without Zeeman shifts at the mid-frequency between the excitations. This **absolute clock transition frequency** can serve as magnetic field independent reference for tracking the drift of the cavity resonance frequency and relate different spectra showing spin-exchange interaction shifts to each other.

Chapter 5 Summary and Outlook

In this thesis I presented a detailed evaluation of a highly stable "clock" laser system and its application in an experiment investigating of two-body interactions in Fermionic Ytterbium.

Fermionic Ytterbium has favourable electronic properties for the investigation of many-body physics in ultracold quantum gases: It provides a ground- and a low-lying metastable state, both with independent spin and electronic degrees of freedom. This preserves the spin-state atomic collision and fulfils a SU(N) symmetry. Atomic interactions in fermionic Yb result in two two-atom states, an orbital-symmetric spin-singlet state $|eg\rangle^+|\uparrow\downarrow\rangle^-$ and an orbital-antisymmetric spin-triplet state $|eg\rangle^-|\uparrow\downarrow\rangle^+$. Due to different scattering lengths of these interaction states, a spin-exchange interaction V_{ex} arises between these two states and a Zeeman coupling introduces an energy level dependence to an external magnetic field. This makes it possible to obtain the two-body spin-exchange interaction strengths in Yb by spectroscopy on the $^1S_0$-$^3P_0$ clock transition. And these Ytterbium features enable realizations of complex quantum many-body systems, such as the Kondo lattice model [37,45].

Experiments with ultracold Ytterbium require an elaborate setup to cool and prepare the atoms, to load them into a highly controlled, well-defined optical lattice, to probe and finally to image the atoms. Recapitulating the abilities of our apparatus, I stated that we can reliably prepare ultra-cold Yb quantum gases with well-defined, clean spin populations. We can load several 10^4 atoms into the lowest band of a magic-wavelength optical lattice at 759 nm with up to 47 E_R lattice depth. The deep optical lattice enables us to perform Fourier limited spectroscopy in the Lamb-Dicke regime. Finally, we can detect both ground- and metastable state atoms making use of a repump laser on the $^3P_0$-$^3D_1$ transition at 1388 nm. With this setup and the highly-stable clock laser, we fulfil the demanding prerequisites for quantum gas experiments with Ytterbium.

Our 578 nm clock laser system is referenced by Pound-Drever-Hall (PDH) lock to a highly stable, high-finesse cavity, placed in a temperature-controlled environment in a vacuum system. During this PhD, we realised several improvements of the clock laser system and its integration in the experiment, which I described in this thesis:
A new, all-ULE cavity shows a zero-crossing of its coefficient of thermal expansion (CTE-ZC) at $T_{CTE-ZC} = 32{,}3 \pm 0{,}1$ °C. This enables a temperature sensitivity and a beam power sensitivity of the cavity resonance frequency several orders of magnitude lower than with the initial cavity, made of an ULE spacer and fused silica mirrors which operated tens of K away from its CTE-ZC temperature.
We achieve a beam power stability level below 10^{-2}, required for a (sub-)Hz stability of the cavity resonance frequency.

A waveguide-based, fibre-coupled EOM requiring low modulation voltages enables an optimal PDH error signal. Furthermore, the temperature stabilised EOM exhibits intrinsically low levels of residual amplitude modulation (RAM) noise in the PDH lock.
We improved the clock laser integration in the experiment by referencing a phase stabilization of the clock beam as close as possible to the retro reflex mirror of the 1D lattice, thereby avoiding fluctuating Doppler shifts between lattice- and clock laser beams.

We evaluated the clock laser system's performance by a beat with a beam independently stabilised to another cavity. I showed narrow short-time linewidths of 1 Hz in 2 s and around 10 Hz in 60-90 s. Low frequency noise in the systems leads to a broadening of the combined linewidth. Monitoring of the beat frequency showed up to 1 h long intervals of approximately linear drift. Therein, drifts were within 50 Hz range along with fast frequency fluctuations of 20-30 Hz. These cavity-cavity beat measurements are dominated by a significantly worse stability of the reference cavity.
In atom spectroscopy measurements, we determined a linear drift of the new cavity of -318 ± 1 mHz/s, with several-hour-long linear deviations of 5-33 mHz/s. These deviations might indicate a non-optimal temperature stabilisation of the cavity. These characterisation measurements show an excellent short-time stability of the clock laser system and an extended, good stability on the tens of Hz level for spectroscopy measurements taking up to one hour.

The detailed analysis of the clock laser system identified various approaches for improvements in future revisions, especially for experiments requiring higher resolutions and extended measurement times with high frequency stability. Possible upgrades may include the implementation of a frequency noise cancellation (FNC) in the PDH setup, a double frequency modulation scheme at the EOM enabling fast frequency shifts and sweeps [62], the stabilization of the clock laser beam power at the experiment, an improved FNC setup at the experiment to resolve technical limitations occurring at low beam power, and, ideally, a highly stable reference signal for the clock laser, such as a narrow linewidth comb or an optical reference signal from a metrology institute [68].

In clock spectroscopy measurements on ultracold, spin-polarised ^{173}Yb in the magic-wavelength optical lattice, we first evaluated the performance of the atom preparation and of the clock laser system in particular. We recorded high-resolution spectra of a spin-polarised ^{173}Yb degenerate Fermi gases in the lowest band of the deep optical lattice. We achieved a Fourier limited resolution of 50 ± 2 Hz FWHM (sinc^2 fit) and excitation fractions above 80%. The resolution was limited by the stability of the clock laser and by technical limitations encountered when operating with low clock beam powers at the atoms. Optical sideband spectroscopy measurements with spin-polarised ultracold ^{173}Yb in the optical lattice confirmed an efficient loading of atoms into the lowest lattice band.

Finally, I presented a clock spectroscopy measurement of a two spin-component mixture in the deep magic-wavelength optical lattice. We clearly resolved a feature showing spin-exchange interactions between two atoms occupying a lattice site. This measurement proved the capability of our experiment to investigate two-body interactions in Ytterbium quantum gases.

Next, one could qualitatively measure the two-body spin-exchange interaction strength in ^{173}Yb by exploiting the magnetic field dependence of the interaction state energy.

I suggested complementary measurements on ^{173}Yb possible with the experimental setup, orienting on publications from groups in Munich and Florence [26,27]: Rabi frequency oscillations in single spin-component gases could show the clock laser's coherence time and emphasize the coherent control over the metastable state. Measurements of the spin-exchange interaction with varying spin combinations in could verify the SU(N) symmetry. And a direct observation of spin-exchange interaction oscillations would show the coherent nature of the process. The latter requires a sufficient coupling of the two interaction states which needs strong magnetic fields with fast switching capability.

Finally, I give a brief outlook on exciting features currently being implemented in the Ytterbium experiment paving the way to realize experiments on frontier topics of quantum many-body physics in the near future.

A state-dependent lattice at 660 nm enables a realization of the Kondo lattice model, in which ground state atoms can tunnel between lattice sites in front of a background of localised atoms in the metastable state [55,57]. Here, Yb enables to implement Hamiltonians in experiments beyond the capabilities of alkali atoms. Developing a preparation scheme of $^1S_0$-$^3P_0$ atoms in the lattice will be the next step. Exploring the phase diagrams in one-, two- and three-dimensional systems by applying corresponding optical lattice confinements gives opportunities for many interesting experiments [25,39,43].
Furthermore, implementing orbital Feshbach resonances [33–35] or confinement induced resonances [44] would enable to tune the atomic interaction strength in Yb. This would extend the accessible parameter regime and possibly allow to access novel quantum phases and phase transitions. An advanced realization of a Kondo lattice model with tuneable anisotropy was recently proposed [39].

The simultaneous cooling of two Yb isotopes can be realized with the current laser setup [55,56], the available isotopes being ^{171}Yb, ^{173}Yb and ^{174}Yb. The 399 nm laser system is capable to sequentially load two isotopes from the 2D MOT into the 3D MOT. A loading and cooling scheme realizing Yb isotope mixtures is being implemented. Isotope mixtures of ultracold Yb enable studying Bose-Fermi statistics by combining ^{171}Yb & ^{174}Yb or ^{173}Yb & ^{174}Yb, and fermi-fermi statistics by combining ^{171}Yb & ^{173}Yb [101,102].

Being able to load isotope mixtures into the 3D MOT enables to cool the ^{171}Yb isotope to quantum degeneracy, which requires another scattering partner for evaporative cooling. A first experiment with ^{171}Yb would then be the characterisation of its spin-exchange interaction strength and its scattering length in the excited clock state. Measuring these parameters would allow to predict realizable quantum phases in a Kondo lattice model with Yb.

Lastly, a further analysis of dissipative systems by continuous loss measurements could be pursued, extending the investigations performed by Bastian Hundt [54], André Kochanke [55] and me. With the updated clock laser system and novel insights from theoretical analysis of the

initial experiment [P1], an improved atom preparation scheme should be possible. Also, in contrast to the interaction-dominated regime accessible with ^{173}Yb, a loss-dominated regime could be reached with the ^{171}Yb isotope.

Bibliography

[1] P. W. Anderson, ‘More Is Different’, *Science*, vol. 177, no. 4047, pp. 393–396, Aug. 1972. https://doi.org/10.1126/science.177.4047.393

[2] R. P. Feynman, ‘Simulating physics with computers’, *Int. J. Theor. Phys.*, vol. 21, no. 6–7, pp. 467–488, Jun. 1982. https://doi.org/10.1007/BF02650179

[3] D. Jaksch, C. Bruder, J. I. Cirac, C. W. Gardiner, and P. Zoller, ‘Cold Bosonic Atoms in Optical Lattices’, *Phys. Rev. Lett.*, vol. 81, no. 15, pp. 3108–3111, Oct. 1998. https://doi.org/10.1103/PhysRevLett.81.3108

[4] I. Bloch, ‘Ultracold quantum gases in optical lattices’, *Nat. Phys.*, vol. 1, no. 1, pp. 23–30, Oct. 2005. https://doi.org/10.1038/nphys138

[5] C. Gross and I. Bloch, ‘Quantum simulations with ultracold atoms in optical lattices’, *Science*, vol. 357, no. 6355, pp. 995–1001, Sep. 2017. https://doi.org/10.1126/science.aal3837

[6] M. H. Anderson, J. R. Ensher, M. R. Matthews, C. E. Wieman, and E. A. Cornell, ‘Observation of Bose-Einstein Condensation in a Dilute Atomic Vapor’, *Science*, vol. 269, no. 5221, pp. 198–201, Jul. 1995. https://doi.org/10.1126/science.269.5221.198

[7] B. DeMarco and D. S. Jin, ‘Onset of Fermi Degeneracy in a Trapped Atomic Gas’, *Science*, vol. 285, no. 5434, pp. 1703–1706, Sep. 1999. https://doi.org/10.1126/science.285.5434.1703

[8] K. B. Davis, M.-O. Mewes, M. R. Andrews, N. J. van Druten, D. S. Durfee, D. M. Kurn, and W. Ketterle, ‘Bose-Einstein Condensation in a Gas of Sodium Atoms’, *Phys. Rev. Lett.*, vol. 75, no. 22, pp. 3969–3973, Nov. 1995. https://doi.org/10.1103/PhysRevLett.75.3969

[9] K. Aikawa, A. Frisch, M. Mark, S. Baier, A. Rietzler, R. Grimm, and F. Ferlaino, ‘Bose-Einstein Condensation of Erbium’, *Phys. Rev. Lett.*, vol. 108, no. 21, p. 210401, May 2012. https://doi.org/10.1103/PhysRevLett.108.210401

[10] A. Griesmaier, J. Werner, S. Hensler, J. Stuhler, and T. Pfau, ‘Bose-Einstein Condensation of Chromium’, *Phys. Rev. Lett.*, vol. 94, no. 16, p. 160401, Apr. 2005. https://doi.org/10.1103/PhysRevLett.94.160401

[11] M. Lu, N. Q. Burdick, S. H. Youn, and B. L. Lev, ‘Strongly Dipolar Bose-Einstein Condensate of Dysprosium’, *Phys. Rev. Lett.*, vol. 107, no. 19, p. 190401, Oct. 2011. https://doi.org/10.1103/PhysRevLett.107.190401

[12] A. Gaëtan, Y. Miroshnychenko, T. Wilk, A. Chotia, M. Viteau, D. Comparat, P. Pillet, A. Browaeys, and P. Grangier, ‘Observation of collective excitation of two individual atoms in the Rydberg blockade regime’, *Nat. Phys.*, vol. 5, no. 2, pp. 115–118, Feb. 2009. https://doi.org/10.1038/nphys1183

[13] E. Urban, T. A. Johnson, T. Henage, L. Isenhower, D. D. Yavuz, T. G. Walker, and M. Saffman, 'Observation of Rydberg blockade between two atoms', *Nat. Phys.*, vol. 5, no. 2, pp. 110–114, Feb. 2009. https://doi.org/10.1038/nphys1178

[14] S. Kraft, F. Vogt, O. Appel, F. Riehle, and U. Sterr, 'Bose-Einstein Condensation of Alkaline Earth Atoms: Ca-40', *Phys. Rev. Lett.*, vol. 103, no. 13, p. 130401, Sep. 2009. https://doi.org/10.1103/PhysRevLett.103.130401

[15] S. Stellmer, M. K. Tey, B. Huang, R. Grimm, and F. Schreck, 'Bose-Einstein Condensation of Strontium', *Phys. Rev. Lett.*, vol. 103, no. 20, p. 200401, Nov. 2009. https://doi.org/10.1103/PhysRevLett.103.200401

[16] T. Fukuhara, Y. Takasu, M. Kumakura, and Y. Takahashi, 'Degenerate Fermi Gases of Ytterbium', *Phys. Rev. Lett.*, vol. 98, no. 3, p. 030401, Jan. 2007. https://doi.org/10.1103/PhysRevLett.98.030401

[17] Y. Takasu, K. Maki, K. Komori, T. Takano, K. Honda, M. Kumakura, T. Yabuzaki, and Y. Takahashi, 'Spin-Singlet Bose-Einstein Condensation of Two-Electron Atoms', *Phys. Rev. Lett.*, vol. 91, no. 4, Jul. 2003. https://doi.org/10.1103/PhysRevLett.91.040404

[18] M. Takamoto, F.-L. Hong, R. Higashi, and H. Katori, 'An optical lattice clock', *Nature*, vol. 435, no. 7040, pp. 321–324, Mai 2005. https://doi.org/10.1038/nature03541

[19] N. Hinkley, J. A. Sherman, N. B. Phillips, M. Schioppo, N. D. Lemke, K. Beloy, M. Pizzocaro, C. W. Oates, and A. D. Ludlow, 'An Atomic Clock with 1E−18 Instability', *Science*, p. 1240420, Aug. 2013. https://doi.org/10.1126/science.1240420

[20] B. J. Bloom, T. L. Nicholson, J. R. Williams, S. L. Campbell, M. Bishof, X. Zhang, W. Zhang, S. L. Bromley, and J. Ye, 'An optical lattice clock with accuracy and stability at the 10^{-18} level', *Nature*, vol. 506, no. 7486, pp. 71–75, Feb. 2014. https://doi.org/10.1038/nature12941

[21] S. Falke, N. Lemke, C. Grebing, B. Lipphardt, S. Weyers, Vladislav Gerginov, N. Huntemann, C. Hagemann, A. Al-Masoudi, S. Häfner, S. Vogt, Uwe Sterr, and C. Lisdat, 'A strontium lattice clock with 3×10^{-17} inaccuracy and its frequency', *New J. Phys.*, vol. 16, no. 7, p. 073023, 2014. https://doi.org/10.1088/1367-2630/16/7/073023

[22] M. A. Cazalilla and A. M. Rey, 'Ultracold Fermi gases with emergent SU(N) symmetry', *Rep. Prog. Phys.*, vol. 77, no. 12, p. 124401, 2014. https://doi.org/10.1088/0034-4885/77/12/124401

[23] M. Hermele and V. Gurarie, 'Topological liquids and valence cluster states in two-dimensional SU(N) magnets', *Phys. Rev. B*, vol. 84, no. 17, p. 174441, Nov. 2011. https://doi.org/10.1103/PhysRevB.84.174441

[24] M. Foss-Feig, A. J. Daley, J. K. Thompson, and A. M. Rey, 'Steady-State Many-Body Entanglement of Hot Reactive Fermions', *Phys. Rev. Lett.*, vol. 109, no. 23, p. 230501, Dec. 2012. https://doi.org/10.1103/PhysRevLett.109.230501

[25] A. V. Gorshkov, M. Hermele, V. Gurarie, C. Xu, P. S. Julienne, J. Ye, P. Zoller, E. Demler, M. D. Lukin, and A. M. Rey, 'Two-orbital SU(N) magnetism with ultracold alkaline-earth atoms', *Nat. Phys.*, vol. 6, no. 4, pp. 289–295, Apr. 2010. https://doi.org/10.1038/nphys1535

[26] F. Scazza, C. Hofrichter, M. Höfer, P. C. De Groot, I. Bloch, and S. Fölling, 'Observation of two-orbital spin-exchange interactions with ultracold SU(N)-symmetric fermions', *Nat. Phys.*, vol. 10, no. 10, pp. 779–784, Oktober 2014. https://doi.org/10.1038/nphys3061

[27] G. Cappellini, 'Direct Observation of Coherent Interorbital Spin-Exchange Dynamics', *Phys. Rev. Lett.*, vol. 113, no. 12, 2014. https://doi.org/10.1103/PhysRevLett.113.120402

[28] X. Zhang, M. Bishof, S. Bromley, C. Kraus, M. Safronova, P. Zoller, A. M. Rey, and J. Ye, 'Spectroscopic observation of SU(N)-symmetric interactions in Sr orbital magnetism', *Science*, vol. 345, no. 6203, pp. 1467–1473, 2014. https://doi.org/10.1126/science.1254978

[29] M. Sigrist and K. Ueda, 'Phenomenological theory of unconventional superconductivity', *Rev. Mod. Phys.*, vol. 63, no. 2, pp. 239–311, Apr. 1991. https://doi.org/10.1103/RevModPhys.63.239

[30] P. Coleman, 'Heavy Fermions: electrons at the edge of magnetism', *ArXivcond-Mat0612006*, Nov. 2006. http://arxiv.org/abs/cond-mat/0612006

[31] M. Foss-Feig, M. Hermele, V. Gurarie, and A. M. Rey, 'Heavy fermions in an optical lattice', *Phys. Rev. A*, vol. 82, no. 5, p. 053624, Nov. 2010. https://doi.org/10.1103/PhysRevA.82.053624

[32] Y. Zhong, Y. Liu, and H.-G. Luo, 'Simulating heavy fermion physics in optical lattice: Periodic Anderson model with harmonic trapping potential', *Front. Phys.*, vol. 12, no. 5, p. 127502, Oct. 2017. https://doi.org/10.1007/s11467-017-0690-x

[33] R. Zhang, Y. Cheng, H. Zhai, and P. Zhang, 'Orbital Feshbach Resonance in Alkali-Earth Atoms', *Phys. Rev. Lett.*, vol. 115, no. 13, p. 135301, Sep. 2015. https://doi.org/10.1103/PhysRevLett.115.135301

[34] M. Höfer, L. Riegger, F. Scazza, C. Hofrichter, D. R. Fernandes, M. M. Parish, J. Levinsen, I. Bloch, and S. Fölling, 'Observation of an Orbital Interaction-Induced Feshbach Resonance in 173Yb', *Phys. Rev. Lett.*, vol. 115, no. 26, p. 265302, Dec. 2015. https://doi.org/10.1103/PhysRevLett.115.265302

[35] G. Pagano, M. Mancini, G. Cappellini, L. Livi, C. Sias, J. Catani, M. Inguscio, and L. Fallani, 'Strongly Interacting Gas of Two-Electron Fermions at an Orbital Feshbach Resonance', *Phys. Rev. Lett.*, vol. 115, no. 26, p. 265301, Dec. 2015. https://doi.org/10.1103/PhysRevLett.115.265301

[36] M. A. Cazalilla, A. F. Ho, and M. Ueda, 'Ultracold gases of ytterbium: ferromagnetism and Mott states in an SU(6) Fermi system', *New J. Phys.*, vol. 11, no. 10, p. 103033, 2009. https://doi.org/10.1088/1367-2630/11/10/103033

[37] M. Foss-Feig, M. Hermele, and A. M. Rey, 'Probing the Kondo lattice model with alkaline-earth-metal atoms', *Phys. Rev. A*, vol. 81, no. 5, p. 051603, May 2010. https://doi.org/10.1103/PhysRevA.81.051603

[38] M. Hermele, V. Gurarie, and A. M. Rey, 'Mott Insulators of Ultracold Fermionic Alkaline Earth Atoms: Underconstrained Magnetism and Chiral Spin Liquid', *Phys. Rev. Lett.*, vol. 103, no. 13, p. 135301, Sep. 2009. https://doi.org/10.1103/PhysRevLett.103.135301

[39] M. Kanász-Nagy, Y. Ashida, T. Shi, C. P. Moca, T. N. Ikeda, S. Fölling, J. I. Cirac, G. Zaránd, and E. A. Demler, 'Exploring the Kondo model in and out of equilibrium with alkaline-earth atoms', *ArXiv180101132 Cond-Mat Physicsquant-Ph*, Jan. 2018. http://arxiv.org/abs/1801.01132

[40] A. J. Daley, M. M. Boyd, J. Ye, and P. Zoller, 'Quantum Computing with Alkaline-Earth-Metal Atoms', *Phys. Rev. Lett.*, vol. 101, no. 17, p. 170504, Oct. 2008. https://doi.org/10.1103/PhysRevLett.101.170504

[41] A. V. Gorshkov, A. M. Rey, A. J. Daley, M. M. Boyd, J. Ye, P. Zoller, and M. D. Lukin, 'Alkaline-Earth-Metal Atoms as Few-Qubit Quantum Registers', *Phys. Rev. Lett.*, vol. 102, no. 11, p. 110503, Mar. 2009. https://doi.org/10.1103/PhysRevLett.102.110503

[42] K. Shibata, S. Kato, A. Yamaguchi, S. Uetake, and Y. Takahashi, 'A scalable quantum computer with ultranarrow optical transition of ultracold neutral atoms in an optical lattice', *Appl. Phys. B*, vol. 97, no. 4, p. 753, Dec. 2009. https://doi.org/10.1007/s00340-009-3696-4

[43] L. Riegger, N. Darkwah Oppong, M. Höfer, D. R. Fernandes, I. Bloch, and S. Fölling, 'Localized Magnetic Moments with Tunable Spin Exchange in a Gas of Ultracold Fermions', *Phys. Rev. Lett.*, vol. 120, no. 14, Apr. 2018. https://doi.org/10.1103/PhysRevLett.120.143601

[44] R. Zhang, D. Zhang, Y. Cheng, W. Chen, P. Zhang, and H. Zhai, 'Kondo effect in alkaline-earth-metal atomic gases with confinement-induced resonances', *Phys. Rev. A*, vol. 93, no. 4, p. 043601, Apr. 2016. https://doi.org/10.1103/PhysRevA.93.043601

[45] M. Nakagawa and N. Kawakami, 'Laser-Induced Kondo Effect in Ultracold Alkaline-Earth Fermions', *Phys. Rev. Lett.*, vol. 115, no. 16, p. 165303, Oct. 2015. https://doi.org/10.1103/PhysRevLett.115.165303

[46] G. Chen, K. R. A. Hazzard, A. M. Rey, and M. Hermele, 'Synthetic-gauge-field stabilization of the chiral-spin-liquid phase', *Phys. Rev. A*, vol. 93, no. 6, p. 061601, Jun. 2016. https://doi.org/10.1103/PhysRevA.93.061601

[47] J. Dalibard, F. Gerbier, G. Juzeliūnas, and P. Öhberg, 'Colloquium: Artificial gauge potentials for neutral atoms', *Rev. Mod. Phys.*, vol. 83, no. 4, pp. 1523–1543, Nov. 2011. https://doi.org/10.1103/RevModPhys.83.1523

[48] F. Gerbier and J. Dalibard, 'Gauge fields for ultracold atoms in optical superlattices', *New J. Phys.*, vol. 12, no. 3, p. 033007, 2010. https://doi.org/10.1088/1367-2630/12/3/033007

[49] S. Taie, R. Yamazaki, S. Sugawa, and Y. Takahashi, 'An SU(6) Mott insulator of an atomic Fermi gas realized by large-spin Pomeranchuk cooling', *Nat. Phys.*, vol. 8, no. 11, pp. 825–830, Nov. 2012. https://doi.org/10.1038/nphys2430

[50] S. Taie, Y. Takasu, S. Sugawa, R. Yamazaki, T. Tsujimoto, R. Murakami, and Y. Takahashi, 'Realization of a SU(2) x SU(6) System of Fermions in a Cold Atomic Gas', *Phys. Rev. Lett.*, vol. 105, no. 19, p. 190401, Nov. 2010. https://doi.org/10.1103/PhysRevLett.105.190401

[51] S. Dörscher, A. Thobe, B. Hundt, A. Kochanke, R. Le Targat, P. Windpassinger, C. Becker, and K. Sengstock, 'Creation of quantum-degenerate gases of ytterbium in a compact 2D-/3D-magneto-optical trap setup', *Rev. Sci. Instrum.*, vol. 84, no. 4, pp. 043109-043109–7, Apr. 2013. https://doi.org/doi:10.1063/1.4802682

[52] S. Dörscher, ‘Creation of ytterbium quantum gases with a compact 2D-/3D-MOT setup’, PhD Thesis, Universität Hamburg, Hamburg, 2013

[53] A. Thobe, ‘Ultracold Yb Gases with Control over Spin and Orbital Degrees of Freedom’, PhD Thesis, Universität Hamburg, 2014. http://ediss.sub.uni-hamburg.de/volltexte/2014/6932/

[54] B. Hundt, ‘Optical Potentials for the Realization of Dissipative Fermi-Hubbard Models with Ultracold Ytterbium Atoms’, PhD Thesis, 2016. http://ediss.sub.uni-hamburg.de/volltexte/2017/8407/

[55] A. Kochanke, ‘Towards Quantum Simulation of the Kondo-Lattice-Model’, PhD Thesis, Universität Hamburg, Hamburg, 2017. http://ediss.sub.uni-hamburg.de/volltexte/2017/8496

[56] B. Abeln, ‘Design, Implementation and Characterization of a new Laser System for Mixtures of Ytterbium Quantum Gases’, Master Thesis, Universität Hamburg, 2016

[57] A. Skottke, ‘Setup of a State-Dependent Lattice for the Realization of the 1D-Kondo-Lattice-Model with Ultracold Ytterbium-Atoms’, Master Thesis, Universität Hamburg, 2016

[58] N. I. Petersen, ‘Setup and characterization of a triangular optical lattice for Ytterbium’, Master Thesis, Universität Hamburg, 2014

[59] T. Sobottke, ‘Design and realisation of a high-resolution imaging system for Ytterbium quantum gases’, Bachelor Thesis, Universität Hamburg, 2014

[60] S. G. Porsev and A. Derevianko, ‘Hyperfine quenching of the metastable 3P(0,2) states in divalent atoms’, *Phys. Rev. A*, vol. 69, no. 4, p. 042506, Apr. 2004. https://doi.org/10.1103/PhysRevA.69.042506

[61] Z. W. Barber, J. E. Stalnaker, N. D. Lemke, N. Poli, C. W. Oates, T. M. Fortier, S. A. Diddams, L. Hollberg, C. W. Hoyt, A. V. Taichenachev, and V. I. Yudin, ‘Optical Lattice Induced Light Shifts in an Yb Atomic Clock’, *Phys. Rev. Lett.*, vol. 100, no. 10, p. 103002, Mar. 2008. https://doi.org/10.1103/PhysRevLett.100.103002

[62] F. Scazza, ‘Probing SU(N)-symmetric orbital interactions with ytterbium Fermi gases in optical lattices’, PhD Thesis, Ludwig-Maximilians-Universität München, München, 2015

[63] Z. Barber, ‘Ytterbium optical lattice clock’, University of Colorado at Boulder, 2007. https://search.proquest.com/docview/304868454?accountid=11262

[64] J. Alnis, A. Matveev, N. Kolachevsky, T. Udem, and T. W. Hänsch, ‘Subhertz linewidth diode lasers by stabilization to vibrationally and thermally compensated ultralow-expansion glass Fabry-Pérot cavities’, *Phys. Rev. A*, vol. 77, no. 5, p. 053809, Mai 2008. https://doi.org/10.1103/PhysRevA.77.053809

[65] R. W. P. Drever, J. L. Hall, F. V. Kowalski, J. Hough, G. M. Ford, A. J. Munley, and H. Ward, ‘Laser phase and frequency stabilization using an optical resonator’, *Appl. Phys. B*, vol. 31, no. 2, pp. 97–105, Jun. 1983. https://doi.org/10.1007/BF00702605

[66] E. D. Black, ‘An introduction to Pound–Drever–Hall laser frequency stabilization’, *Am. J. Phys.*, vol. 69, no. 1, pp. 79–87, Jan. 2001. https://doi.org/10.1119/1.1286663

[67] G. Cappellini, ‘Two-orbital quantum physics in Yb Fermi gases exploiting the 1S0 -> 3P0 clock transition’, PhD Thesis, University of Florence, Florence, 2016. https://flore.unifi.it/handle/2158/1045924

[68] C. Clivati, G. Cappellini, L. F. Livi, F. Poggiali, M. S. de Cumis, M. Mancini, G. Pagano, M. Frittelli, A. Mura, G. A. Costanzo, F. Levi, D. Calonico, L. Fallani, J. Catani, and M. Inguscio, ‘Measuring absolute frequencies beyond the GPS limit via long-haul optical frequency dissemination’, *Opt. Express*, vol. 24, no. 11, pp. 11865–11875, May 2016. https://doi.org/10.1364/OE.24.011865

[69] G. D. Domenico, S. Schilt, and P. Thomann, ‘Simple approach to the relation between laser frequency noise and laser line shape’, *Appl. Opt.*, vol. 49, no. 25, pp. 4801–4807, Sep. 2010. https://doi.org/10.1364/AO.49.004801

[70] A. L. Schawlow and C. H. Townes, ‘Infrared and Optical Masers’, *Phys. Rev.*, vol. 112, no. 6, pp. 1940–1949, Dec. 1958. https://doi.org/10.1103/PhysRev.112.1940

[71] ‘Encyclopedia of Laser Physics and Technology - Schawlow-Townes linewidth, single-frequency laser, phase noise’. . https://www.rp-photonics.com/schawlow_townes_linewidth.html

[72] T. Rützel, ‘Conceptual Design and Setup of a Highly Stable Laser for Precision Measurements on Ultracold Quantum Gases’, Diploma Thesis, Universität Hamburg, 2010

[73] J.-H. Carstens, ‘Stabilization of a Clock Laser for High Precision Spectroscopy on Ultracold Quantum Gases’, Diploma Thesis, Universität Hamburg, 2011.

[74] P. K. Madhavan Unni, M. K. Gunasekaran, and A. Kumar, ‘±30 μK temperature controller from 25 to 103 °C: Study and analysis’, *Rev. Sci. Instrum.*, vol. 74, no. 1, pp. 231–242, Jan. 2003. https://doi.org/10.1063/1.1529299

[75] Corning, ‘ULE® Corning Code 7972 Ultra Low Expansion Glass’, 13-Nov-2008. . https://www.corning.com/media/worldwide/csm/documents/D20FD2EA-7264-43DD-B544-E1CA042B486A.pdf

[76] K. Numata, A. Kemery, and J. Camp, ‘Thermal-Noise Limit in the Frequency Stabilization of Lasers with Rigid Cavities’, *Phys. Rev. Lett.*, vol. 93, no. 25, p. 250602, Dezember 2004. https://doi.org/10.1103/PhysRevLett.93.250602

[77] T. Kessler, T. Legero, and U. Sterr, ‘Thermal noise in optical cavities revisited’, *J. Opt. Soc. Am. B*, vol. 29, no. 1, pp. 178–184, Jan. 2012 . https://doi.org/10.1364/JOSAB.29.000178

[78] T. Legero, T. Kessler, and U. Sterr, ‘Tuning the thermal expansion properties of optical reference cavities with fused silica mirrors’, *J. Opt. Soc. Am. B*, vol. 27, no. 5, p. 914, May 2010. https://doi.org/10.1364/JOSAB.27.000914

[79] S. Häfner, ‘Ultra-stabile Lasersysteme für Weltraum- und Bodenanwendungen’, PhD Thesis, Universität Hannover, Hannover, 2015

[80] H. Stoehr, ‘Diodenlaser mit Hertz-Linienbreite für ein optisches Calcium-Frequenznormal’, Universität Hannover, Hannover, 2005

[81] R. W. Fox, ‘Temperature analysis of low-expansion Fabry-Perot cavities’, *Opt. Express*, vol. 17, no. 17, pp. 15023–15031, Aug. 2009. https://doi.org/10.1364/OE.17.015023

[82] M. Notcutt, ‘Mirror Deformation from mirror/spacer differential thermal expansion and its contribution to the cavity Zero Crossing Temperature’, Nov. 2010. http://www.stablelasers.com/spec-sheets/mirror_deformation.pdf

[83] J. W. Berthold and S. F. Jacobs, ‘Ultraprecise thermal expansion measurements of seven low expansion materials’, *Appl. Opt.*, vol. 15, no. 10, pp. 2344–2347, Oct. 1976. https://doi.org/10.1364/AO.15.002344

[84] I. Dotsenko, ‘Single atoms on demand for cavity QED experiments’, Ph. D. thesis, Rheinische Friedrich-Wilhelms Universität, Bonn, 2007. http://www.iaea.org/inis/collection/NCLCollectionStore/_Public/38/071/38071739.pdf

[85] JENOPTIK Optical Systems GmbH, ‘Integrated-optical modulators: Technical information and instructions for use’, 12-Jul-2015. https://www.jenoptik.com/-/media/websitedocuments/optical-systems/modulatoren/modulatorfibel_en.pdf

[86] S. Barke, M. Tröbs, B. Sheard, G. Heinzel, and K. Danzmann, ‘EOM sideband phase characteristics for the spaceborne gravitational wave detector LISA’, *Appl. Phys. B*, vol. 98, no. 1, pp. 33–39, Jan. 2010. https://doi.org/10.1007/s00340-009-3682-x

[87] W. Zhang, M. J. Martin, C. Benko, J. L. Hall, J. Ye, C. Hagemann, T. Legero, U. Sterr, F. Riehle, G. D. Cole, and M. Aspelmeyer, ‘Reduction of residual amplitude modulation to 1 × 1E-6 for frequency modulation and laser stabilization’, *Opt. Lett.*, vol. 39, no. 7, p. 1980, Apr. 2014. https://doi.org/10.1364/OL.39.001980

[88] I. Silander, P. Ehlers, J. Wang, and O. Axner, ‘Frequency modulation background signals from fiber-based electro optic modulators are caused by crosstalk’, *JOSA B*, vol. 29, no. 5, pp. 916–923, May 2012. https://doi.org/10.1364/JOSAB.29.000916

[89] N. C. Wong and J. L. Hall, ‘Servo control of amplitude modulation in frequency-modulation spectroscopy: demonstration of shot-noise-limited detection’, *J. Opt. Soc. Am. B*, vol. 2, no. 9, p. 1527, Sep. 1985. https://doi.org/10.1364/JOSAB.2.001527

[90] L. Li, F. Liu, C. Wang, and L. Chen, ‘Measurement and control of residual amplitude modulation in optical phase modulation’, *Rev. Sci. Instrum.*, vol. 83, no. 4, p. 043111, Apr. 2012. https://doi.org/10.1063/1.4704084

[91] A. Foltynowicz, I. Silander, and O. Axner, ‘Reduction of background signals in fiber-based NICE-OHMS’, *JOSA B*, vol. 28, no. 11, pp. 2797–2805, Nov. 2011. https://doi.org/10.1364/JOSAB.28.002797

[92] J. A. Barnes, A. R. Chi, L. S. Cutler, D. J. Healey, D. B. Leeson, T. E. McGunigal, J. A. Mullen, W. L. Smith, R. L. Sydnor, R. F. C. Vessot, and G. M. R. Winkler, ‘Characterization of Frequency Stability’, *IEEE Trans. Instrum. Meas.*, vol. IM–20, no. 2, pp. 105–120, May 1971. https://doi.org/10.1109/TIM.1971.5570702

[93] D. B. Sullivan, D. W. Allan, D. A. Howe, and F. L. Walls, *Characterization of clocks and oscillators*. National Institute of Standards and Technology Technical Note, 1990

[94] L.-S. Ma, P. Jungner, J. Ye, and J. L. Hall, ‘Delivering the same optical frequency at two places: accurate cancellation of phase noise introduced by an optical fiber or other time-varying path’, *Opt. Lett.*, vol. 19, no. 21, pp. 1777–1779, Nov. 1994. https://doi.org/10.1364/OL.19.001777

[95] J. C. Bergquist, W. M. Itano, and D. J. Wineland, *Laser stabilization to a single ion*. North Holland, Amsterdam, 1994

[96] M. Köhl, H. Moritz, T. Stöferle, K. Günter, and T. Esslinger, 'Fermionic Atoms in a Three Dimensional Optical Lattice: Observing Fermi Surfaces, Dynamics, and Interactions', *Phys. Rev. Lett.*, vol. 94, no. 8, p. 080403, Mar. 2005. https://doi.org/10.1103/PhysRevLett.94.080403

[97] N. D. Lemke, A. D. Ludlow, Z. W. Barber, T. M. Fortier, S. A. Diddams, Y. Jiang, S. R. Jefferts, T. P. Heavner, T. E. Parker, and C. W. Oates, 'Spin-1/2 Optical Lattice Clock', *Phys. Rev. Lett.*, vol. 103, no. 6, p. 063001, Aug. 2009. https://doi.org/10.1103/PhysRevLett.103.063001

[98] T. A. Savard, K. M. O'Hara, and J. E. Thomas, 'Laser-noise-induced heating in far-off resonance optical traps', *Phys. Rev. A*, vol. 56, no. 2, pp. R1095–R1098, Aug. 1997. https://doi.org/10.1103/PhysRevA.56.R1095

[99] M. M. Boyd, 'High precision spectroscopy of strontium in an optical lattice: Towards a new standard for frequency and time', PhD Thesis, University of Colorado at Boulder, 2007

[100] M. Kitagawa, K. Enomoto, K. Kasa, Y. Takahashi, R. Ciuryło, P. Naidon, and P. S. Julienne, 'Two-color photoassociation spectroscopy of ytterbium atoms and the precise determinations of s-wave scattering lengths', *Phys. Rev. A*, vol. 77, no. 1, p. 012719, Jan. 2008. https://doi.org/10.1103/PhysRevA.77.012719

[101] Y. Takasu and Y. Takahashi, 'Quantum Degenerate Gases of Ytterbium Atoms', *J. Phys. Soc. Jpn.*, vol. 78, no. 1, p. 012001, Jan. 2009. https://doi.org/10.1143/JPSJ.78.012001

[102] Y. Takahashi, 'Quantum Simulation Using Ultracold Ytterbium Atoms in an Optical Lattice', in *Principles and Methods of Quantum Information Technologies*, Springer, Tokyo, 2016, pp. 309–324. https://doi.org/10.1007/978-4-431-55756-2_14

[P1] K. Sponselee, L. Freystatzky, B. Abeln, M. Diem, B. Hundt, A. Kochanke, T. Ponath, B. Santra, L. Mathey, K. Sengstock, C. Becker, 'Dynamics of Ultracold Quantum Gases in the Dissipative Fermi-Hubbard Model' *New Journal of Physics*, In Review (2018) https://arxiv.org/abs/1805.11853

Danksagung

Die vorliegende Arbeit hätte ohne die Motivation und Unterstützung zahlreicher Personen, die mich und meine Forschung in den vergangenen Jahren begleitet haben, nicht entstehen können. Einigen Personen möchte ich namentlich danken:

Zuallererst danke ich meinem Doktorvater Prof. Dr. Klaus Sengstock für die Möglichkeit in der Forschungsgruppe Quantengase an so einem spannenden Experiment forschen und promovieren zu dürfen. Deinen Einsatz für das Institut und für die Gewährleistung der Versorgung des Experiments kann man nicht hoch genug schätzen. Dein entgegengebrachtes Vertrauen in meine Arbeit und die motivierenden Worte während der Schreibphase haben mir sehr geholfen.

Dr. Christoph Becker danke vielmals ich für seine unumstößliche Unterstützung des Ytterbium Experiments. Das Projekt lebt von Deinem umfassenden Wissen zur Physik und Technik sowie von Deinem Antrieb, welcher mich auch persönlich hat wachsen lassen. Ich danke Dir zudem für Deine vielen hilfreichen Anmerkungen während der Entstehung des Manuskripts.

Meinen Doktoranden - Vorgängern am Ytterbium Experiment, Dr. Alex Thobe und Dr. Sören Dörscher, gilt mein herzlicher Dank für die höchst kompetente wissenschaftliche Einführung ins Experiment und für ihre stetige Bereitschaft, meine Fragen mit viel Geduld zu beantworten. Eure Arbeiten beeindrucken mich immer wieder aufs Neue.

Ganz besonders danke ich meinen beiden Kollegen und „Laborbuddys“ Dr. André Kochanke und Dr. Bastian Hundt für ihre fantastische Kollegialität, die fruchtbare Zusammenarbeit und die enge Freundschaft, die sich während und außerhalb der vielen gemeinsamen Stunden im Labor entwickelt hat - und nicht zuletzt für die Aufmunterungen und vielen Korrekturhinweise in der Schlussphase meiner Arbeit. Ich freue mich schon auf viele weitere Stunden mit Euch!

Dr. Bodhaditya Santra, Koen Sponselee und allen MasterandInnen und BachelorandInnen des Ytterbium Projekts danke ich für die freundschaftliche Stimmung im Team und für die exzellente Arbeit: Benjamin Abeln, Lars Hilbig, Niels Petersen, Anna Skottke und Torben Sobottke.

Ich bedanke mich bei Prof. Dr. Henning Moritz für die Übernahme des Zweitgutachtens meiner Dissertation.

Ich danke allen Initiatoren, Fellows und Mitarbeitern des Marie Curie Initial Training Networks "QTea" für ihren Einsatz, allen voran Prof. Dr. Thomas Fernholz. Die wertvollen Erfahrungen

und die Einblicke in vielfältige Forschung jenseits des eigenen Labors auf Treffen und Summer Schools sowie die gegenseitige Unterstützung im Netzwerk haben mir sehr geholfen.

Allen KollegInnen, ProfessorInnen und MitarbeiterInnen am ILP und ZOQ danke ich für die gute Atmosphäre und die stete Hilfsbereitschaft, die das Leben und Arbeiten an den Instituten so angenehm gemacht hat. Im Besonderen danke ich Janina Neubert für die Übernahme vieler organisatorischer Belange, für ihre Herzlichkeit und Optimismus, sowie für ihre Freundschaft.

Ein ganz besonderer Dank gilt meiner Familie, Ludmila, Hans-Ernst und Daniel, für ihr Vertrauen, ihre Fürsorge und die unermüdliche Unterstützung. Zuletzt danke ich Malte, Mauricio, Evy und Anna. Eure Freundschaft, eure offenen Ohren, eure Zuversicht und eure Anregungen haben mich in allen Phasen meines Lebens bereichert. Danke!

Hamburg im Mai 2018

Thomas Georg Ponath

Errata

Section 4.2.1, Figure 32: High-resolution clock spectroscopy

Taking the generalised Rabi cycle into consideration, we can adapt the fit function for the high-resolution single spin-component spectra recorded with Rabi $1{\cdot}\pi$ pulses to the form of an ideal line shape of a Rabi resonance, shown in equation (e1). This function fits the measurements better than a $\mathrm{sinc}^2(a \cdot \Delta/w)$ function shown in Figure 32, especially regarding the off-resonant side-peaks. The extracted properties presented in the thesis, such as central peak linewidths and excitation ratios, are not affected by the adapted fit function.

$$P\left(\Delta, \omega_1, t = \frac{\pi}{\omega_1}\right) = \mathrm{A} \cdot \frac{\omega_1^2}{\Delta^2 + \omega_1^2} \cdot \sin^2\left(\frac{1}{2} \cdot \frac{\pi}{\omega_1} \cdot \sqrt{\omega_1^2 + \Delta^2}\right) + P_{offset} \qquad \text{(e1)}$$

A allows for a vertical scaling, $\Delta = \omega - \omega_0$ is the frequency detuning, P_{offset} allows for a vertical offset.

The measured spectra fitted with Rabi line shape curves as in equation (e1) are shown in Figure E1.

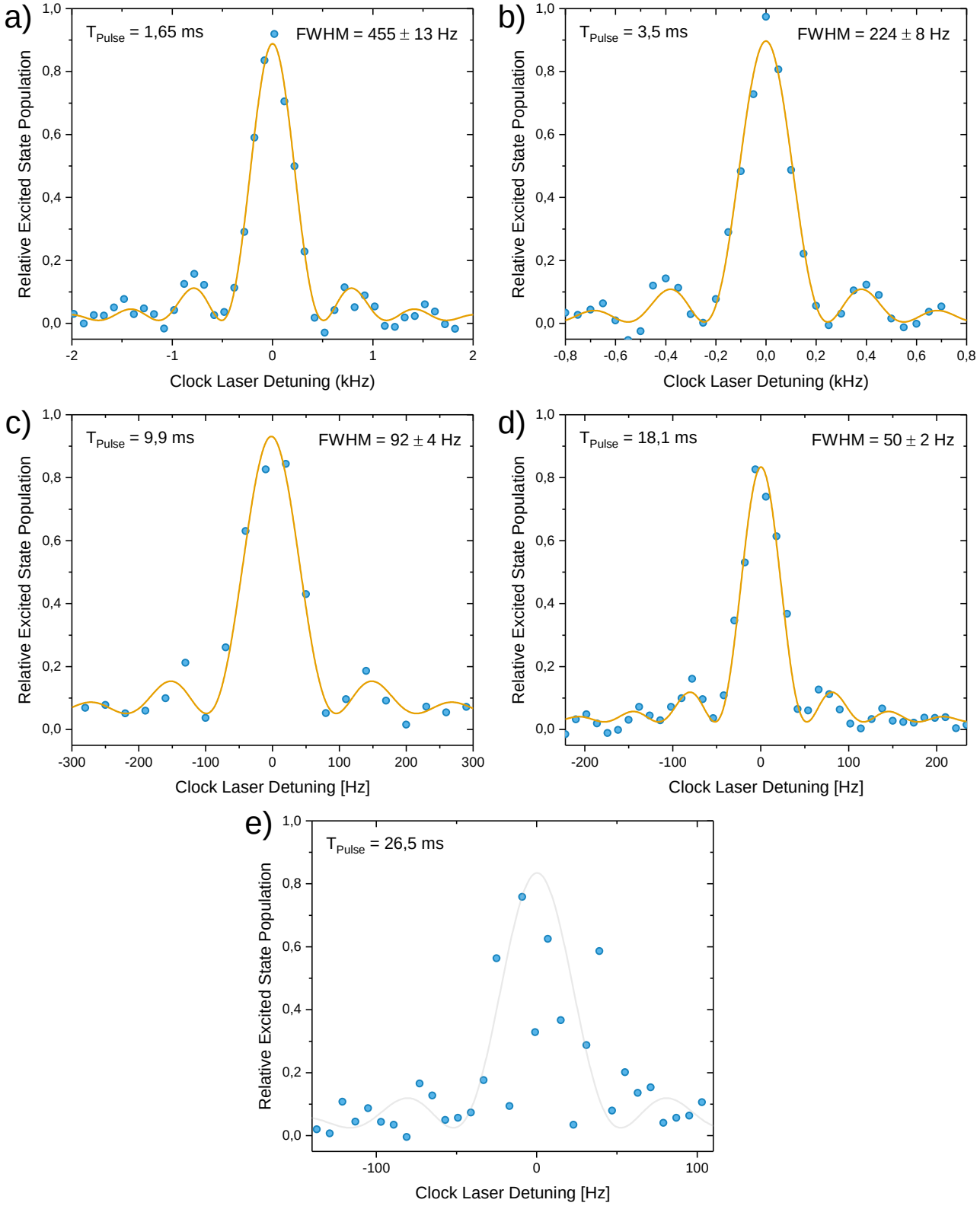

Figure E1: High-resolution clock spectroscopy measurements on ultra-cold gases of spin-polarised ^{173}Yb in an optical lattice. The plots show the relative excited state population, normalized to the total atom count, together with fitted Rabi line shape curves (equation (e1)). All spectra show single experimental runs, with clock laser pulses at Rabi 1·π pulse duration. We observe excitation ratios of 82-97%. Fit curves (solid orange lines) expected from theory fit well to spectra a)-d). However, spectra a) and b) undercut the Fourier-limited FWHM by over 12%. We successfully recorded spectra down to a Fourier-limited resolution of 50 Hz FWHM. Attempting to access a higher resolution in spectrum e) (with overlay of sinc² fit of spectrum d) in gray), shows multiple excitations scattered over a similar width as for the 50 Hz spectrum. This indicates that low-frequency noise limits a higher spectroscopy resolution.

Section 4.3.2: Spectroscopy of a two-component Fermi gas

Reevaluating the spectroscopy features' positions for our lattice configuration with recoil energy of $E_R = h \cdot 1{,}99$ kHz and using values from [26] predicts the excitation of the $|-\rangle$ state at a detuning of -400 ± 40 Hz, shown in Figure E2. Therefore, the measured detuning of the $|-\rangle$ state at -240 ± 20 Hz presented in Figure 36 qualitatively agrees with the theory calculations. More detailed numerical calculations also considering interaction energy values published in [27,34] may resolve the remaining frequency discrepancy.

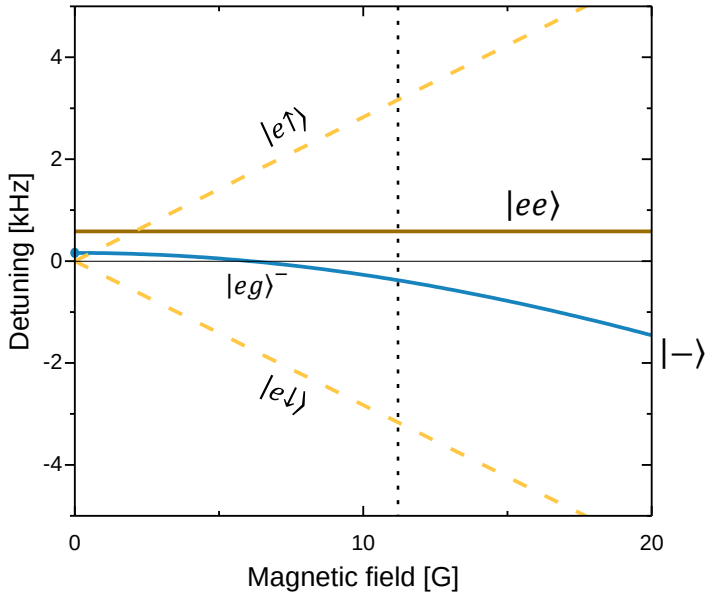

Figure E2: Theoretically expected positions of excitations in a two-component Fermi gas spectroscopy measurement presented in section 4.3.2 and based on values from [26], with singly and doubly occupied lattice sites. Excitations of singly occupied sites, $|e\uparrow\rangle$ and $|e\downarrow\rangle$, shown with yellow, dotted lines. The interaction state $|eg\rangle^-$ transforming into the $|-\rangle$ state for larger magnetic fields is shown in blue. At the magnetic field strength of 11,6 G as used in the experiment (dotted vertical line) the interaction state $|eg\rangle^-$ is expected at a detuning of ≈-400 ± 40 Hz. The frequency detuning of the doubly excited state $|ee\rangle$, shown in brown, is independent of the magnetic field strength. The interaction state $|eg\rangle^+$, respectively $|+\rangle$, is far in the positive detuning, outside of this scale.